Technische Universität Braunschweig

DLR

IGEP TU Braunschweig

Institut für Geophysik und extraterrestrische Physik

Thermal Conductivity Measurements of Dry and Icy Lunar Regolith Simulants

Master Thesis for the Attainment of the Academic Degree of
Master of Science in Physics

Submitted to the
Institute of Geophysics and Extraterrestrial Physics

in Cooperation with the
German Aerospace Center Bremen

Henning Wache
4969879

Supervisors:
Prof. Dr. Jürgen Blum
Dr.-Ing. Paul Zabel

Supported by:
Luca Kiewiet and Christopher Kreuzig

July 31, 2024

Declaration of Originality

I hereby confirm that the submitted thesis was written by myself without any further assistance from others. No sources other than those listed as references have been used and appropriate credit has been allocated accordingly. All figures and tables have either been created by myself or have been provided with references to the respective authors. This thesis has not been examined in any form before, nor has it been published yet.

Henning Wache

Braunschweig, July 31, 2024

Declaration of Conformity

I hereby confirm that the electronic and printed versions of this thesis are identical. Both versions contain the same content, including text, figures, and tables, and no alterations have been made between the two formats.

Henning Wache

Braunschweig, July 31, 2024

Contents

1. Introduction

Now, more than ever, humans have longed to explore outer space. Recent advancements in both technology and science have brought us closer to establishing a permanent human presence beyond our home planet. The Moon represents a pivotal point in humanity's exploration of the solar system. However, a permanent human presence outside the reach of Earth requires not only vast amounts of fuel but also consumables for the crew, which cannot be sourced from our home planet indefinitely. With the recent confirmations of the presence of water ice on the lunar surface, such long-term objectives begin to appear within reach. If extracted, this water could not only be used to support human life, but also to be transformed into hydrogen and oxygen, which yields a potent rocket propellant that might help transport humans to Mars and beyond.
One question that is still unanswered to date is the exact location and morphology of this ice on the initially thought dry lunar surface. Since the Moon has no significant atmosphere, water can only exist in extremely cold regions. Fortunately, the lunar south pole contains some of the coldest places found in the entire solar system, the so-called Permanently Shadowed Regions (PSRs), which are craters where the sun never shines. Beyond the boundaries of these craters, the rough and weathered surface, composed of a highly irregular and porous material called regolith, could provide thermal insulation from what lies below, possibly allowing the presence of solid water ice.

In order to physically model local temperature conditions in ice-bearing regions on the lunar surface, thermal conductivity measurements are required as input parameters. Since in-situ or remote-sensing missions are very costly, this study aims to provide laboratory measurements of the thermal conductivity of icy regolith simulant materials, which can be used as an approximation for the thermal conductivity of real lunar icy materials. As the nature of ice in such a material alters the thermal properties, this study focuses on a specially created discrete microgranular icy regolith simulant and compares it to a fused icy mudpie simulant to provide insight into two possible ice morphologies that might occur on the Moon. The novel microgranular simulant aims to simulate the impact that millennia of space weathering may have had on the ice present on the lunar surface, while the mudpie simulant resembles fused subsurface ice layers.
The objective of this study is to analyze the temperature behavior of the thermal conductivity of such icy samples in comparison to dry regolith simulant samples. The effects of ice content but also temperature-dependent effects such as sintering and possible re-cementation processes via sublimation and deposition are of interest, given that diurnal temperature changes on the Moon most likely influence any ice in the upper surface layers and near PSRs. It is currently unknown how the morphology of the ice and the thermal conductivity of the material are influenced by this effect, although an increase in thermal conductivity with increasing cementation is anticipated.

An application of such thermal conductivity measurements is the extraction of water from icy regolith. For future in-situ missions and laboratory-based experiments, it is necessary to evaluate the thermal conductivity of ice-bearing materials. This knowledge will contribute to the optimization of heating methods and the development of thermal models.

The following chapter 2 provides a short introduction to the conditions on the lunar surface and the occurrence of water on the Moon in addition to a short introduction to the theory of heat transport in granular media such as regolith. The creation of the novel icy lunar regolith simulant is presented in Chapter 3, while the details on the measurement setup created for this work are given in Chapter 4. Chapter 5 then presents the transient hot strip method utilized to measure the thermal conductivity, while the results are presented and discussed in Chapter 6 for several dry and icy lunar regolith samples in a temperature range of 120 K to 450 K. Chapter 7 provides a more generalized discussion of these findings and puts them into context with the objective of this study. Finally, the results of this study are summarized in Chapter 8, and an outlook for future measurements and potential improvements to the setup is given.

2. Lunar Conditions and Heat Transport Theory

2.1. Lunar Conditions

The Moon is the largest natural satellite of the Solar System in relation to its primary planet. It has a mass of $7.35 \cdot 10^{22}$ kg and a mean radius of 1738 km, with a surface gravity of only $1.62\,\mathrm{m\,s^{-2}}$, which is one sixth of that of Earth [1]. Due to its low mass and weak magnetic field, the Moon only has a loosely bound atmosphere with pressures on the order of 10^{-12} mbar, which is comparable to the best technical vacuum currently achievable in laboratories on Earth. Additionally, the mean surface temperature varies drastically from approximately 100 K to 400 K during a regular lunar day.

In the absence of a significant atmosphere, the Moon's surface exhibits a considerable age, with structures that were created shortly after the formation of the Moon, approximately 4.5 billion years ago. In general, the lunar surface can be divided into two distinct types of regions, which are the dark maria and the lighter highlands. The maria are basalt-rich regions that formed due to the differentiation process and volcanic activity. The highlands, on the other hand, contain mostly anorthosite and are older than the maria, as no volcanism occurred here. Due to their older age, the highlands show an abundance of craters, which are a result of the bombardment with asteroids and comets in the early days of the solar system's formation process. These craters are especially prominent on the far side of the Moon, as shown in Figure 2.1.

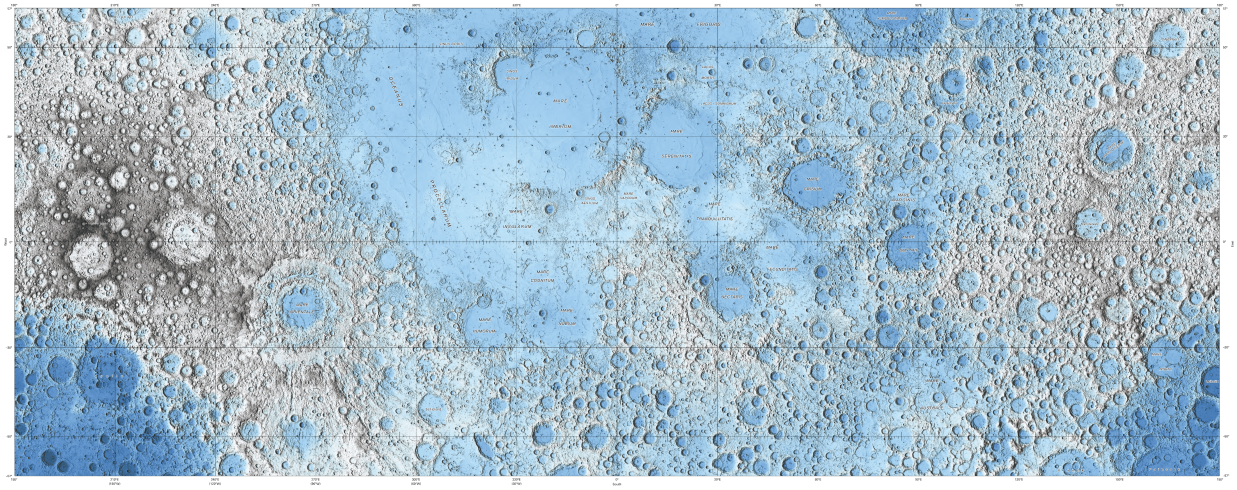

Figure 2.1.: Topography of the lunar surface. The darker maria are situated at low elevations, while the highlands, which are marked by a multitude of craters, are located at higher elevations mostly on the far side of the Moon (left and right). The color map indicates the elevation of the surface ranging from approximately −9 km (dark blue) to 11 km (dark gray) [2].

2.1.1. Regolith Surface

While larger impacts from comets and asteroids excavated large amounts of material, small impacts from micro-meteorites and the constant exposure to solar and cosmic ionizing radiation led to the creation of regolith, a fine dust of highly irregular particles that covers the entire surface. This erosion process is often referred to as space weathering.
The thickness of the regolith varies depending on the location. For the younger maria, the thickness is typically a few meters, while in older highland regions, it can reach up to 20 m [1]. Below this fine dusty material, there is a layer with larger ejecta fragments, probably meters in size.
From the Apollo and Luna missions, a considerable number of rock and regolith samples were returned to Earth for analysis. Through these samples, the size distribution as well as the chemical and mineral compositions are well known today. However, depending on the location from which the samples were obtained, variations were found mostly concentrated between the basalt-rich maria and the anorthosite-rich highlands. Intermediate differentiations were also identified, indicating a versatile surface composition [1]. The regolith particles are on average micrometers in size and highly irregularly shaped, resulting in a highly porous packing structure with average bulk densities of the order of $1.5\,\mathrm{g\,cm^{-3}}$ [1]. Due to the relatively weak gravitational attraction to the Moon and the electrostatic forces between the particles, they disperse over broad ranges if moved, but may also adhere to anything they come in contact with, creating a significant challenge for any in situ experiments, especially if moving parts are involved.

2.1.2. Water

The presence of water on the Moon was not always certain. Given the extremely thin atmosphere, it was initially thought that water could not exist on the lunar surface. However, due to the axial tilt of the Moon, there are craters in the polar regions that are permanently shaded from the sun, resulting in maximal annual surface temperatures below 110 K, allowing for water ice to exist [3]. The presence of ice in these PSRs was proven not only by remote sensing data, but also by an impact experiment done with the Lunar Crater Observation and Sensing Satellite (LCROSS). Remote sensing data, for example, from the Moon Mineralogy Mapper (M3), was analyzed by Li et al. [3], who found up to 30 wt % of water ice in some PSRs near the south pole, while Colaprete et al. [4] found approximately 5 wt % of water in the ejecta plume of the LCROSS impact experiment at the Cabeus crater at 85 °S, in addition to multiple other volatiles. Figure 2.2 shows a map of the northern and southern lunar hemispheres, indicating the locations that were identified by Li et al. [3] as potential locations containing water ice. Notably, only 3.5 % of all PSRs exhibited ice signatures, indicating that temperature alone is not a sufficient indicator of potential water-bearing sites.
In addition to these findings, evidence for water was discovered outside of PSRs as well. By analyzing in situ reflectance spectra of the Lunar Mineralogical Spectrometer (LMS) on board the Chang'e-5 lander, Lin et al. [5] found 120 ppm of water in the lunar regolith at a relatively low latitude of 43 °N. A differentiation between H_2O and HO was not possible, which means that hydroxyl groups could also account for this finding. Similarly Honniball et al. [6] found evidence for molecular water on the sunlit lunar surface from reflectance measurements by the Stratospheric Observatory for Infrared Astronomy (SOFIA).

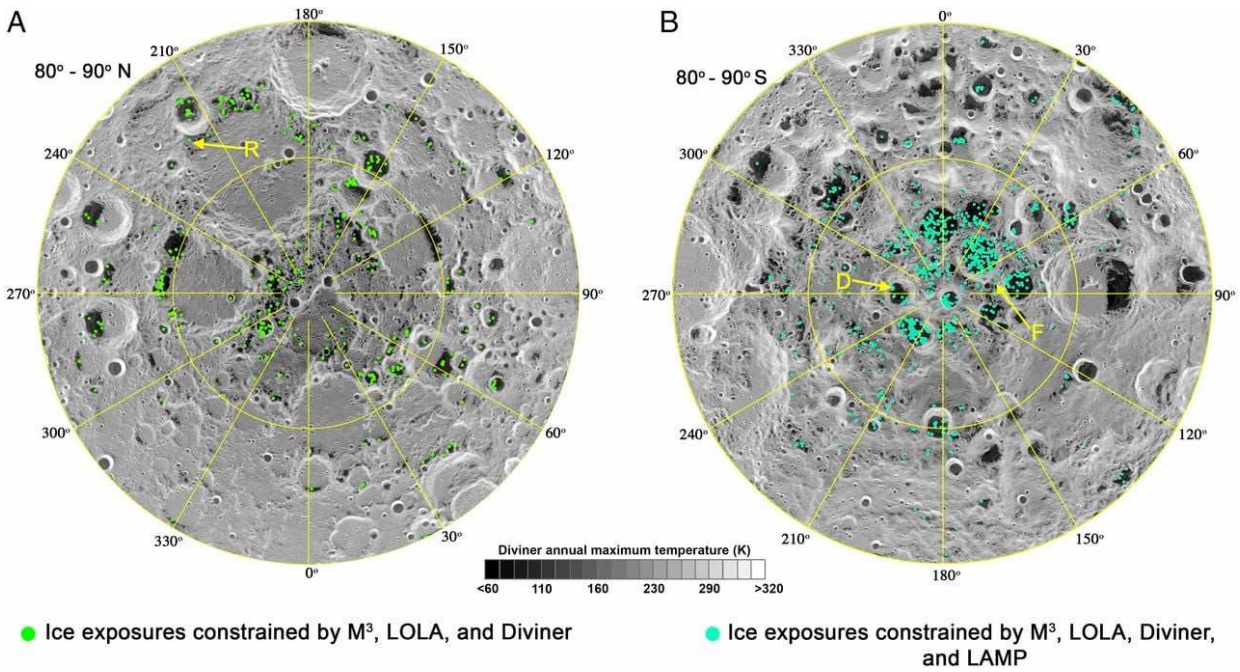

Figure 2.2.: Water-ice bearing sites of the northern (left) and southern (right) lunar polar regions with the maximum annual temperature as derived from Diviner remote sensing data [3]. The southern polar region shows indications of PSRs with more concentrated water ice.

In addition to large-scale PSRs, Hayne, Aharonson, and Schörghofer [7] found that water ice could also accumulate in micro-cold traps scattered in the polar regions. These micro-cold traps, which are mostly centimeters in size, are the most abundant form of cold traps on the lunar surface, given that only small alterations in the terrain provide sufficient low temperatures for water ice to exist.

While hydrogen is implanted by the solar wind into minerals in the soil, molecular water could be trapped in volcanic glasses or within the pore space of the regolith. In cold traps or subsurface layers, ice could be present in a fused or discrete form. However, the general origin and morphology of water on the lunar surface is unknown.
Larger amounts of water could have been brought to the Moon by asteroids and comets. Given the high-energy nature of these impacts and the fact that the heat of the sun would prevent the majority of water from maintaining a solid form, some amounts of water ice sublimes and may deposit again at colder regions like the PSRs or micro cold traps, while other ice particles might be scattered and intermixed with the upper few layers of regolith.
It is also possible that water is more abundant in the subsurface due to outgassing from the early differentiation processes and as a consequence of volcanic activity as shown by Chakraborty et al. [8].
Additionally, water that migrated through the regolith in gaseous form and deposited in colder regions, as well as ice that was buried during impacts, is protected by the insulating capabilities of the regolith. In regions where the maximum diurnal temperature is not too large, this would create a layer of ice below a desiccated surface layer of regolith.

In conclusion, the multitude of processes that could have brought water to the Moon and subsequently altered it, including impact gardening and changes in diurnal and long-term temperature, could also result in the formation of a diverse array of morphologies and abundances of water ice on the lunar surface. Future in situ observations by, for example, JAXA's Lunar Polar Exploration Mission (LUPEX), future Chinese Chang'e missions, or similar missions to NASA's recently canceled Volatiles Investigating Polar Exploration Rover (VIPER), will provide further insight into the precise characteristics of the ice present at the lunar polar regions.

2.2. Heat Transport in Granular Media

Heat transport in granular media such as regolith differs from that of solid materials. While a singular grain may transport heat through solid conductivity, the finite amount and size of contact points between the grains restrict the efficiency of heat transfer to adjacent grains. In addition, the pore space between the grains can be utilized for heat transport as well. It is not only photons in the form of thermal radiation that can transfer heat from a warm to a cold location, but also gas via diffusion. These three main components of heat transfer are illustrated by Figure 2.3.

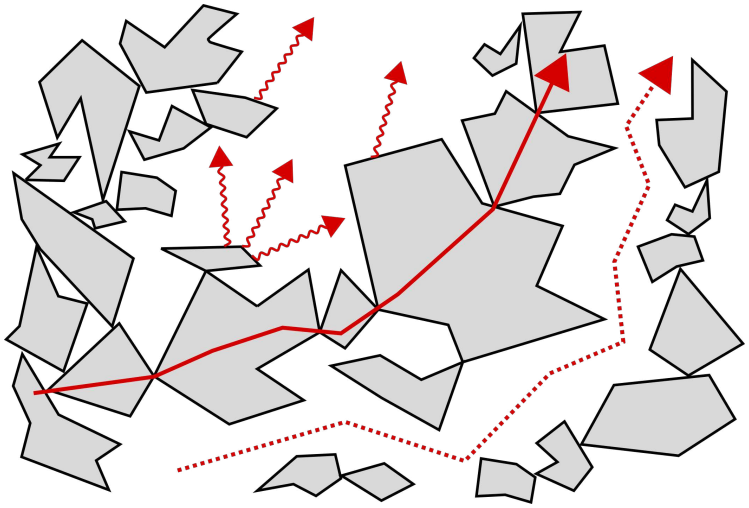

Figure 2.3.: Illustration of heat transfer in granular media. From a warmer area, heat may be transported via conduction (solid line) from grain to grain and via radiation (wavy lines) or via gas diffusion (dotted line) in the pore space between the grains.

The contact conductivity can be orders of magnitudes smaller than the solid conductivity of the individual grains, especially for materials that are highly angular and not elastic, where contact points consist of only a few layers of atoms. The radiative conductivity is strongly dependent on the mean free path of the photons, which corresponds to the size of the pore space. If there are many differently sized particles in the granular medium, smaller particles might fill the space between the larger ones, thereby limiting the radiative conductivity. Similarly, gas diffusion also depends on the pore space if the gas molecules can travel freely. However, this is restricted by the number of gas molecules in the pore space as explained in Section 2.2.2.
In the field of planetary sciences, granular media occur mostly exposed to vacuum, for example on asteroids or the lunar surface. Therefore, the gas conductivity is negligible and only the contact

and radiative conductivity play a significant role in the heat transfer. The following section presents an empirical model for such an application.

2.2.1. The Gundlach Blum Model of Thermal Conductivity

One model of the combined thermal conductivity of contact and radiative heat transport in a granular medium was introduced by Gundlach and Blum [9, 10]. The model was developed using equal-sized spheres of radius r that are packed in a granular manner with a volume filling fraction $\phi = \rho_{\mathrm{bulk}}/\rho_{\mathrm{material}}$, bulk density ρ_{bulk} and solid material density ρ_{material} at a temperature T.
In the model, the solid thermal conductivity λ_{solid} of the individual particles is reduced by a Hertzian factor to account for the heat transfer only occurring at the contact points of the particles in the granular medium. This factor depends on Poisson's ratio $\mu = 0.25$, Young's modulus $E = 7.8 \cdot 10^{10}\,\mathrm{Pa}$, the surface energy $\gamma = 0.02\,\mathrm{J\,m^{-2}}$ and the particle radius r, with the constants taken from Bürger et al. [11] for the application of the model to lunar regolith. The radiative thermal conductivity is a strongly temperature-dependent function that depends on the mean free path of the photons, which in turn depends on the volume filling fraction and the grain radius with the Stefan-Boltzmann constant σ_{SB} and the emissivity in the infrared range of the material ϵ. If combined, this results in the effective thermal conductivity given by Equation 2.1:

$$\lambda(r, \phi, T) = \lambda_{\mathrm{solid}}(T)\left(\frac{9\pi}{4}\frac{1-\mu^2}{E}\frac{\gamma}{r}\right)^{1/3} f_1 \exp(f_2\phi)\cdot\chi + 8\sigma_{\mathrm{SB}}\epsilon T^3 e_1 \frac{1-\phi}{\phi} r\,. \tag{2.1}$$

Here, $f_1 = 5.18 \cdot 10^{-2}$ and $f_2 = 5.26$ are empirical constants while $e_1 = 1.34$ and χ are scaling parameters. The latter one was introduced to apply the model to non-monodisperse and irregular-shaped particles like regolith.

To account for the very low-temperature regimes that can be found on planetary bodies, the solid conductivity has to be temperature dependent, since the phonon movement that is responsible for heat transport will freeze out at these low temperatures, resulting in the thermal conductivity also approaching zero [12]. Bürger et al. [11] accounted for this by fitting the thermal conductivity measurements done on lunar meteorites with a fifth-order polynomial as given by Equation 2.2 with $a = 0$:

$$\lambda_{\mathrm{solid}}(T) = a + bT + cT^2 + dT^3 + eT^4 + fT^5\,. \tag{2.2}$$

The thermal conductivity model was then calibrated to fit experimental measurements of the thermal conductivity of Apollo lunar regolith samples, yielding $\chi = 0.69$ for maria regions and $\chi = 0.14$ for a low conductivity highlands model. Additionally, $\chi = 0.69$ was utilized for a high thermal conductivity highlands model was well.
Figure 2.4 shows the temperature dependence and the influence of variations in r, ϕ, and χ for the Gundlach Blum Bürger (GBB) model, which will be referred to as such from now on. For larger particles, small volume filling fractions and large temperatures, the radiative conductivity dominates, resulting in the strong T^3 dependence. For small particles and small volume filling fractions, the conductive conductivity dominates because of a reduced size of the void space and an increase in contact area. Finally, χ scales the solid conductivity.

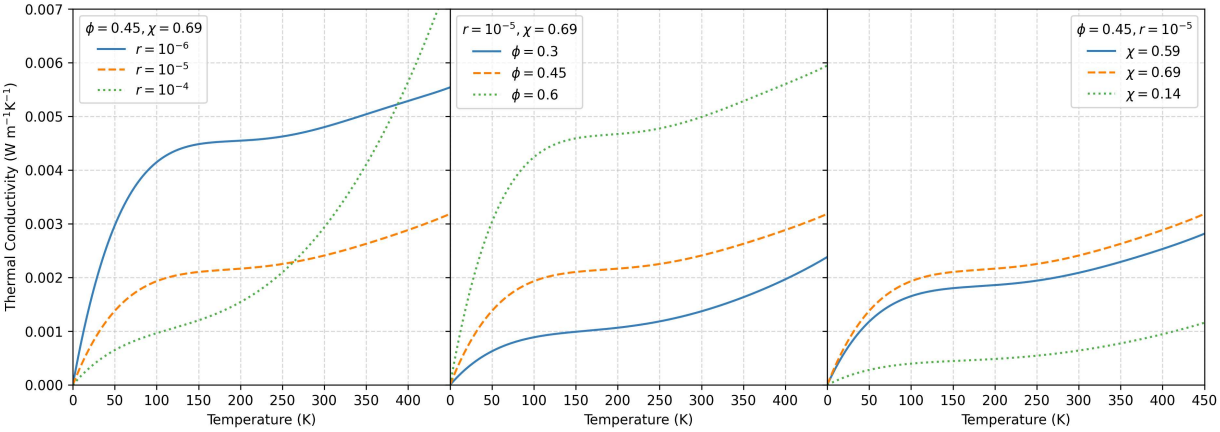

Figure 2.4.: Plots of the GBB model for varying parameters r, ϕ and χ.

2.2.2. Thermal Conductivity of a Gas Component

Although gasses are not present in a vacuum, volatiles in a granular medium may sublimate during temperature or pressure changes, which leads to gas that may diffuse through the pore space, contributing to the transport of heat. The thermal conductivity of a gas depends on the pressure, but only if it is low enough, which is the case if the mean free path l_{mfp} of the gas is greater than a characteristic length d of the volume in which it resides. This is quantified by the Knudsen number

$$\mathrm{Kn} = \frac{l_{\mathrm{mfp}}}{d} \,. \tag{2.3}$$

For large Knudsen numbers $\mathrm{Kn} > 1$, singular gas particles may travel freely through the given volume while for $\mathrm{Kn} < 1$, collisions happen frequently and kinetic gas theory has to be applied. With the kinetic gas theory, the mean free path of a gas depends on pressure and temperature, as well as the molecular cross-section of the scattering particles $\sigma = \pi D^2$ as given by Equation 2.4:

$$l_{\mathrm{mfp}} = \frac{k_{\mathrm{B}} T}{P \sigma \sqrt{2}} \,. \tag{2.4}$$

Here, $D = 2.65 \cdot 10^{-10}\,\mathrm{m}$ is the kinetic diameter, in this case of water [13]. The pressure in the pore space is limited by the sublimation. As volatiles sublime, the pressure rises until the sublimation pressure is reached. Therefore, the sublimation pressure is the maximal pressure in the pore space. To calculate the sublimation pressure of water in mbar, Equation 2.5 may be used with the constants listed in Table 2.1 [14]:

$$P(T) = 10^{A + B/T + C\log(T) + DT} \frac{1}{100} \,. \tag{2.5}$$

This equation is valid for temperatures in the range of 100 K to 273.16 K and shown in Figure 2.5.

With the assumption of an ideal gas, the kinetic gas theory leads to a contribution to the effective thermal conductivity through Equation 2.6 [15]:

$$\lambda_{\mathrm{gas}} = \frac{f}{6} \frac{k_{\mathrm{B}} \bar{v}}{\sigma \sqrt{2}} \,. \tag{2.6}$$

Table 2.1.: Constants for the calculation of the sublimation pressure of water [14].

A	B	C	D
4.07023	-2484.986	3.56654	-0.00320981

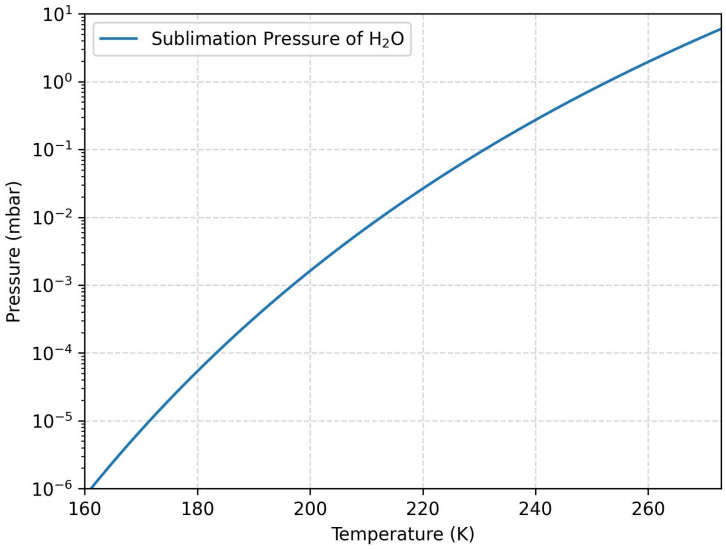

Figure 2.5.: Sublimation pressure of water as given by Equation 2.5.

With water being a triatomic molecule, $f = 6$ represents the thermally activated translational and rotational degrees of freedom. This relation is independent of pressure, but depends on temperature via the mean particle speed

$$\bar{v} = \left(\frac{8k_\mathrm{B}T}{\pi m}\right)^{1/2}, \tag{2.7}$$

where $m = 2.99 \cdot 10^{-26}\,\mathrm{kg}$ is the mass of a water molecule.
Under the assumption that the sublimation pressure is present at all times in the pore space at a given temperature, the mean free path as given by Equation 2.4 follows a trend as shown in Figure 2.6. For regolith, with an assumed pore space size d in the same order as the mean particle sizes in the tens of micrometers, the Knudsen number only exceeds one for elevated temperatures above 250 K, where kinetic gas theory becomes important.
For larger Knudsen numbers at lower temperatures, where the sublimation pressure is smaller than 1 mbar, the thermal conductivity of the gas in the pore space directly depends on the number of molecules transporting heat from one part in the pore space to another, since no collisions occur. This means that the thermal conductivity of the gas is proportional to the pressure P and the size of the volume d as given by Equation 2.8 [16]:

$$\lambda_\mathrm{gas} = \frac{3}{8} P d \sqrt{\frac{3R}{MT}}\,. \tag{2.8}$$

Here, M is the molar mass of the gas and R is the universal gas constant. Under the assumption that the sublimation pressure is present at all times, this molecular flow leads to a thermal conductivity as shown in Figure 2.7 for different pore space sizes.

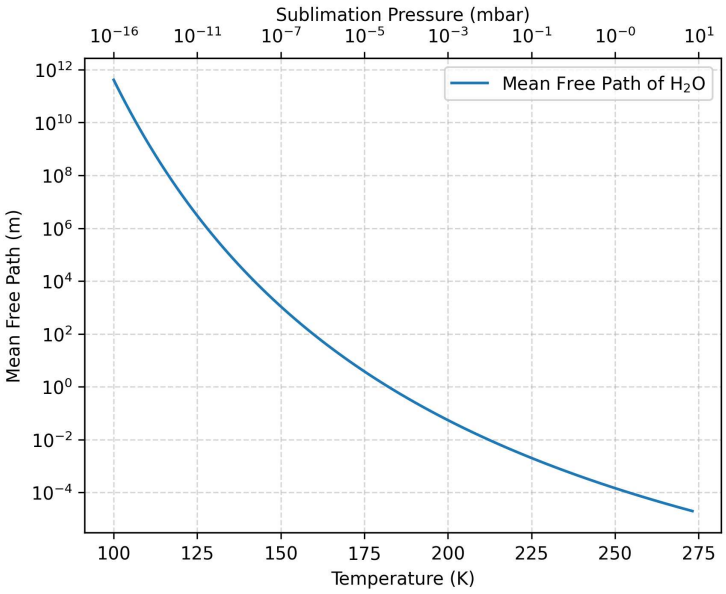

Figure 2.6.: Mean free path of water gas as calculated with the kinetic gas theory and Equation 2.4. It is assumed that the gas is constantly at the sublimation pressure, which only depends on the temperature.

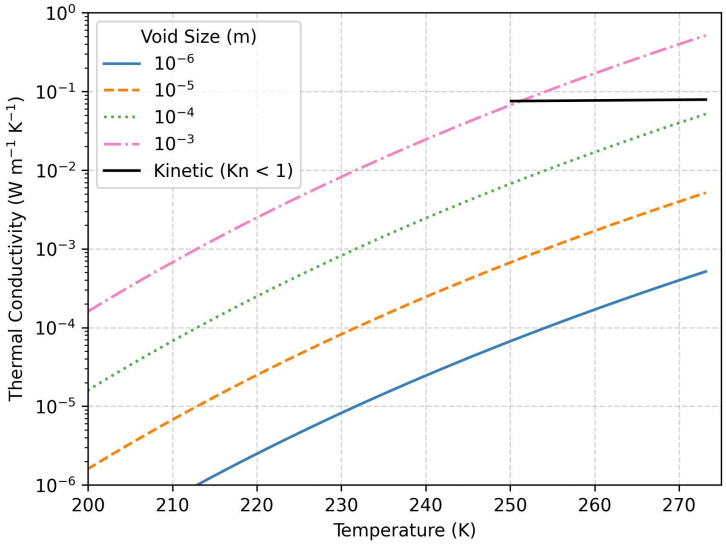

Figure 2.7.: Thermal conductivity of water gas at the sublimation pressure for the assumption of molecular flow in differently sized voids. Additionally, the thermal conductivity in the case of the kinetic gas theory above 250 K with Knudsen numbers greater than one is shown.

For regolith, the gas diffusion thermal conductivity is thereby negligible for lower temperatures and small pore spaces.
However, for small Knudsen numbers as well as at the transitional region, diffusive thermal conductivity might have a significant impact. In the temperature range of 240 K to 250 K, diffusion contributes with $10^{-3}\,\mathrm{W\,m^{-1}\,K^{-1}}$ to $10^{-2}\,\mathrm{W\,m^{-1}\,K^{-1}}$ to the effective thermal conductivity for an assumed pore space size of $10^{-4}\,\mathrm{m}$.
In addition to diffusive heat transport, gas is also able to transport energy via latent heat. In the sublimation process, a certain amount of heat that would otherwise be transported away via radiation, conduction, or regular diffusion is converted into latent heat. The molecules that are now in gaseous form may deposit at another point in the pore space, thereby converting the latent heat back into heat. Alternatively, the molecule may leave the system entirely. Both cases would result in an increase in the effective thermal conductivity.
Steiner and Kömle [17] derived Equation 2.9 for the thermal conductivity due to latent heat in the void spaces of a porous ice sample, assuming a geometry of two planes at different temperatures:

$$\lambda_{\text{latent heat}} = \left(\frac{m}{2\pi k_\mathrm{B} T}\right)^{1/2} \frac{\mathrm{d}P}{\mathrm{d}T} LS\,. \tag{2.9}$$

In the regime of free molecular flow, this formula was derived using the Hertz-Knudsen evaporation rate, which depends on the sublimation pressure P. Thereby, a water molecule of mass m would transport the latent heat $L = 2834\,\mathrm{J\,g^{-1}}$ over the distance S through the pore space. The temperature derivative of the sublimation pressure is calculated from Equation 2.5, resulting in Equation 2.10:

$$\frac{\mathrm{d}P}{\mathrm{d}T} = P(T) \cdot \log(10) \cdot \left(-\frac{B}{T^2} + \frac{C}{T \cdot \log(10)} + D\right). \tag{2.10}$$

Figure 2.8 shows the modeled total thermal conductivity of a void in an ice sample with the latent heat thermal conductivity and the radiative thermal conductivity.
Here, the geometry of the two planes is used as an approximation for the real pore space. The latent heat transport dominates after approximately 175 K, leading to a significant increase in thermal conductivity for much lower temperatures where the contribution from gas diffusion is still negligible as shown above.

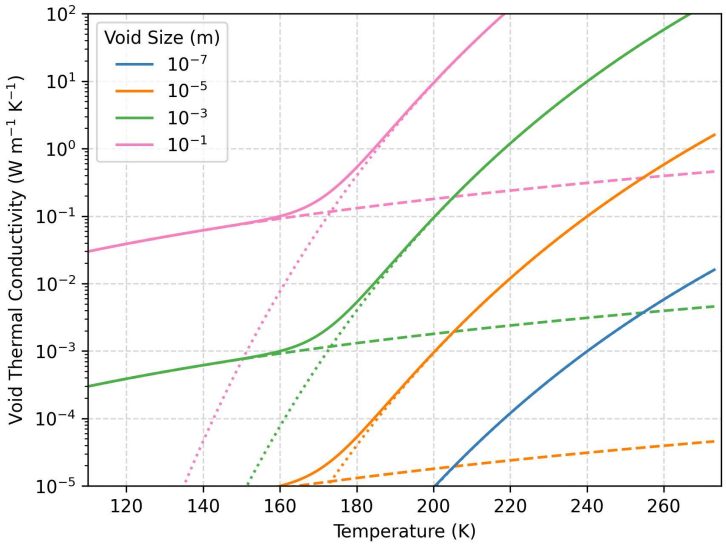

Figure 2.8.: Void thermal conductivity of an ice sample for different void sizes. The dashed lines represent the thermal conductivity due to radiation, while the dotted lines represent the conductivity due to latent heat. The size of the void space drastically increases the thermal conductivity.

2.2.3. Thermal Diffusivity and Specific Heat

In addition to thermal conductivity, thermal diffusivity may also be used to classify heat transport through granular media. Thermal diffusivity a is defined as the ratio between the thermal conductivity λ of a material to its volumetric heat capacity c_V:

$$a = \frac{\lambda}{c_\mathrm{V}} = \frac{\lambda}{\rho_\mathrm{bulk} c_\mathrm{P}} \,. \tag{2.11}$$

In other words, it describes how well a material is able to conduct heat in comparison to its ability to store it. The volumetric heat capacity $c_\mathrm{V} = \rho_\mathrm{bulk} c_\mathrm{P}$ depends on the bulk density ρ_bulk and the specific heat capacity c_P of the material it is composed of. Granular media exhibit a reduced bulk density, which results in a diminished capacity to store heat per unit volume relative to a solid sample, since the specific heat capacity is a material property.
In the case of lunar regolith, the specific heat capacity was fitted by Hayne et al. [18] to Apollo data and Diviner remote sensing data with a fourth-order polynomial as given by Equation 2.12:

$$c_\mathrm{P} = c_0 + c_1 T + c_2 T^2 + c_3 T^3 + c_4 T^4 \,. \tag{2.12}$$

The fit parameters are listed in Table 2.2. This fit does not apply to temperatures approaching absolute zero, where it becomes negative. However, it is sufficient for the temperature ranges analyzed in this work.

Table 2.2.: Specific heat fit parameters c_i for lunar regolith in units of $\mathrm{J\,kg^{-1}\,K^{-(i+1)}}$ [18].

c_0	c_1	c_2	c_3	c_4
-3.6125	2.7431	$2.3616 \cdot 10^{-3}$	$-1.2340 \cdot 10^{-5}$	$8.9093 \cdot 10^{-9}$

3. Icy Regolith Simulant

Due to the lack of in-situ observations on the Moon, the use of icy regolith simulants is essential for understanding the potential behavior of icy regolith materials. The simplest way to create an icy regolith simulant requires only two components. A regolith simulant that can be made from terrestrial minerals and, of course, water ice. Although other volatiles, such as hydrogen sulfide (H_2S), ammonia (NH_3), and carbon dioxide (CO_2), have been identified in permanently shadowed regions [4], water is the most abundant.
This chapter provides a short summary of established types of icy regolith simulants and the concept utilized in this work in Section 3.1. The following Sections 3.2 and 3.3 present the regolith simulant and ice simulant used to produce the novel microgranular icy regolith simulant as described in Section 3.4. Here, several different production methods are discussed, that result in different outcomes in terms of homogeneity. The final Section 3.5 briefly summarizes the production process of an additional mudpie icy regolith simulant.

3.1. Types of Icy Regolith Simmulants

The morphology of lunar ice is not well understood to this date. There could be amorphous and crystalline ice deposits, scattered in the sub-surface or concentrated in permanently shadowed regions. If ice occurs in the upper layers of the surface, space weathering most certainly affected its morphology over the past hundreds of million years in a similar way to the regolith grains, possibly creating similar grain shapes and sizes. Additionally, temperature changes, if they occurred during this period, could have further altered the morphology of the ice. Sublimated water may have been redeposited on adjacent extremely cold regolith grains, resulting in the formation of various types of growth structures or interconnected systems.
As reviewed by Ricardo et al. [19], several approaches are already known to literature for the creation of a material that might resemble lunar ice deposits.

Mudpie

The simplest way to create an icy regolith simulant is to gradually freeze a mixture of liquid water and regolith simulant. This mixture is often referred to as mudpie due to its resemblance to wet sand or mud. As this process includes liquid water, it is not possible to occur on the lunar surface. However, the resulting material is composed of a pore-filling matrix of ice between the regolith grains, resembling a fused subsurface ice deposit on the Moon. In addition to the simple production process, this method is capable of achieving accurate ice contents with high reproducibility, as exact amounts of water can be added to the dry regolith simulant. Depending on the ice content, the structural and thermal properties of the initial highly porous regolith are expected to change drastically.

Condensation Frosting

Another approach to create an icy sample can be realized by exposing a precooled regolith simulant sample to humid air, as water droplets condense on the material and freeze. With this method, dendrite-like macroscopic structures can be created on the regolith grains. The process can be done with ease, but analogous to the mudpie, liquid water is not present on the lunar surface, and therefore similar ice structures are not expected to occur on the Moon. Additionally, the precision with which the water ice content can be controlled is less than that achievable with the mudpie.

Deposition

Instead of using water droplets, gaseous water can be deposited onto cold regolith directly, which is a process that could exist on the lunar surface as well. The geometry of the resulting ice depends strongly on the vapor gradient within the granular sample, which in turn depends strongly on grain curvature and temperature gradients. Since these two parameters are hard to control in a laboratory environment, reproducible results are quite complex to achieve. The resulting materials often have tendril-like structures or ice necks that grow over time between the regolith grains.
Similarly, water ice can also be deposited indirectly. For example, ice can be heated in close proximity to a cold grain surface, where water can migrate through the pore spaces of the regolith sample and deposit to form secondary growth structures or layers. Tendril-like structures arise when the sample is exposed to very high-temperature gradients, and ice necks rather form when grain curvature influences vapor gradients more than temperature gradients do. A similar kind of process might be present on the Moon, where diurnal temperature changes could lead to sublimation of ice and re-deposition on adjacent cold grains, for example at the edges of permanently shadowed regions or in lower layers of the surface, where the diurnal temperature changes lead to the migration of water as recently modeled by Reiss et al. [20].

Quenching

An alternative method of producing an icy regolith simulant is to utilize a high cooling rate. For example, water-coated regolith grains can be dropped into liquid nitrogen to freeze them, creating a granular but fused icy regolith simulant [21]. Similarly, water droplets can be quenched directly and mixed with the regolith simulant to create a granular unfused icy regolith simulant. This method creates a sample that resembles the micrometeorite bombardment on the Moon by scattering the ice discretely in the sample. The quenching process itself is highly reproducible, resulting in ice particles with consistent morphology.
Granular icy samples can also be re-cemented later on by utilizing temperature or pressure changes to increase strength and form large-scale connected systems. This method allows for the recreation of highly irregular and porous particles, referred to as iceglutinates, which are assumed to be present on the Moon.

Comminution

A very different approach to simulate the lunar material is to crush water ice into small particles before mixing them with a regolith simulant. Like the quenching method, this process aims to recreate the effect of millions of years of space weathering and the resulting angular particle shapes. In practice, the exact shape and size of the crushed particles are hard to control and greatly influence the material's properties, which makes samples created by this method not easily reproducible. Crushed ice particles are often a few millimeters in size, much larger than the regolith grains on the lunar surface. These samples can also be exposed to temperature or pressure changes, altering the structure after production. One example material resulting from such an alteration process is a pressure-sintered icy regolith simulant as created by Johnson et al. [22] with an increased mechanical strength.

This Work

In this work, the quenching method is utilized to create spherical-shaped microgranular ice particles which are intermixed with a regolith simulant to create an unfused microgranular icy regolith simulant as illustrated in Figure 3.1.

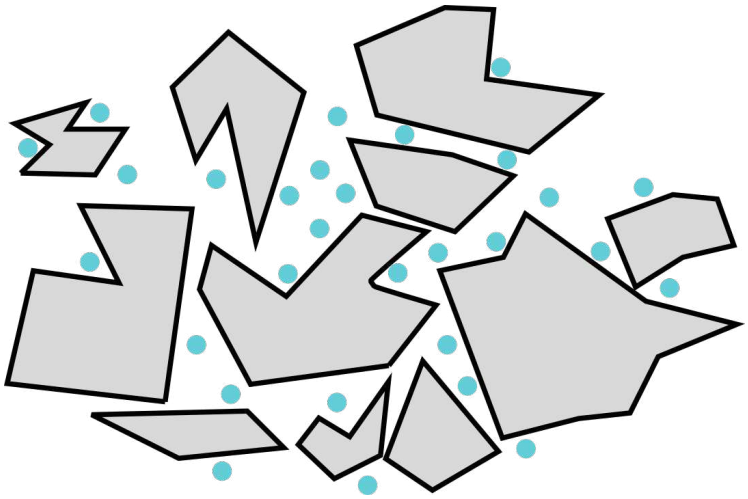

Figure 3.1.: Illustration of the unfused microgranular icy regolith simulant. Spherical ice particles are intermixed with the highly irregular regolith simulant grains.

Although the spherical shape of the ice particles might not occur on the lunar surface, the discrete distribution of ice between the angular regolith grains aims to recreate the effects of space weathering. In particular, impact gardening could result in the distribution of ice particles over broad ranges, leading to their intermixing with the regolith.
Depending on the ice content, this unfused granular material should exhibit minimal thermal conductivity compared to fused or embedded ice. Since thermal conductivity measurements are done over a broad range of temperatures, secondary effects due to sublimation and deposition occur as well, simulating temperature changes on the lunar surface and possibly re-cementing the granular sample.

An additional mudpie sample is utilized to compare the properties of this novel simulant to a sample with initially fused water ice. It is anticipated that an interconnected matrix of water ice and regolith grains results in a significant change in the thermal properties compared to a granular sample.

3.2. Regolith Simulant

A variety of simulants are available for use in the commercial market to simulate the space-weathered, highly porous surface of the Moon. These simulants often differ between mare and highlands materials, based on the properties of the returned Apollo samples. The mare simulants are created with a larger basalt content, while the highlands simulants consist mostly of plagioclase-rich anorthosite. The following sections describe the properties of the simulants used for this work, which are mainly resembling the highlands material.

3.2.1. LHS-1

One of these simulants is the high-fidelity lunar highlands simulant LHS-1, produced by Exolith Lab (Orlando, Florida) [23]. It is mainly composed of 74 % anorthosite and 24 % glass-rich basalt, while the exact mineralogical compositions and chemical constituents are listed in the appendix in Tables A.1 and A.3. The resulting mixture has an uncompressed bulk density of $1.30\,\mathrm{g\,cm^{-3}}$ with a porosity of 52.7 %. The individual particle material density is $3.24\,\mathrm{g\,cm^{-3}}$, as derived from the chemical composition and the individual material densities of the constituents [13]. On a macroscopic scale, the simulant appears as a fine gray powder, as shown in Figure 3.2.
The microscopic appearance of LHS-1 is displayed in Figure 3.3, which shows a Scanning Electron Microscope (SEM) image of the highly angular particles. As visible in the image, LHS-1 exhibits a broad particle size distribution, where the largest particles are often coated with much smaller ones. The particle sizes range from $< 0.04\,\mu\mathrm{m}$ to $1000\,\mu\mathrm{m}$ with a mean particle size of $90\,\mu\mathrm{m}$ and a median size of $60\,\mu\mathrm{m}$.

3.2.2. Lunex Simulant

Another simulant used in this work is made by Lunex Technologies (Berlin) [24]. It is made of a mixture of two commercially available products, the TUBS-T (75 %) and LX-M (25 %) simulants, resembling a mixture of highlands and mare regolith. The uncompressed bulk density of 1.24 $\mathrm{g\,cm^{-3}}$ is slightly lower in comparison to that of LHS-1. The size distribution is not as resolved as that for LHS-1, but shows a similar trend with particles in the range of $<10\,\mu\mathrm{m}$ to $1000\,\mu\mathrm{m}$ and a median particle size of $61\,\mu\mathrm{m}$.
The mineral and chemical compositions are listed in Table A.2 and Table A.3 respectively. The mass fractions of the oxides are comparable to those of LHS-1, with only minor discrepancies in the lower percentage range, resulting in the same material density of $3.24\,\mathrm{g\,cm^{-3}}$.

Figure 3.2.: A small pile of LHS-1 appearing as a fine gray powder with some darker grains [23].

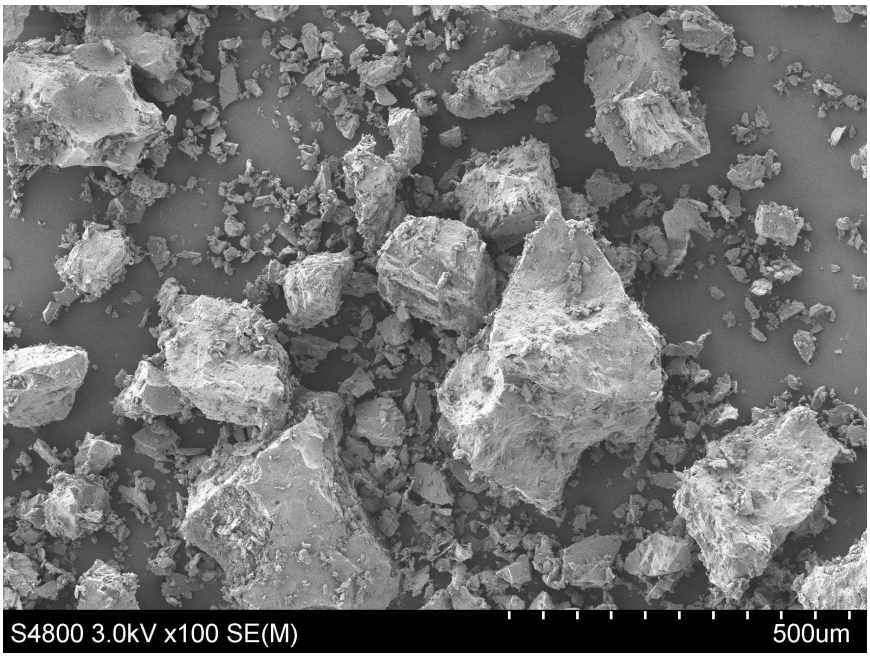

Figure 3.3.: SEM image of LHS-1, provided by C. Kreuzig [personal communication, June 2024]

3.3. Ice Simulant

To simulate the result of the micrometeorite bombardement on the lunar ice, unfused granular water ice particles are used. These particles were initially created as an analog material for cometary physics experiments by Kreuzig et al. [25] but can also be used to simulate lunar water ice. This section briefly summarizes the production process and the characteristics of this ice simulant.

3.3.1. Production Process

A mist of micrometer-sized water droplets, produced by a piezoelectric water atomizer submerged in distilled water, is directed into a dewar filled with liquid nitrogen. Upon contact, the water droplets are quenched and freeze instantly to form spherical ice particles. The resulting suspension of ice particles in liquid nitrogen can then be dried with a desiccator where the liquid nitrogen is evaporating slowly to form a dry powder of water ice particles. This powder can be weighed and used to mix with the regolith simulant. Alternatively, the liquid nitrogen-ice suspension may be used for mixing purposes as well.

3.3.2. Ice Particle Characteristics

The water ice particles are unfused and spherical in shape, as visible in the Cryo-SEM image in Figure 3.4. They exhibit a well-defined size distribution, with a median particle radius of (2.4 ± 0.1) µm and 80 % of all particle radii within the interval of (1.4 ± 0.1) µm to (3.7 ± 0.1) µm.

On a macroscopic scale, the ice particles appear as a white powder, similar in appearance to powdered sugar as illustrated in Figure 3.5. The particles tend to form agglomerates as a result of the adhesive forces between them. These agglomerates can reach sizes of up to multiple millimeters when the ice sample is moved but can be broken into smaller pieces with some force. The agglomeration is not present in the liquid nitrogen-suspended samples, as shown in Figure 3.6. Directly after production, the ice particles are discretely distributed in the liquid.
The volume filling fraction of the desiccated granular water ice was measured to be in the range of 0.21 to 0.35 depending on the size of the container.

3.3.3. Storage

The suspension of ice and liquid nitrogen can be stored in a dewar as long as enough liquid nitrogen covers the material. It is important to note that if the nitrogen level drops too low, the ice particles start agglomerating, which may render the suspension unusable for later applications.
In the desiccated form, the particles can be stored in cryogenic storage cans or directly in the desiccator, avoiding changes due to temperature-driven effects, such as sintering, keeping the temperature below 110 K at all times.

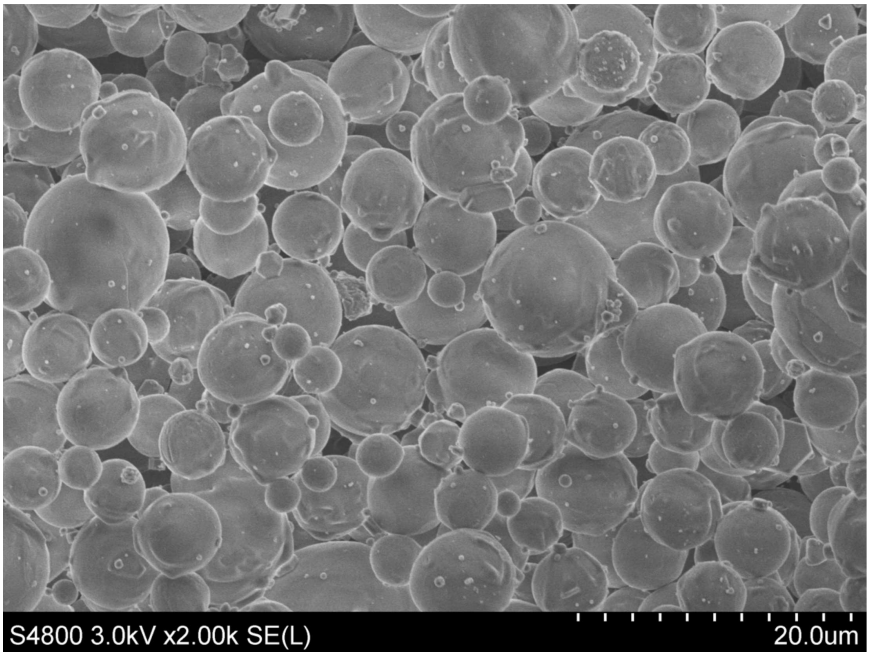

Figure 3.4.: Cryo-SEM image of microgranular water ice particles [25].

Figure 3.5.: Desiccated water ice particles in a metal bowl. In the sample, numerous agglomerates of up to a few millimeters in size are visible. The diameter of the bowl is approximately 125 mm.

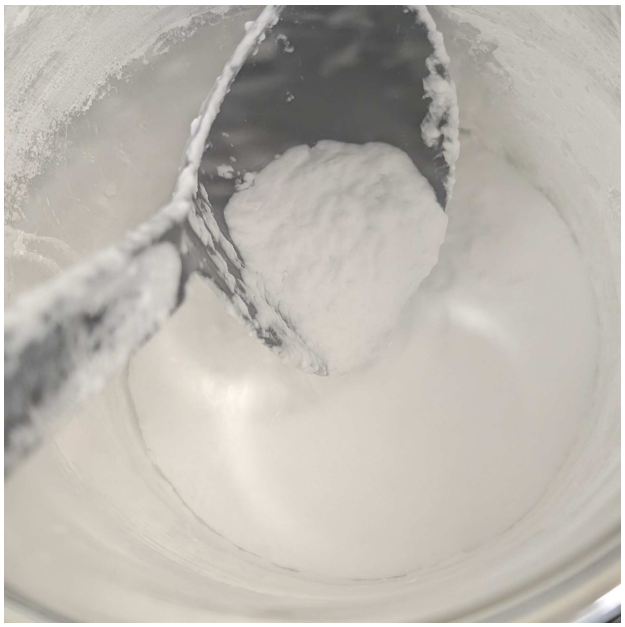

Figure 3.6.: Liquid nitrogen suspended ice particles. The picture shows a view into the Dewar with a ladle moving some ice particles suspended in a small amount of liquid nitrogen, appearing as a slushy white mixture.

3.4. Microgranular Icy Regolith Simulant

To create a microgranular icy regolith simulant, the regolith simulant and the ice simulant have to be mixed in a consistent manner. Condensation, frost formation, and ice agglomeration must be avoided during the mixing process in order to achieve a controlled water ice content and to create a homogeneous sample. Although high homogeneity might not be present in lunar ice deposits, it is advantageous to start with homogeneous samples to reduce the number of free parameters that might influence the thermal conductivity. For example, if the ice agglomerates, the nature of the micrometer-sized ice particles changes, and the thermal conductivity likely increases.
This section provides an overview of the preparatory steps necessary for the reproducible production of a microgranular icy regolith simulant, as well as the setup utilized for the mixing process, as detailed in Section 3.4.1. Section 3.4.2 presents various methods of mixing that have been investigated, which have yielded different results in terms of homogeneity and granularity. Finally, Section 3.4.3 presents the micro-granular icy regolith simulant as prepared for the experiments presented in Chapter 6.

3.4.1. Preparation

In order to create a sample with a reliable ice content and to avoid the influence of any additional water in non-granular form, the regolith simulant has to be dried before usage for any experiments. Under laboratory stable conditions, the adsorption of water from air humidity can lead to a water content of 0.1 wt % to 0.5 wt %, depending on the environment. As recommended by NASA [26], a simulant sample is dried at 110 °C for a minimum of 12 hours.
After this period, it is transferred directly into a dry atmosphere or vacuum, since the water

adsorption from the humidity takes place in the first few minutes of exposure to humid air. After approximately 20 minutes, a typical sample exhibits a water content of $(0.20 \pm 0.05)\,\mathrm{wt\,\%}$ as measured by weight gain in a regular laboratory atmosphere.
The dried regolith can now be utilized for experiments. If needed in a cooled state, it is placed within a metal container in a bath of liquid nitrogen as shown in Figure 3.7. The evaporating nitrogen provides a dry atmosphere with a slight overpressure during the entire process, minimizing the adsorption of water. The sample is covered with an aluminium foil to avoid liquid nitrogen from directly entering the warm sample, as this leads to outbursts of dust with evaporating nitrogen. The entire setup is situated within a glovebox to provide additional protection from the outer atmosphere and to contain any airborne dust particles. With this setup, no frost formation was evident throughout the entire cooling period as long as enough liquid nitrogen was present.

While cooling the regolith sample to cryogenic temperatures below 100 K, it is crucial to avoid any exposure to humidity or laboratory air, as frost can form in a matter of seconds. The icy sample production is therefore carried out with the same setup, minimizing transportation times and providing a cold and dry atmosphere for the entire mixing process.
Given that samples created in this study are on the order of a few hundred grams, small tools such as spoons, a ladle, or a metal sieve are used. All tools are precooled in a bath of liquid nitrogen before use.

3.4.2. Methods of Mixing

Initially, the regolith simulant was mixed with desiccated ice particles directly, as the precise mass of the ice can only be accurately determined if no liquid nitrogen is present. Thereby, samples with a predefined ice content were produced.

Figure 3.7.: Setup for the cool-down process of regolith simulant samples. Liquid nitrogen cools the metal sample container (covered with aluminium foil, approx. 20 cm wide) and provides a dry atmosphere. The entire setup is located in a glove box to further limit the influence of humidity.

As explained in Section 3.3.2, the desiccated particles tend to agglomerate as they collide with each other, making it difficult to produce a homogeneous micro-granular icy regolith simulant.

In a first approach, the desiccated ice particles were added directly to the precooled regolith, resulting in a multitude of agglomerates as shown in Figure 3.8. As ice particles are coated with dust particles upon contact, the agglomeration could be reduced slightly by adding small amounts of ice at a time and stirring carefully. Additionally, agglomerates could be crushed with some force, however, generating smaller agglomerates, which are not micro-granular in nature.
The addition of liquid nitrogen to the mixture of desiccated ice particles and regolith simulant did not contribute to a smaller number of agglomerates.
Since the agglomerates can be broken up with some force, an automated approach using a whisk attachment on a power tool was tested, as shown in Figure 3.9. With the addition of liquid nitrogen to aid stirring, there was no significant reduction in the number of agglomerates. However, the size of the largest agglomerates could be reduced to approximately 1 mm.
Another method was employed by re-suspending the desiccated ice particles in liquid nitrogen after the mass was determined. This approach was utilized to dissolve the agglomerates back into micro-granular particles, which was only partially successful, as some agglomerates are so tightly bound to each other that they do not break or dissolve easily. As illustrated in Figure 3.10 an ice sample prepared in this way still displays several agglomerates, albeit smaller in size. For the purpose of homogeneity, this approach yields the best results yet.
A very different approach to creating an evenly distributed icy regolith sample is to first sieve the desiccated ice particle, enforcing the formation of agglomerates, as this creates a well-defined particle size. Once in contact with the finest dust particles, the sieved agglomerates can be stirred into the regolith without further agglomeration. Figure 3.11 shows this process for two different

Figure 3.8.: Agglomerates in an icy regolith simulant sample mixed with desiccated ice particles and without liquid nitrogen. The largest agglomerates visible here are approximately 4 mm in size.

Figure 3.9.: Whisking of an icy regolith simulant with agglomerates with a power tool has no significant effect on the number of agglomerates. The largest ones seem to break into smaller ones of approximately 1 mm in size.

Figure 3.10.: Resuspended ice particles in liquid nitrogen. After stirring and breaking agglomerates with force, many smaller ones are still present in the sample.

Figure 3.11.: Desiccated ice particles sieved onto a dry regolith simulant sample with a sieve opening of 250 µm (left) and 1000 µm (right). The sieved ice particles can be distributed evenly and can be made much smaller than the unsieved agglomerates (left bottom).

sieve sizes of 250 µm and 1000 µm.
For sieve openings of smaller size, it is considerably harder to achieve an appropriate mass throughput to create samples with a few ten grams of ice. Consequently, this method may only be utilized to create samples with either a very low ice content or with larger ice particles. Furthermore, the mass loss on the sieve must be accounted for, which results in a larger uncertainty in the water content determination in comparison to the previous methods.
The resulting mixtures are homogeneous samples, although the microgranular nature of the ice is no longer evident, as the sieved agglomerates are now much larger in size.

In conclusion, the mixing of a regolith simulant with desiccated ice particles produces mostly inhomogeneous results due to the agglomeration of the micrometer-sized ice particles. The number of particles involved in the formation of the agglomerates and the degree of intermixing of residual particles with the regolith simulant remain unknown. However, the presence of the larger agglomerates has resulted in a loss of the micrometer-sized nature of the ice particles, which is contrary to the objective of this work, which is to create a microgranular icy regolith simulant.

The agglomeration of the ice particles can be avoided only if the particles are utilized in the freshly produced state, suspended in liquid nitrogen. In liquid nitrogen, the particles do not stick to each other. With this method, the mass of the ice can not be determined, but the nature of the micro-granular particles is preserved.

3.4.3. Micro-Granular Sample Production

To create a micro-granular icy regolith simulant from the freshly produced ice particle liquid nitrogen suspension, the regolith is first mixed with an appropriate quantity of liquid nitrogen to achieve a consistency comparable to that of mud. Subsequently, the ice suspension is added in incremental quantities to prevent any forms of agglomeration, which is shown in Figure 3.12. During this process, dust particles rapidly coat the ice grains.
In order to determine the mass of the produced sample, it is necessary to boil off the liquid nitrogen prior to the insertion into the vacuum chamber for thermal conductivity measurements. During this process, the sample is maintained in the dry and cold environment until the mass stabilizes at a point where all the liquid nitrogen has boiled off.
Figure 3.13 shows two samples produced in such a way, where no visible trace of the added ice can be found. This is due to the absence of any agglomerates and the coating of the micro-granular particles with dust.
Since the water content cannot be determined beforehand with this method, it is inferred using the method described in Section 3.4.4. The two samples shown here exhibited a relatively low water content of 2.9 wt % and 7.7 wt %. With significantly larger ice contents, the macroscopic appearance changes to a point where the mixture is much lighter in color. This is due to the fact that not all ice grains are coated by regolith, which consequently affects the overall appearance.
Following the complete desiccation of the liquid nitrogen from the sample, larger regolith clumps occurred. The formation of these clumps is a consequence of the wetting of the material with liquid nitrogen, which results in some degree of compaction. The clumps were dissolved by stirring the sample after desiccation.
By measuring the volume and mass of these samples with known material densities, the volume filling fractions were determined to lie in the order of 0.3 to 0.5, although further compaction was possible as well. Here, a constant material density of ice of $0.917\,\mathrm{g\,cm^{-3}}$ was utilized for the calculations [13].
In general, the low ice content simulant's behavior is very similar to that of the dry regolith, with the exception that almost no dust is produced when the icy material is moved. After a sample is heated and dried completely for the ice content measurement, dust is again present, which indicates that the ice particles bind most of the smallest regolith grains.

The homogeneity of the samples prepared with the liquid nitrogen-suspended ice particles is visibly much larger than that of samples made from desiccated ice particles. For this reason, the method is used to create the unfused microgranular icy regolith samples analyzed later in this work.
As this study does not include a microscopic analysis of the prepared samples, it would be beneficial to further evaluate the influence of the mixing process on the morphology and homogeneity of a sample by conducting such an analysis in the future.

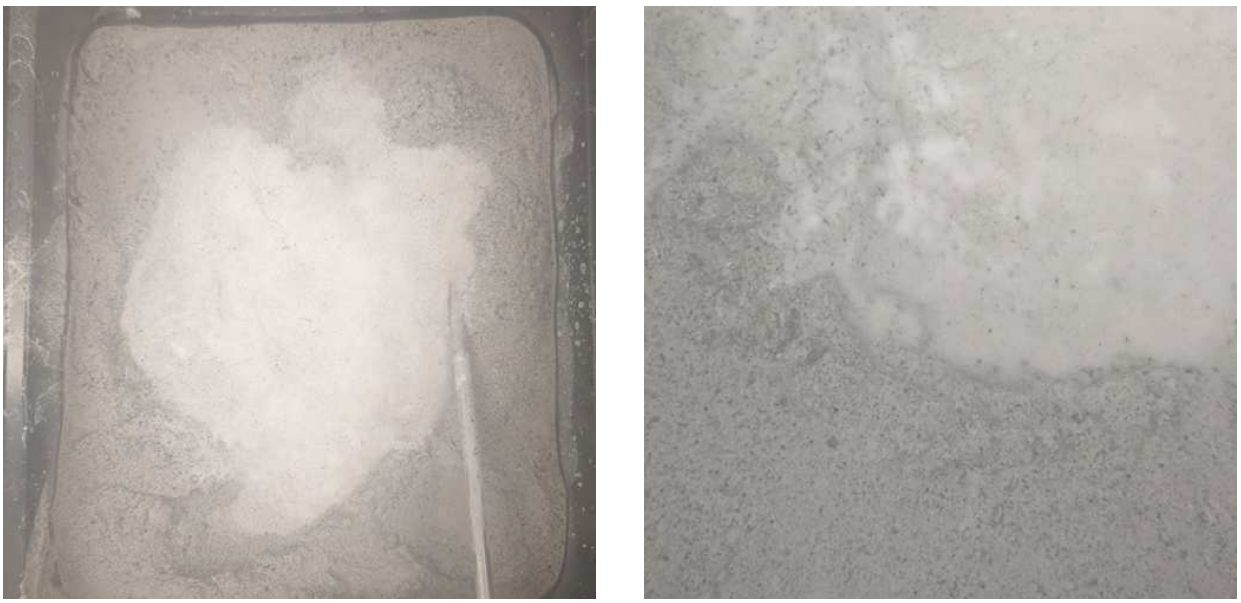

Figure 3.12.: Suspension of liquid nitrogen and ice particles in the regolith simulant (left) and a closeup of the white ice suspension (right). No agglomerates are visible even after mixing. The tray shown here is 20 cm wide, while the right frame shows a surface approximately 3 cm wide.

Figure 3.13.: Microgranular icy regolith simulant samples with an ice content of 2.9 wt % (left) and 7.7 wt % (right) after most of the liquid nitrogen evaporated. No major trace of ice agglomeration is evident in those approximately 7 cm and 5 cm wide frames, indicating a mostly homogeneous mixture.

3.4.4. Measuring the Water Ice Content of an Icy Sample

To measure the water ice content of a sample after it is produced, it is dried in an oven. By measuring the mass before and after drying, the water content that was present in the sample before can be derived in the form of Equation 3.1:

$$c_{\text{water}} = \frac{m_{\text{water}}}{m_{\text{total}}} = \frac{m_{\text{before}} - m_{\text{after}}}{m_{\text{before}}} \,. \tag{3.1}$$

If the material was mixed with liquid nitrogen during the production process, it is necessary for the nitrogen to evaporate prior to weighing the sample to prevent any deviation from residual nitrogen mass. As this process takes time, the sample is kept in the cool and dry environment to maintain its properties. To ensure that all liquid nitrogen has evaporated, the sample is weighed and if the mass remains constant, it may be dried.
Since this method of determining the water content destroys the icy samples, it is not performed on the entire produced batch but on smaller samples. If the batch is sufficiently homogeneous in relation to the sample size, the average water content of the smaller samples can be used as an estimate for the entire batch. If the batch is not homogeneous, the average value might not reflect the total water content, and either more or larger samples have to be used.

3.5. Mudpie Icy Regolith Simulant

The creation of a mudpie simulant is a relatively straightforward process in comparison to the micro-granular one. A dried regolith simulant sample is placed in a dry environment. Demineralized water is added by weight and thoroughly mixed, resulting in a sample with a highly reproducible water content. This sample appears like wet sand or mud, as shown in Figure 3.14, depending on the amount of water added.
If only small amounts of water are present, the regolith tends to clump together, creating larger agglomerates of regolith similar to the above-mentioned process with liquid nitrogen. Consequently, small volume filling fractions of 0.3 are realizable, as these clumps are more compact. The addition of even more water results in further compacted samples as air pockets are filled with water. Here, the saturation point has to be considered, which is situated at approximately 20 wt % for LHS-1, which was determined with a drip experiment. In laboratory conditions, the addition of further water results in water leakage and, consequently, the formation of a non-homogeneous mixture.
By freezing the wetted regolith simulant, a mudpie icy simulant is created. At this point, it is especially important to ensure that the sample is not exposed to humidity to prevent the formation of additional frost.

Figure 3.14.: Mudpie simulant prepared by mixing the regolith simulant with demineralized water with a water content of 2.9 wt % (left) and 23.1 wt % (right) resembling wet sand and mud respectively. The additional water visible on the right side of the image is a result of the sample being over-saturated with water. The samples shown here are not frozen yet.

4. Experimental Setup

To measure the thermal conductivity of dry and icy regolith simulants in an environment that resembles the conditions on the lunar surface, temperature and pressure must be regulated. For this purpose, a Thermal Vacuum Chamber (TVAC) is utilized with a liquid nitrogen cooling system and an electrical heating system. This chapter describes the infrastructure utilized in the form of the thermal vacuum chamber and sample holder in Section 4.1 and additional measurement and control devices in Section 4.2. Section 4.3 focuses on the software implemented for the control of the temperature of the sample holder and the automation of thermal conductivity measurements.

4.1. Thermal Vacuum Chamber

The TVAC used for this work is shown in Figure 4.1. It is capable of providing temperatures of approximately 100 K to 500 K as well as low pressures down to 10^{-6} mbar by using a setup of two pumps. A prepump creates an initial vacuum of $<10^{-1}$ mbar, which is then further reduced by a turbomolecular pump to reach the lower regimes of down to 10^{-6} mbar. The pressure inside the TVAC is measured with a Pirani vacuum gauge attached to the back of the chamber. The TVAC is equipped with a quick-access lid, enabling a fast change of samples.
Venting can be done via two valves. One specifically intended for argon or nitrogen to create a dry but pressurized environment, and another one for atmosphere venting.

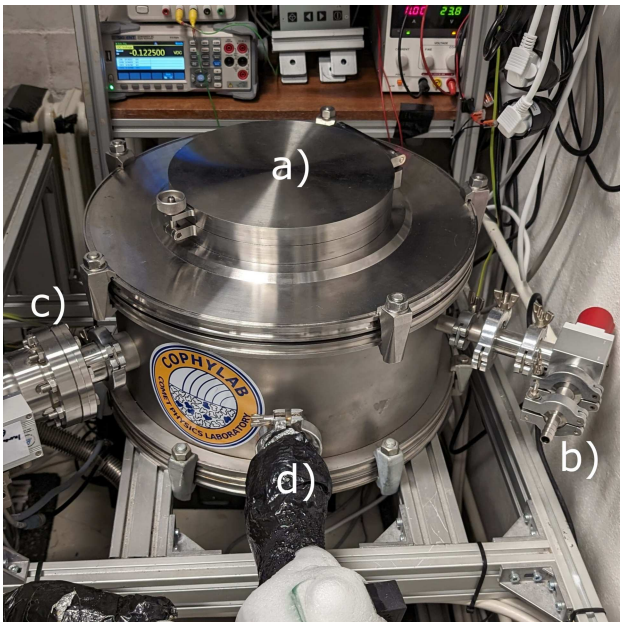

Figure 4.1.: TVAC with quick-access lid (a), venting valve (b), pump connection (c), a pressure sensor (not visible here), electrical throughput (not visible), and a liquid nitrogen throughput (d) with a solenoid valve.

With an electrical throughput on the back of the chamber, the heating system and sensors are connected to the power supplies and measurement devices. The cooling system on the other hand is controlled via a solenoid valve attached to a liquid nitrogen supply pipe. Via copper tubes, the liquid nitrogen runs through the chamber and exits into a Styrofoam box situated below the chamber, resembling a flow cryostat.

4.1.1. Sample Holder

The TVAC contains a cylindrical sample holder made from aluminium as shown in Figure 4.2 with an inner diameter of 16 cm and an inner height of 4.8 cm. The outer wall is 2 cm thick.
To regulate the sample holder's temperature, the liquid nitrogen pipes of the cooling system are embedded in its outer wall, and multiple heating foils are attached to the bottom, lid, and side wall of the sample holder. This configuration enables an active cooling system in combination with a Pt-1000 sensor measuring the temperature of the sample holder. An additional Pt-1000 sensor is installed outside the TVAC at the exhaust pipe of the liquid nitrogen system to prevent overflow of the coolant.
The lid of the sample holder is not actively cooled but can be screwed tight to the outer wall with inlets for the electrical wiring to improve thermal contact. If tightly screwed in place, these inlets are the only opening to the outer TVAC volume.
The liquid nitrogen copper pipe runs across the bottom and the lid of the sample holder, providing some degree of thermal insulation from the warm outer walls of the TVAC while keeping the inner volume accessible.

Figure 4.2.: Sample holder inside of the TVAC. The copper pipes of the cooling system run along and above the sample holder. There are three heating foils in total, one of which is visible on the lid next to the sample holder. The other two are attached to the inner bottom (not visible here) and inner side wall of the sample holder. A Pt-1000 sensor is located inside the aluminium wall.

To increase the thermal insulation even more, the sample holder is placed on screws with additional Tecapeek pieces underneath, which is a material with a low thermal conductivity of $0.27\,\mathrm{W\,m^{-1}\,K^{-1}}$ and high resistance to thermal stress [27]. This drastically limits heat transfer through contact points, reducing the amount of liquid nitrogen needed for cooling. Since there is no cooling shield installed, heat transfer by radiation remains possible, particularly impacting the non-actively cooled lid.
The internal volume of the sample holder of approximately $1000\,\mathrm{cm^3}$ provides a considerable amount of space, which is not always required. In particular, for thermally inert samples, such as many granular media, large sample sizes lead to longer experimental timescales. To minimize the duration of temperature changes within the sample, the effective sample volume can be reduced by incorporating a secondary aluminium tray within the sample holder. The remaining volume is filled with a granulate, in this case, aluminium, as illustrated in Figure 4.3. With a large solid conductivity of $23.7\,\mathrm{W\,m^{-1}\,K}$ [13], aluminium provides good thermal contact with the walls of the sample holder, even in a granular form. This thermally connects the sample to the cooling and heating system.
The aluminium tray configuration represents a cost-effective approach that enables swift temperature changes and provides a simplified method for inserting and removing a sample, as detailed in Section 4.1.2. This approach circumvents the necessity for the fabrication of an additional sample holder.

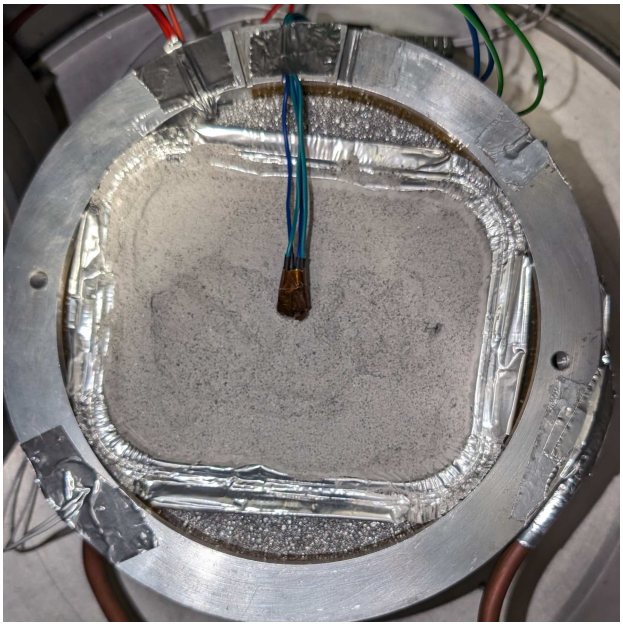

Figure 4.3.: Closeup of the sample holder with the secondary aluminium sample tray and a regolith sample prepared for a measurement with the measurement sensor in place. For good thermal contact, the remaining volume of the sample holder is filled with aluminium granulate.

4.1.2. Sample Insertion and Removal

A preliminary approach to inserting a sample was conducted without the secondary aluminium tray. In this approach, a sample with previously determined mass was poured into the volume of the sample holder through a funnel and distributed as evenly as possible within it. The measurement sensor was then inserted and the height and, thereby, the volume was measured with a caliper.
This method was deemed unsuitable for further measurements. First of all, the electrical charge of the regolith simulant particles causes them to adhere to surfaces, resulting in material loss as it sticks to the utilized tools. Additionally, a non-measurable amount of regolith is dispersed into the atmosphere during the pouring process, necessitating extended protective measures at the location of the TVAC and increasing mass uncertainty. Furthermore, evenly distributing a fine granular sample within a large volume is challenging, rendering a height measurement, and consequently the determination of bulk density and volume filling fraction, highly uncertain. The removal of a sample is also tedious and time-consuming. Lastly, direct contact between the regolith simulant and the heating foils can cause damage. The adhesive securing the foils cannot withstand cryogenic temperatures and fails if the foils are not in perfect contact with a flat surface such as the aluminum outer walls. Exposure of the foils directly to the regolith simulant allows some grains to move between the heating foil and the sample holder wall, weakening the adhesive and drastically reducing the thermal contact. This results in the deterioration and eventual failure of the heating foils.

Most of these problems were solved with the aluminium tray setup. Here, one tray is placed in the sample holder, holding the aluminium granulate in place, while a second tray is utilized to prepare the sample at a suitable location and insert it into the TVAC. Inserting the sample with the tray minimizes dust production, as this process only takes a few seconds. This also reduces the exposure to humidity, which is particularly important for precooled samples.
After insertion, the material surface is flattened, which can be done with slightly more precision due to the smaller surface area. However, some uncertainty remains, as a perfectly flat surface can not be produced. To introduce the vacuum, the chamber is slowly pumped to avoid alterations in the bulk density of the sample due to outbursts from air-filled pores.
Finally, the sample can be quickly removed by lifting the outer aluminium tray from the sample holder. This enables post-processing steps like drying or weighing of the sample, which were not possible with the initial method.

In addition to this procedure, the TVAC is flooded with cold nitrogen or argon throughout the entire insertion and removal process to reduce the influence of ambient conditions, especially humidity.

4.2. Measurement and Control Devices

In order to regulate the temperature within the chamber and to measure the thermal conductivity, a number of different devices are required. This section provides an overview of these instruments.

4.2.1. Transient Hot Strip

The main aspect of this work, the measurement of the thermal conductivity, is done with a Transient Hot Strip (THS). With a length of 7.2 cm and a width of 2 mm, the THS utilized here consists of a tightly wound copper wire embedded in a polyimide frame, as shown in Figure 4.4. The wire is used to insert heat into a surrounding sample by passing a current through it. At the same time, it serves as a resistance-based thermometer. With a configuration of four electrical contacts, the resistance of the THS can be measured by the voltage drop across it independently from the current supply, minimizing the influence of contact resistances. The precise functionality of the THS method is explained in Section 5.2.
The outer polyimide frame insulates the wire electrically and protects it mechanically from the surrounding sample. As shown by Figure 4.4, the polyimide layer is very narrow. In combination with a thermal conductivity in the range of $0.1\,\mathrm{W\,m^{-1}\,K^{-1}}$ to $0.2\,\mathrm{W\,m^{-1}\,K^{-1}}$ at 70 K to 300 K [13], this layer does not alter the outwards heat flow significantly. Furthermore, polyimide exhibits high thermal stress resistance, allowing measurements to be conducted at elevated and cryogenic temperatures.

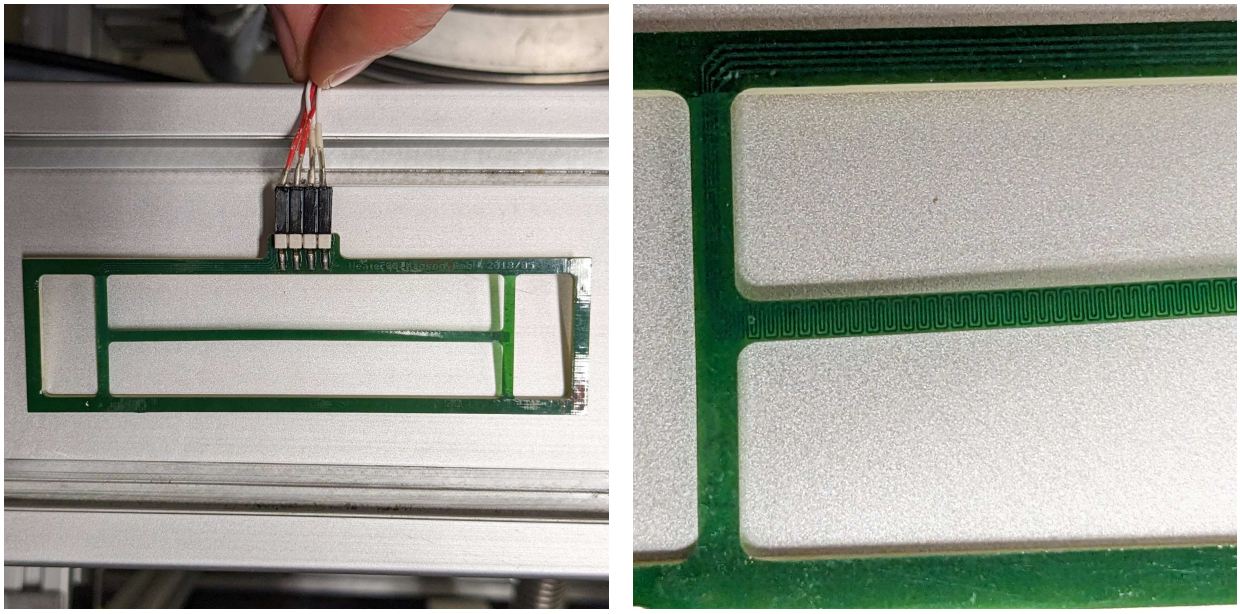

Figure 4.4.: THS made from a polyimide frame for stability and structure (left) and a copper winding to emit heat and measure the temperature (right).

4.2.2. Power Supplies

To power the THS, a programmable linear DC power supply is used to provide adjustable voltage and current. In the default low power mode, the current is set to 0.1 A and the voltage to 0.2 V. These values were selected as the result of a trade-off between the signal-to-noise ratio of the voltage reading of the THS. The noise increases with lower power due to a smaller signal strength. However, voltages can not be too large, as significant amounts of heat are emitted into the sample due to the resistive heating, which is not desired for an idle phase.
During a measurement, a high power mode is utilized for which the current is raised to 1 A while the voltage can be set to 1 V to 5 V, depending on the thermal properties of the sample.

A second power supply with a constant DC output of 24 V is used for the temperature control system, supplying the heating foils inside the sample holder and the solenoid valve for the liquid nitrogen outside of the TVAC. The power to those devices can be individually shut off and on via relays controlled by a programmable microcontroller.

4.2.3. Digital Multimeter

Measuring the temperature of the THS and the sample holder requires precision. For this purpose, a Siglent SDM3065X-SC digital multimeter is used, measuring the voltage drop across the THS. The current flowing through the THS is measured via the voltage drop across a 50 Ω shunt resistance located outside of the TVAC, resulting in the resistance and thereby the temperature of the THS as explained in Section 5.2.
Additionally, the digital thermometer measures the resistance of the Pt-1000 sensor located within the sample holder and the one situated within the exhaust pipe of the liquid nitrogen system, providing the data to actively control the temperature of the sample holder.

4.3. Control Software

To monitor and operate the entire system, a measurement and control software has been developed. Its primary function is to regulate the temperature of the sample holder and to execute measurements. The software interfaces the THS, the programmable power supply and the microcontroller used to activate the heating and cooling system. The Graphical User Interface (GUI) of this software is shown in Figure 4.5, which enables real-time monitoring and control of the setup. The software is capable of mostly automatic operation, executing measurements, and controlling the temperature throughout experiments, which may last for multiple weeks at a time.
The following sections provide a summary of the implemented Proportional-Integral-Derivative (PID) temperature control mechanism and the methods that automatically change the temperature and execute measurements.

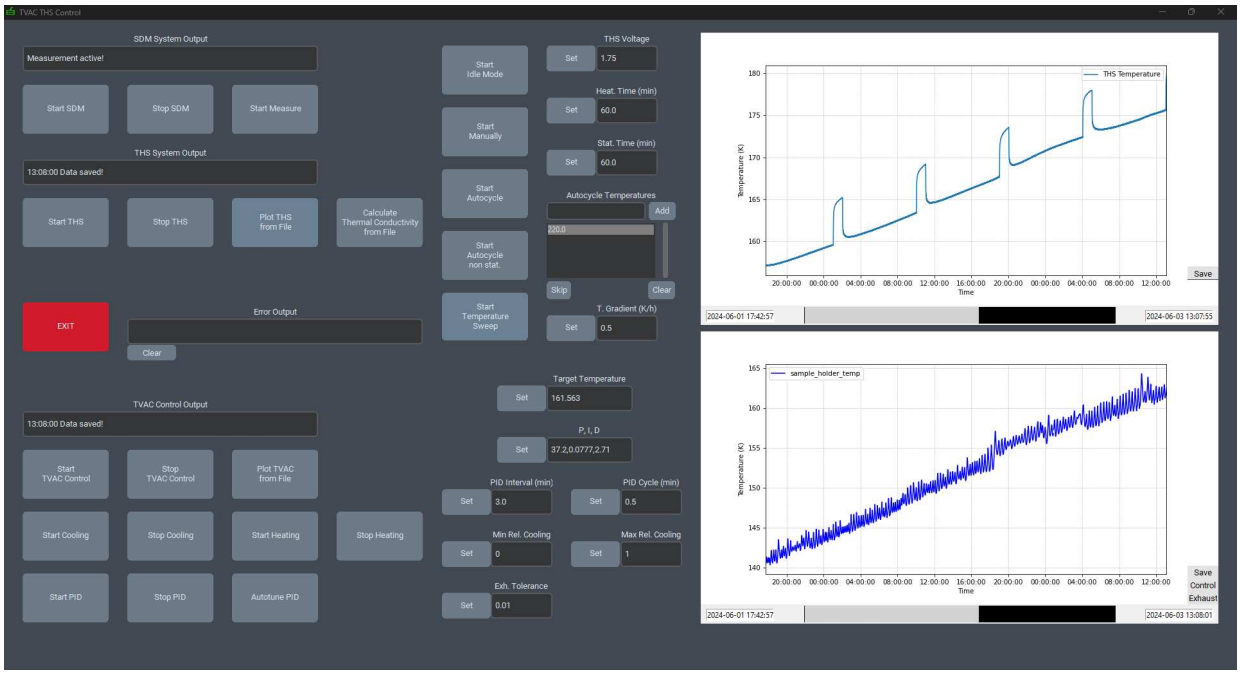

Figure 4.5.: GUI of the Python control software.

4.3.1. Temperature Control

The temperature of the system is controlled with the sample holder. Although manual control is an option, the temperature is mostly regulated by an automatic PID controller.

A PID controller uses three input parameters, namely proportional P, integral I, and derivative D. Together with the deviation of the current temperature to the targeted temperature $e(t)$ a strength signal $C(t)$ is computed which can be used to control the heating and cooling hardware. Equation 4.1 shows this strength signal with the time t, which may range from a certain start point t_i to the current time t_now:

$$C = P \cdot e(t_\mathrm{now}) + I \cdot \int_{t_\mathrm{i}}^{t_\mathrm{now}} e(\tau) d\tau + D \cdot \frac{\mathrm{d}e(t)}{\mathrm{d}t} \,. \tag{4.1}$$

While the heaters and liquid nitrogen supply are controlled by relays that are only capable of processing digital signals, the PID function returns an analog signal. It is therefore necessary to convert this signal to a duty cycle. For this purpose, the output value is scaled to an interval between -100 and 100 to resemble a percentage of the heating interval for positive values or the cooling interval for negative values. This percentage is then translated to a relative time for the corresponding system in which the cooling or heating will be activated. The time intervals for these calculations may be selected freely depending on the temperature response of the sample as well as the wear of the relays.
Since this PID function can only activate either the heating or the cooling system, additional minimal cooling or heating times are implemented to set limits to the duty cycle, providing a balance for possible fluctuations in the liquid nitrogen supply and transitional effects near $C(t) = 0$.
Since the selection of the PID parameters drastically changes the system's behavior, an automated

PID parameter tuning function has been implemented that utilizes a differential evolution to simulate the best possible parameters for a given target temperature.

When choosing the parameters manually, the controller is most strongly influenced by the P parameter. For values exceeding > 40, the controller is prone to overshoot the targeted temperature, particularly when the cooling system is used, given its comparatively lower responsiveness. Conversely, if the P parameter is chosen to be too small, the system may fail to reach the targeted value. With the I parameter, the oscillation around the targeted value can be controlled. If it is too large, the temperature will oscillate more strongly around the target. The D parameter finally influences if and how pronounced the oscillation will occur.
If all parameters are chosen in an ideal way, the temperature should not overshoot but quickly converge to the targeted value. Since the system's temperature response changes in different temperature intervals and for different samples, the parameters should be adjusted regularly to achieve ideal results.

4.3.2. Measurement Control

Once a given stable temperature is reached, a measurement with the THS may be conducted. Therefore, a user-specified voltage and a constant current of 1 A are applied to the THS to insert heat into the sample. For low thermal conductivity samples like regolith, 1.3 V is sufficient while higher thermal conductivities require higher voltages. When using a material with unknown thermal conductivity, the ideal voltage has to be found by trial and error until a temperature increase of 3 K to 7 K is evident to enable an accurate evaluation. The maximum voltage to not damage the THS is 5 V.
Upon completion of a measurement, which is specified by a fixed time interval, the THS returns to its idle and low power mode with 0.1 A and 0.2 V to continuously measure the temperature.
In addition to manual operation, these measurements can be conducted by automated scripts to enable consistent temperature control over extensive periods as described in the following sections.

Autocycle

With the autocycle mode, the PID controller is used to sequentially target temperatures that have been previously specified in a list. At each temperature, a measurement is initiated once the system has reached a stationary state. The recognition of such a state is achieved in by utilizing all temperature values within the most recent time interval with a specified length. To be considered as stationary, a temperature interval of 0.1 K around the average is defined. First of all, 90 % of all temperature values have to lie within this interval to account for noise. Secondly, by calculating the slope of the data, the extrapolated temperature should not exceed the interval within the next period of the same length. If both conditions are fulfilled, a stationary state exists and a measurement is performed automatically. Furthermore, the resulting temperature curve is evaluated automatically afterwards. In this mode, a second measurement will be performed after the first one to counter-check the result, which leads to an elevated certainty but comes with the cost of measurement time. If the results are in good agreement, the next temperature is targeted and the cycle begins again until all temperature steps have been reached.

Autocycle non stat.

Since approaching stationary states is highly time-consuming for low thermal conductivity samples, another approach was implemented, where only a time constraint influences the execution of a measurement. With this method, non-stationary measurements occur as well. As the evaluation of a measurement requires the knowledge of the temperature change due to the THS input power, any temperature changes induced by other factors must be subtracted as explained in more detail in Section 5.2.
Temperature changes can be done rather quickly, depending on the temperature values selected. On the one hand, this is very time-efficient. On the other hand, it might produce a higher measurement uncertainty based on the quality of the correction fit. Due to the temperature being unstable, the measurement is not repeated and compared. Additionally, if temperature steps are chosen too large, small changes in the sample's properties might not be observable.

Temperature Sweep

For the purpose of analyzing sample properties with a higher resolution in temperature while still utilizing the time benefits of non-stationary measurements, a temperature sweep was implemented. With this sweep, a constant temperature gradient can be set to the sample holder.
The target temperature is updated automatically once every minute to create a smooth gradient. Additionally, the PID parameters are tuned automatically every 10 K to maintain the accuracy of the controller. Similar to the previous mode, the measurements are conducted exclusively based on a time interval.
The set gradient simplifies the subtraction of the non-THS-induced temperature changes, but manual evaluation is still required to create a suitable fit. Similar to the autocycle modes, the measurements done with this sweep are prone to uncertainty if the temperature fit is not ideal as explained in Section 5.3.

5. Method and Evaluation

While measuring the thermal conductivity of any material, one is able to use either transient or steady-state methods. In this context, a steady state refers to the existence of a constant thermal gradient leading to a constant heat flow through the sample. If more than one temperature along this gradient is known, the thermal conductivity can be calculated quite easily.
In opposition to this stands the transient method, where a temporary temperature change based on a known heat source can be evaluated to determine the thermal conductivity of a material.

The transient method is more complicated to evaluate, however, it is used in this work due to its versatile usability. To reach prominent stationary gradients, for example, one has to control the temperatures of a heated and a cooled surface very precisely. Transient measurements can be performed in many situations, with the only condition being a precisely determinable heat flow during the measurement. A singular measurement is therefore in theory much quicker to realize with the transient method.
In this work, the transient hot strip is used to determine the thermal conductivity. The following Section 5.1 describes the theory behind this method, while Section 5.2 goes into detail on the measurement and evaluation process. Section 5.3 provides an assessment of the uncertainty of the resulting thermal properties.

5.1. The Transient Hot Strip Method

The THS method was originally developed by Gustafsson, Karawacki, and Khan [28] to simultaneously measure the thermal conductivity and thermal diffusivity of solids or liquids. By introducing a known quantity of electrical power through a thin metal strip with a known temperature resistance characteristic, heat can be inserted into the sample surrounding the strip while simultaneously measuring its temperature via a resistance measurement. The temperature response of the strip to this heating power gives insight into the thermal conductivity and thermal diffusivity of the sample surrounding it.
The main advantage of this method is the increased surface area of the strip with a very small thickness compared to, for example, a line heat source, often referred to as a transient hot wire. This allows for better thermal contact, especially when using granular materials such as regolith.

5.1.1. THS Theory

The THS is modeled as a metal strip of width D and length $L >> D$ surrounded by an isotropic dielectric at a given temperature $T(t)$ at time t. With a constant current I flowing through the strip and a voltage drop U across it, the strip emits a heat of $\phi = U \cdot I$ in radial direction. At the same time, it functions as a resistance thermometer with output voltage $U(T(t))$. Equation 5.1 shows the strip source solution from Gustafsson, Karawacki, and Khan [28] with the thermal

conductivity λ:

$$\Delta U(T(t)) = U(T(t)) - U_0 = \frac{\alpha U_0^2 I}{2\sqrt{\pi} L \lambda} f(\tau)\,. \tag{5.1}$$

Here, U_0 is the voltage drop at $t = 0$, α is the temperature coefficient of the electrical resistance of the strip and

$$\tau = \frac{\sqrt{4at}}{D} \tag{5.2}$$

is a non-dimensional time with thermal diffusivity a, which is utilized to express the time dependence of the THS signal $f(\tau)$, as given by Equation 5.3:

$$f(\tau) = \tau \mathrm{erf}(\tau^{-1}) - \frac{\tau^2}{\sqrt{4\pi}}\left[1 - \exp\left(-\tau^2\right)\right] - \frac{1}{\sqrt{4\pi}}\mathrm{Ei}(-\tau^{-2})\,. \tag{5.3}$$

A linearization of Equation 5.3 was done by Hammerschmidt and Sabuga [29] by applying a first-order Taylor series and a McLaurin series, yielding Equation 5.4:

$$f(\tau) \approx \frac{3-\gamma}{2\sqrt{\pi}} + \frac{1}{\sqrt{\pi}}\ln(\tau) + \frac{1}{12\sqrt{12}\tau^2}\,. \tag{5.4}$$

Here, $\gamma \approx 0.5772$ is Euler's constant. Incorporating this approximation into Equation 5.1 results in the approximated THS signal in the form of Equation 5.5:

$$U(t) - U_0 \approx \frac{\alpha U_0^2 I}{4\pi L \lambda}\left(3 - \gamma + \ln(t) + \ln\left(\frac{4a}{D^2}\right) + \frac{D^2}{24at}\right). \tag{5.5}$$

Using the thermometer equation $U = U_0(1 + \alpha T)$, this voltage signal can be translated into a temperature change

$$T(t) - T_0 \approx \frac{U_0 I}{4\pi L \lambda}\left(3 - \gamma + \ln(t) + \ln\left(\frac{4a}{D^2}\right) + \frac{D^2}{24at}\right) = m\ln(t) + n + R_2(t)\,. \tag{5.6}$$

With

$$m = \frac{U_0 I}{4\pi L \lambda} \tag{5.7}$$

and

$$n = m\left(3 - \gamma + \ln\left(\frac{4a}{D^2}\right)\right), \tag{5.8}$$

the third term of Equation 5.6 scales with $1/t$ and can therefore be neglected for sufficiently large times. Therefore, m and n represent the slope and intersection of a linear dependency in the temperature-$\ln(t)$ space. From these parameters, the thermal conductivity and thermal diffusivity can easily be extracted as given by Equation 5.9:

$$\lambda = \frac{U_0 I}{4\pi L m}\,, \tag{5.9}$$

and by Equation 5.10:

$$a = \frac{D^2}{4\exp(3-\gamma)}\exp\left(\frac{n}{m}\right). \tag{5.10}$$

5.1.2. Applicability of the Linearized Model

Due to the approximations, a deviation from the original $f(\tau)$ occurs, which only vanishes for $\tau \geq 2$ [29]. The model is therefore applicable only for larger non-dimensional times.
Additionally, at the beginning of a measurement, much of the input power is first adsorbed by the THS itself, causing a strong initial increase in temperature due to the non vanishing heat capacity of the strip. Similarly, non-ideal thermal contact with the sample leads to an increase in temperature as well. This is especially important to consider for granular media, where the particles in direct contact with the strip exhibit a slightly altered packing configuration compared to those situated at greater distances within the sample. For particles small in comparison to the strip size, this effect should be small as well. The temperature curve of the THS will therefore only be linear at the point where the heat flow into the THS becomes insignificant and that into the sample stabilizes.
An upper boundary for the time is provided by the finite dimensions of the sample. The loss of heat at the sample's surface to the surrounding environment creates a deviation from the linear dependence leading to an upper boundary closely linked to the sample's size R_0 and its diffusivity. Equations 5.11 and 5.12 give the maximum time $t_{\max}$

$$t_{\max} \leq \frac{R_0^2}{2a} \tag{5.11}$$

and the maximum dimensionless time $\tau_{\max}$

$$\tau_{\max} \leq \frac{\sqrt{4at_{\max}}}{D} = \frac{\sqrt{2}R_0}{D}\,, \tag{5.12}$$

at which the surface reaches an excess temperature of 0.1 K, up to which the error is negligible.

Since the thermal diffusivity of the sample is unknown before a measurement, it is advantageous to collect more data than needed and select all values $t < t_{\max}$ in the later evaluation to determine the thermal properties.
Furthermore, heavy electrical leads may act as heat sources or sinks, which will create a deviation from the linear model. This deviation can be minimized experimentally by ensuring good electrical connections.
Another requirement for this method is the contact with the material surrounding the strip. If the contact is poor, the heat in the THS may not be emitted efficiently. If this is the case, the initial time taken for the heat flow to stabilize and therefore the temperature to become linear will be significantly larger and in extreme cases could prevent a heating curve from being analyzed correctly.

5.1.3. Model Uncertainty

In addition to several non-linear model errors, Hammerschmidt and Sabuga [29] introduced a new error due to the linear approximation. As only the linear part is evaluated here, non-linear model errors are not required which increases the accuracy in comparison to that of the non-linear method.

The linearized model error arises from the approximation of $f(\tau)$ and was numerically analyzed to yield Equations 5.13 and 5.14 with the constants L1 = 12.7, L2 = 0.85, A1 = 28.5 and A2 = 0.67:

$$\frac{u_{\mathrm{lin}}(\lambda)}{\lambda} \cdot 100 \approx \mathrm{L1} \cdot (\tau_{\min} \cdot \tau_{\max}^{\mathrm{L2}})^{-1}\,, \tag{5.13}$$

$$\frac{u_{\mathrm{lin}}(a)}{a} \cdot 100 \approx \mathrm{A1} \cdot (\tau_{\min} \cdot \tau_{\max}^{\mathrm{A2}})^{-1}\,. \tag{5.14}$$

In addition to these model errors, additional evaluation and measurement errors have to be accounted for as explained in Section 5.3.

5.2. Measurement and Evaluation

In the experiments conducted here, the THS is employed continuously to monitor the temperature within the sample. By applying Ohm's law:

$$R = \frac{U}{I}\,, \tag{5.15}$$

the measured voltage U and current I can be translated into the THS resistance R. With the THS temperature calibration function:

$$R(T) = R_0\Big(A \cdot T + B \cdot T^2 + C \cdot (T - 100) \cdot T^3\Big)\,, \tag{5.16}$$

the resistance may be converted into the THS temperature. For the measurements, a constant power is set that corresponds to the model's $U_0 I$. When using the default low-power mode with a power of 0.02 W, the sample's temperature does not change significantly, which is ideal for long-term observations. However, for a measurement, a temperature change of a few Kelvin is required. Depending on the sample properties, the high-power mode with 1 W to 5 W leads to an initially drastic increase in temperature that flattens over time as shown in Figure 5.1. The linearized model given in Section 5.1 is then used to evaluate this measurement.
For many measurements, it is advantageous not to wait for the temperature of the sample to reach a stationary state but to measure with an underlying temperature gradient. If the sample's temperature is not stationary, the temperature change has to be corrected before applying the model since only the influence of the THS is of interest.
This is done by fitting the temperature data before and, with a sufficiently long gap, after a measurement. The gap is required due to the decreasing influence of the temperature change from a measurement. For the regression, the data is fitted using either a linear function, a fifth-order polynomial function or or a Newton function:

$$T(t) = a + b \cdot t\,, \tag{5.17}$$

$$T(t) = a + b \cdot t + c \cdot t^2 + d \cdot t^3 + e \cdot t^4 + f \cdot t^5\,, \tag{5.18}$$

$$T(t) = T_{\mathrm{eq}} + (T_{\mathrm{i}} - T_{\mathrm{eq}}) \cdot (1 - \exp(-h \cdot t))\,. \tag{5.19}$$

Notably, these fits are not necessarily intended to resemble the physical characteristics of the temperature change. Instead, they are simply used to accurately match the original temperature values. An example correction using a fifth-order polynomial fit is shown in Figure 5.2.

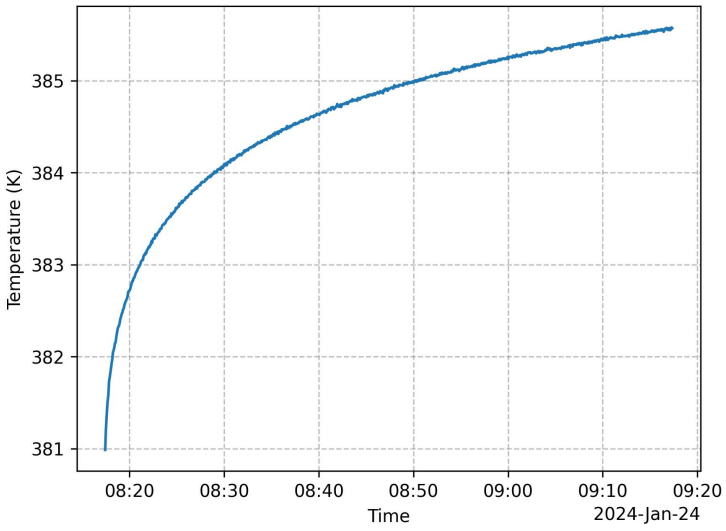

Figure 5.1.: Example curve of the THS temperature over time during a measurement. A strong increase in the initial temperature is visible in the first few minutes that flattens over time.

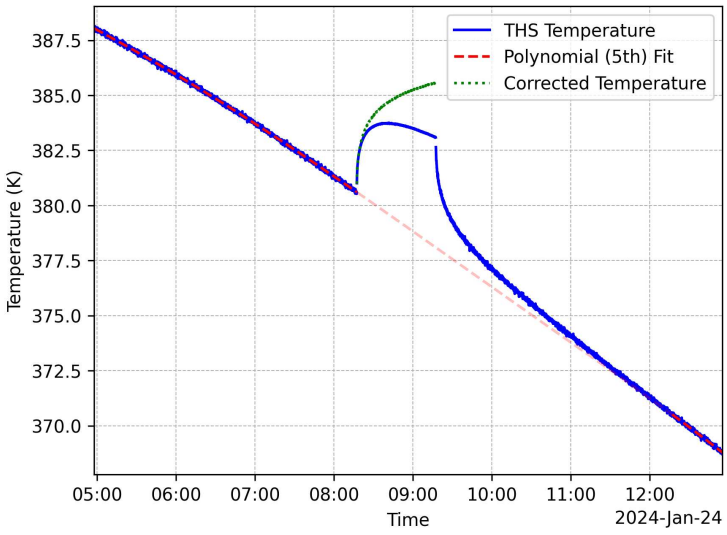

Figure 5.2.: Temperature correction of a non-stationary THS measurement. A fifth-order polynomial is used to subtract the sample temperature gradient from the measurement. The dark red dashed line resembles the fitted region while the lighter red one represents the interpolated values used to correct the data.

This correction is only possible if the temperature gradient of the sample is sufficiently smooth. Short-term or larger amplitude temperature fluctuations may prevent the data from being fitted which could render any non-stationary measurement non-evaluable. For this reason, a stable background temperature control system is of great importance.

To apply the model, the data is plotted as a temperature difference from the initial value on a logarithmically scaled time axis to reveal the linear part. This part is then fitted as shown in Figure 5.3. From the fit, the thermal conductivity and thermal diffusivity are calculated using the slope and intercept. Additionally, the nondimensional time limits τ_{min} and τ_{max} are determined from the thermal diffusivity. If these limits exceed the boundaries of $\tau_{\mathrm{minlim}} = 2$ and τ_{maxlim}, the fit is altered in position until the limits match. The resulting thermal properties may then be used as a final result. In the case that the limits can not be matched, the measurement is not usable for evaluation.
For some of the granular media analyzed in this work, the upper boundary is not important since the discrepancy from the linear portion occurs well beyond the duration of the measurement. This is due to an extremely low thermal diffusivity and a relatively large sample size. For materials with larger thermal diffusivity, such as ice, the upper boundary will result in a deviation from the linear behavior at an earlier point in time. Depending on the duration of the measurement, this boundary has to be identified in order to precisely fit the linear part as described in Section 6.2.7.

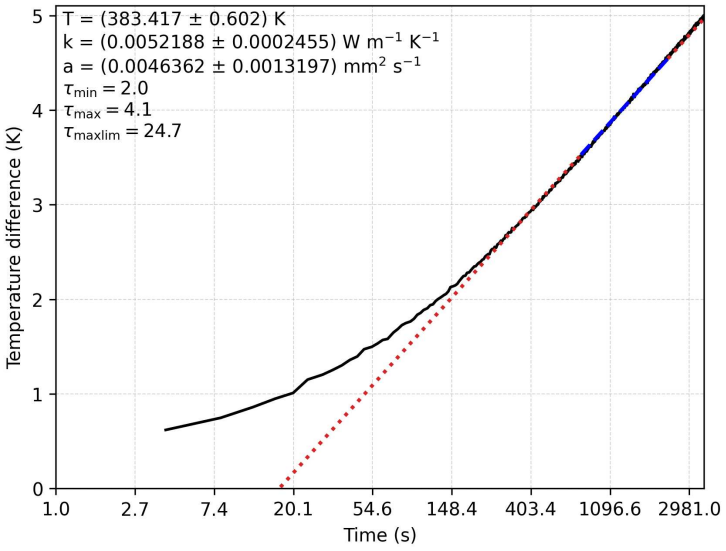

Figure 5.3.: Evaluation of a logarithmically plotted THS temperature curve with an initial non-linear behavior, followed by a linear part. The parameters and position of the linear fit are used to calculate the properties listed in the top left corner.

5.3. Uncertainty Assessment

In addition to the linear model error described in Section 5.1.3 the measurement and it's evaluation are subject to several other uncertainties, which are discussed in this section.

5.3.1. Measurement Errors

In the laboratory experiments, the measurement of the current and voltage is susceptible to error. Since neither the current nor the voltage are constant during a measurement due to fluctuations in the power source as well as due to the temperature change of the THS, average values with standard deviations ΔU_{std} and ΔI_{std} are used to calculate the mean power $P = U \cdot I$ of a measurement. With the uncertainty of the digital multimeter readout $\Delta U_{\text{mult}} = 0.000\,05\,\text{V}$, the total voltage error is $\Delta U = \sqrt{\Delta U_{\text{std}}^2 + \Delta U_{\text{mult}}^2}$.
Since the current is not measured directly, the uncertainties due to the shunt resistance and shunt voltage have to be considered and added to the standard deviation to provide the total uncertainty of the measurement current $\Delta I = \sqrt{\Delta I_{\text{std}}^2 + \Delta I_{\text{shunt}}^2}$:

$$\Delta I_{\text{shunt}} = \sqrt{\left(\frac{1}{R_{\text{shunt}}}\Delta U_{\text{shunt}}\right)^2 + \left(\frac{U_{\text{shunt}}}{R_{\text{shunt}}^2}\Delta R_{\text{shunt}}\right)^2}. \tag{5.20}$$

The uncertainty of the shunt resistance ΔR_{shunt} was determined through a direct resistance measurement with a digital multimeter before the shunt resistance was included in the setup. The mean resistance with standard deviation and multimeter uncertainty was found to be $R_{\text{shunt}} = (47.1291 \pm 0.0006)\,\Omega$ at constant ambient temperature. The shunt voltage error $\Delta U_{\text{shunt}} = 0.0005\,\text{V}$ takes into account not only the uncertainty of the multimeter but also small variations due to typical ambient temperature changes at the location of the shunt resistance, which are not included in ΔR_{shunt}.

5.3.2. Evaluation Errors

In the process of fitting data, noise and predefined uncertainties of the temperature reading will result in an uncertainty in the fit parameters. The slope error Δm and the intercept error Δn are therefore important to consider when evaluating the uncertainty of the thermal conductivity and thermal diffusivity.
The predefined uncertainty of the temperature data ΔT comes from several different sources. Firstly, there is uncertainty in determining the temperature from the error-prone THS resistance via Equation 5.16. Secondly, small temperature changes in the sample or the electrical leads cause the voltage signal and therefore the THS temperature to fluctuate, creating noise.
Additionally, if the temperature of the measurement was corrected, the uncertainty of the correction fit has to be accounted for. This error becomes significant for very noisy data and is therefore added to the uncertainty of the temperature data ΔT to be accounted for in the linear fit and passed onto the fit parameter errors.

5.3.3. Combined Uncertainty

Combining the above-mentioned linearized model error, the measurement uncertainty and the evaluation uncertainty, the total error of the thermal conductivity and thermal diffusivity can be expressed in the form of Equations 5.21 and 5.22:

$$\Delta\lambda = \sqrt{u_{\text{lin}}^2(\lambda) + \left(\frac{1}{4\pi L m}\right)^2 \left[(\Delta U \cdot I)^2 + (\Delta I \cdot U)^2 + \left(\Delta m \frac{U \cdot I}{m}\right)^2\right]}, \tag{5.21}$$

$$\Delta a = \sqrt{u_{\text{lin}}^2(a) + \left(\frac{D^2}{4\exp(3-\gamma)}\right)^2 \left[\left(\Delta n \frac{\exp(\frac{n}{m})}{m}\right)^2 + \left(\Delta m \frac{n\exp(\frac{n}{m})}{m^2}\right)^2\right]}. \tag{5.22}$$

6. Experiments and Results

The experiments conducted in this study were performed on multiple samples of dry and icy regolith simulants. Unless otherwise indicated, each simulant was prepared following the procedures described in Chapter 3 and measured in the TVAC under low pressures of $<10^{-4}$ mbar. In this chapter, the experiments and the results are presented and subsequently analyzed. The results of the dry lunar regolith simulants are presented in Section 6.1, while Section 6.2 contains the results of the icy simulants.

6.1. Dry Lunar Regolith Simulants

For the dry lunar regolith simulants, measurements were performed on two LHS-1 samples (LHS-1 S1 and S2) and on one sample of the Lunex Technologies simulant (Lunex S1). Another sample presented here consists of the remains of a dried-out icy LHS-1 sample (Icy LHS-1 S1 dried), which was mixed with micro-granular water ice as described in Section 6.2 and dried in the TVAC.
The following Section 6.1.1 describes the properties of the dry samples and the conditions and setup utilized for the measurements, while the resulting thermal conductivity values are presented and analyzed in Section 6.1.2. Here, a comparison to Apollo samples is made and the GBB model for the thermal conductivity is applied. Section 6.1.3 presents the thermal diffusivity values and the derived specific heat capacity.

6.1.1. Sample Properties and Experimental Procedure

For the initial sample LHS-1 S1, the entire volume of the sample holder was utilized as described in Section 4.1.1, leading to a considerable sample mass of (1301 ± 10) g. With known material density and measurement of the height of the sample, a bulk density of $(1.580 \pm 0.320)\,\mathrm{g\,cm^{-3}}$ was derived. Due to the large surface area of the sample, it could not be flattened evenly, resulting in a large standard deviation in the height measurement, which is reflected in the uncertainty of the bulk density. The same sample was subsequently compacted to yield sample LHS-1 S1 compacted with a bulk density of $(1.720 \pm 0.300)\,\mathrm{g\,cm^{-3}}$.

For LHS-1 S1, measurements were performed exclusively during stationary states, starting at low temperatures. This non-optimized setup led to an elongated experimental time frame, which is why the chamber was flooded with Argon in between measurements to accelerate the temperature adjustment period between stationary states. For the measurements, the chamber was then slowly pumped down again. It is anticipated that the sample packing structure was modified during the flooding and pump-down cycles, resulting in an increase in bulk density and volume filling fraction over time. Additional vibrations of the setup due to the pumps could have resulted in a similar effect. However, an attempt to measure a difference in bulk density by comparing the height before and after the entire measurement run did not result in any significant change relative to the uncertainty of the height measurement.

The analysis of the entire temperature range of 175 K to 450 K for this non-compacted sample was conducted over a period of approximately one month. As a result, the aluminum tray method was employed for all remaining samples.

With this tray method, the uncertainties in the height measurement and the mass measurement are reduced as described in Section 4.1.1. The mass uncertainty, due to both the balance's inaccuracy and any material stuck to the caliper utilized for height measurement or the spoon used for flattening, is estimated to be 1 g. With a smaller standard deviation of the height measurements, this results in relatively smaller uncertainties for the bulk densities and volume filling fractions of the other samples. All of the sample properties are listed in Table 6.1.
In order to further reduce the experimental timeframe, the thermal gradient correction, as presented in Section 5.2, was additionally implemented for the aluminium tray samples. This enabled the conduction of measurements not only during stationary states but also in the intermediate periods, making the flooding with Argon obsolete. To compare both methods, sample LHS-1 S2 was prepared in a similar way to LHS-1 S1, although within the aluminium tray.
The last sample, Icy LHS-1 S1 dried, was prepared differently, as it consists of the dried remains of an icy sample. The height and mass of this sample were measured only after the experiments were completed, since the structure of the dried material was not to be changed before the measurements. These measurements were performed by first heating and then cooling the sample, allowing insight into the entire temperature range.

Table 6.1.: Sample properties of the dry lunar regolith simulants

Sample	Mass (g)	Bulk density ($\mathrm{g\,cm^{-3}}$)	Volume fraction
LHS-1 S1	1301 ± 10	1.580 ± 0.320	0.49 ± 0.10
LHS-1 S1 compacted	1301 ± 10	1.720 ± 0.300	0.53 ± 0.09
LHS-1 S2	507.4 ± 1.0	1.600 ± 0.120	0.49 ± 0.04
LHS-1 S2 compacted	507.4 ± 1.0	1.700 ± 0.080	0.53 ± 0.07
Icy LHS-1 S1 dried	412.1 ± 1.0	1.450 ± 0.100	0.45 ± 0.03
Lunex S1	397.7 ± 1.0	1.380 ± 0.800	0.43 ± 0.03

6.1.2. Thermal Conductivity

The thermal conductivity was derived for all of the conducted measurements as explained in Section 5.2. While the temperature curves of each of those measurements can be found in the supplementary material in Appendix A.2, this section presents the results, a comparison to Apollo samples, and an interpretation using the Gundlach Blum Bürger model.

Non compacted LHS-1

Figure 6.1 depicts the measured thermal conductivity of LHS-1 S1 in the temperature range of 175 K to 450 K. The data was fitted with Watson's equation

$$a + b \cdot T^3 \,, \tag{6.1}$$

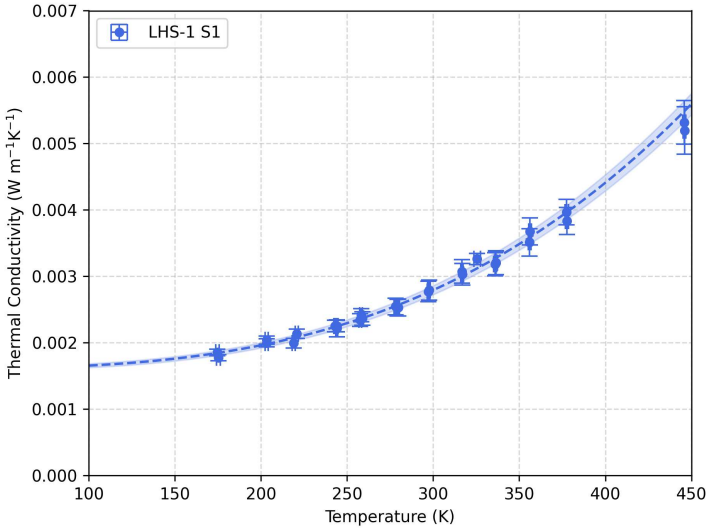

Figure 6.1.: Thermal conductivity of LHS-1 S1 with a bulk density of $(1.580 \pm 0.320)\,\mathrm{g\,cm^{-3}}$ in the temperature range of 175 K to 450 K. The dashed line shows a $a + b \cdot T^3$ fit with an uncertainty of one standard deviation of the fit parameters, closely matching the measured values with $R^2 = 0.99$.

where a represents a constant contact conductivity not dependent on temperature and $b \cdot T^3$ represents the radiative one. Due to the low-pressure environment of the TVAC, any gas conductivity is assumed to be negligible. The parameter values of the shown regression are listed together with a one-sigma uncertainty in Table 6.2. The same uncertainty is displayed in the plot as an uncertainty band around the fit. With a coefficient of determination of $R^2 = 0.99$, this data is very well fitted.

LHS-1 at different bulk densities

Figure 6.2 shows the plot of the compacted variant of LHS-1 S1 in addition to sample Icy LHS-1 S1 dried.

It can be seen that as the bulk density increases, the value of a increases while that of b decreases. This can be attributed to the alteration of the packing structure of the granular material. When compacting such a sample, the space between grains reduces, increasing the number and possibly the size of contact points between grains, resulting in a larger contact conductivity a. At the same time, the radiative conductivity $b \cdot T^3$ is reduced due to the reduction in the mean free path of photons responsible for the transfer of heat. The smaller the pore space gets, the less heat can be transported via radiation.

This behavior can be observed for the low bulk density sample Icy LHS-1 S1 dried, where the total thermal conductivity surpasses the one of the non-compacted LHS-1 S1 after approximately 350 K due to the larger contribution of the radiative conductivity with a larger pore space.

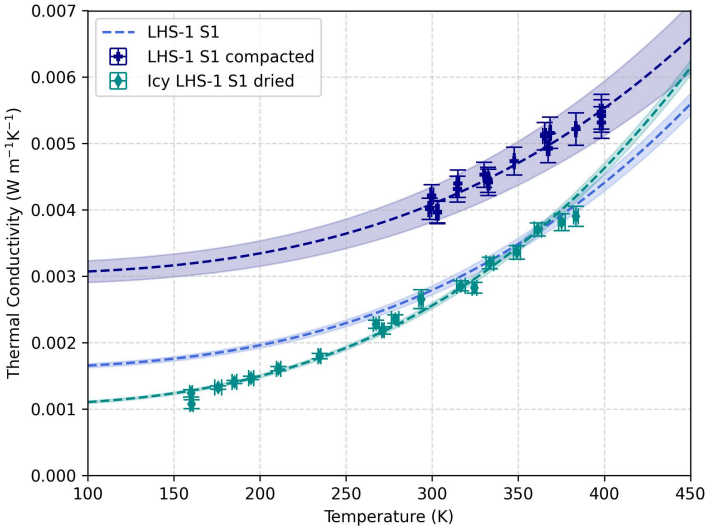

Figure 6.2.: Thermal conductivity of LHS-1 samples with $a + b \cdot T^3$ fits at higher (LHS-1 S1 compacted) and lower (Icy LHS-1 S1 dried) bulk density in comparison to LHS-1 S1. The coefficients of determination are $R^2 = 0.95$ for LHS-1 S1 compacted and $R^2 = 0.98$ for Icy LHS-1 S1 dried.

Reproducibility

To verify the results obtained from the first LHS-1 S1 sample and to test the comparability between the two insertion methods as well as to analyze the influence of the argon flooding, sample LHS-1 S2 was analyzed, yielding the results presented in Figure 6.3.
The measured values for LHS-1 S2 are in good agreement with the previously collected data for LHS-1 S1, despite the simplicity of the method of filling and compacting the sample with only the use of a spoon.
This is also shown by the bulk densities and volume filling fractions given in Table 6.1, which are in good agreement to those of S1 in both the compacted and non-compacted variants.
Due to the flooding with Argon for LHS-1 S1, the later measured values at higher temperatures might be slightly larger due to the expected compaction with each flooding cycle, which could have led to a slight increase in the conductive heat transfer. This might have contributed to a slight difference in the fits for larger temperatures.
A comparison of the $a + b \cdot T^3$ fit parameters listed in Table 6.2 gives a similar result, as small variations from the parameters of sample S1 are present. However, the deviations could also result from the smaller temperature range fitted for sample LHS-1 S2. This means that the extrapolation of the fit to smaller and larger temperatures might not reflect the exact behavior of the sample's thermal conductivity. A larger uncertainty is also visible in the fit parameter errors and the R^2 values of the non-compacted sample $R^2 = 0.98$, which is slightly lower than the one for LHS-1 S1. The compacted LHS-1 S2 fit has a coefficient of determination of $R^2 = 0.95$, the same as the compacted LHS-1 S1, which is reasonable since the data is scattered similarly in the same temperature range.

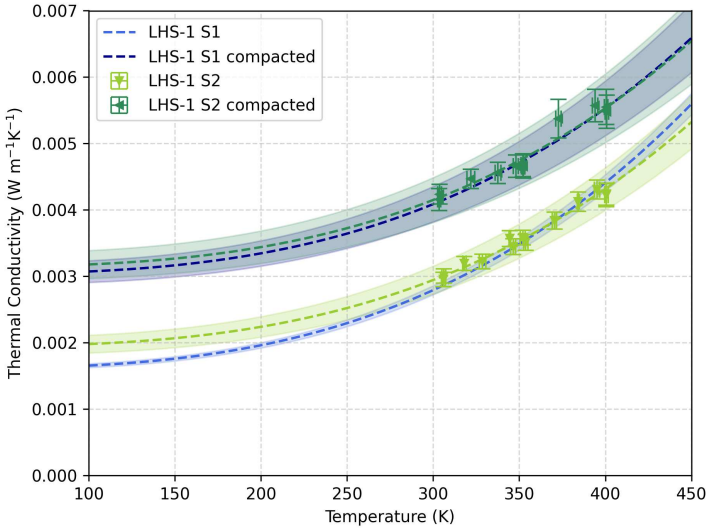

Figure 6.3.: Thermal conductivity of LHS-1 S1 in comparison to a second sample S2 in two configurations with similar bulk densities. The results are in good agreement with the first sample, although small variations are evident, possibly due to small differences in density. The coefficients or determination of the $a + b \cdot T^3$ fits are $R^2 = 0.95$ for the compacted sample S2 and $R^2 = 0.98$ for the non-compacted one.

Difference between the simulants

Figure 6.4 shows a comparison between the measured thermal conductivities of LHS-1 S1 and Lunex S1. The resulting $a + b \cdot T^3$ fit of Lunex S1 has a coefficient of determination of $R^2 = 0.96$. This value indicates that the model resembles the general trend of the data, although with fluctuations.

Notably, the thermal conductivity of this simulant is generally larger than that of LHS-1 S1, while the volume filling fraction is lower. The discrepancy is attributable to variations in the particle size distribution and minor discrepancies in the chemical composition, which can alter the mean-free path of the photons, as well as the solid conductivity.

Table 6.2.: Watson's equation fit parameters of the dry regolith simulants thermal conductivities.

Sample	a ($10^{-3}\,\mathrm{W\,m^{-1}\,K^{-1}}$)	b ($10^{-11}\,\mathrm{W\,m^{-1}\,K^{-2}}$)
LHS-1 S1	1.61 ± 0.03	4.37 ± 0.15
LHS-1 S1 compacted	3.03 ± 0.16	3.90 ± 0.40
LHS-1 S2	1.94 ± 0.13	3.71 ± 0.30
LHS-1 S2 compacted	3.14 ± 0.21	3.74 ± 0.49
Icy LHS-1 dried	1.05 ± 0.02	5.59 ± 0.11
Lunex S1	2.41 ± 0.02	4.90 ± 0.09

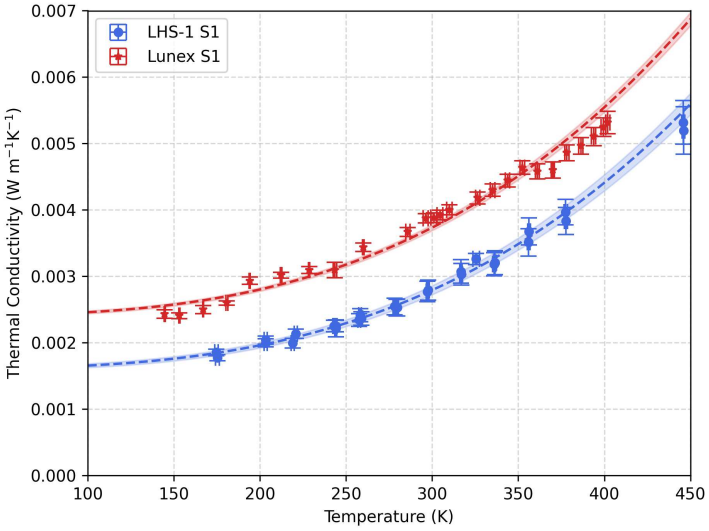

Figure 6.4.: Thermal conductivity of Lunex S1 in comparison to LHS-1 S1.

Comparison to the Apollo Samples

To evaluate weather the simulants thermal conductivity resembles that of the lunar material, the here-found results are compared with thermal conductivities of Apollo samples, as provided by Cremers [30, 31, 32, 33, 34]. Figures 6.5 and 6.6 show this comparison for highlands/boundary samples and maria samples respectively. The thermal conductivity of a basalt sample as analyzed by Fountain and West [35] is depicted as well. It is similar in composition to the regolith simulants. The exact chemical constituents of the basalt as well as the simulants can be found in Table A.3. The Apollo sample's $a + b \cdot T^3$ fits are based mostly on data in the temperature range of 100 K to 400 K and extrapolated to the entire temperature range.

Although all thermal conductivity values are within the same order of magnitude, there are notable differences between the materials. Most significantly, several Apollo samples exhibit smaller thermal conductivities than the presented simulants, especially in the radiative term.
This is possibly a result of the small particle sizes, given that these samples consisted of mostly fine dust particles with grain sizes of, for example, 20 µm and <50 µm for Apollo 11 and 16 respectively. This reduces the void space between the grains, leading to a smaller radiative conductivity. At the same time, the reduced particle size should lead to an increased solid conductivity as more contact points emerge. While the solid conductivity of the Apollo 11 sample is indeed larger than that of the Apollo 16 one, the radiative conductivity is larger for Apollo 11 as well. Given these discrepancies, it is plausible that additional factors are involved, such as variations in particle morphology or alterations in composition between the Apollo samples themselves, as well as the simulants.
In conjunction with differences in the particle size, this could also explain the differences in the bulk density. For example, the thermal conductivities of the Apollo 11 and Apollo 12 samples at a bulk density of 1.64 g cm^{-3} drastically differ. A difference in the material composition is therefore plausible, as the samples were sourced from different locations on the lunar surface. For the two

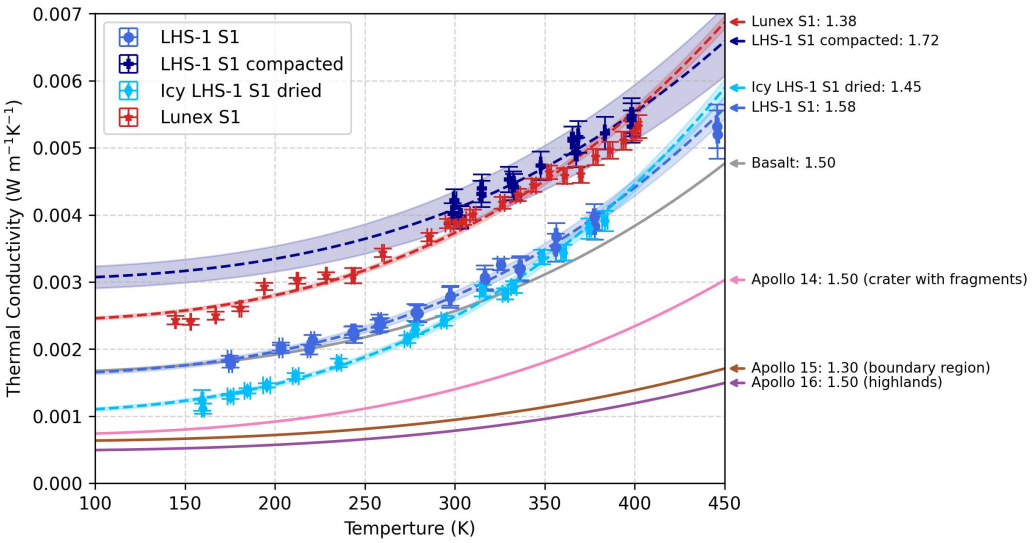

Figure 6.5.: Comparison of the thermal conductivities found in this work to those of Apollo highlands and boundary region samples. The annotations on the right-hand side provide information on the density of the samples in $\mathrm{g\,cm^{-3}}$ as well as the location where they were sampled. The basalt data is taken from Fountain and West [35].

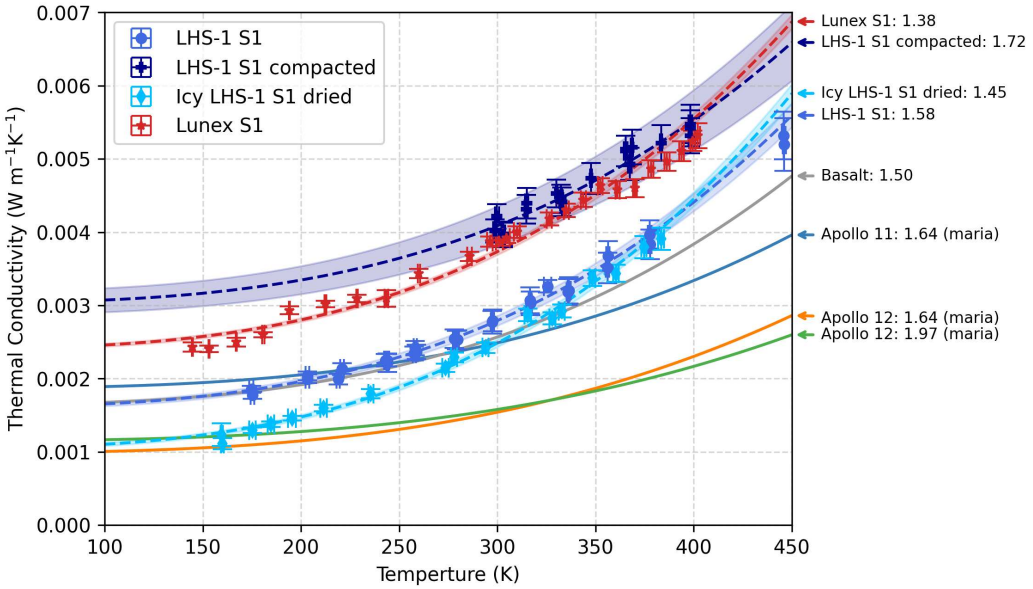

Figure 6.6.: Comparison of the thermal conductivities found in this work to those of Apollo maria samples. The density of the samples in $\mathrm{g\,cm^{-3}}$, as well as the location where they were sampled, is given on the right-hand side of the figure. The basalt data is taken from Fountain and West [35].

Apollo 12 samples, which consist of the same material, a similar behavior as for LHS-1 S1 and Icy LHS-1 S1 dried is evident, where the radiative conductivity outweighs the solid one due to the larger mean free path of the photons at a smaller bulk density and for elevated temperatures.

The basalt sample matches the LHS-1 samples most closely, as the composition is very similar. Some deviations in the particle size, as well as the shape could potentially lead to the observable differences.

In general, it can be concluded that for irregular granular samples like those analyzed here, the exact composition as well as morphology of the particles can influence the resulting thermal conductivity significantly. Although the simulants aim to resemble the lunar material in composition, as well as morphology, the space-weathered appearance is not recreated perfectly. Differences in the sample location on the lunar surface are also evident, where the chemical composition and particle morphologies vary.
This is particularly evident when comparing the LHS-1, Lunex, and the basalt sample, where SiO_2 is the most abundant component but differences in the other substance abundances are present. This alters the effective solid thermal conductivity, thereby influencing the trend of the curves.

Additionally, differences in the packing structure of the sample might influence the contact conductivity in a significant way. The measurement setup alone induces such differences. For the Apollo samples, only a few grams of material were used, while the samples analyzed here consisted of multiple hundred grams of regolith simulant. The shape of the container, the filling method, and the contact to the THS change the size and the number of contact points between the grains, altering the contact conductivity.

In conclusion, the thermal conductivities of the lunar regolith simulants are of the same order of magnitude as those of the Apollo samples. Discrepancies between the Apollo samples, but also between the simulants and the Apollo samples are caused by variations in the particle sizes, material compositions and morphologies. Nevertheless, the regolith simulants provide a good estimate on the lunar materials thermal conductivity and resemble the general temperature trend.

Analysis with the Gundlach Blum Bürger Model

In order to analyze the measured thermal conductivities of the dry regolith simulants in more detail, the Gundlach Blum Bürger model is applied as described in Section 2.2.1. In comparison to Watson's equation, this model provides more insight into the physical nature of the radiative and the contact conductivity. Additionally, the solid conductivity is assumed to be temperature-dependent in this model. Fits for Dry LHS-1 and its compacted variant are shown in Figure 6.7. For the measured data range, there is no significant difference to the $a + bT^3$ fit. A pronounced deviation would only be evident for temperatures below 100 K, which was not achievable with the experimental setup utilized in this work. The other data sets from this work were also fitted with the model, as illustrated in Figure 6.8.

For the model, the effective particle size r and the scaling parameter χ were employed as free parameters. The volume filling fraction ϕ was utilized from Table 6.1 as a fixed value for each

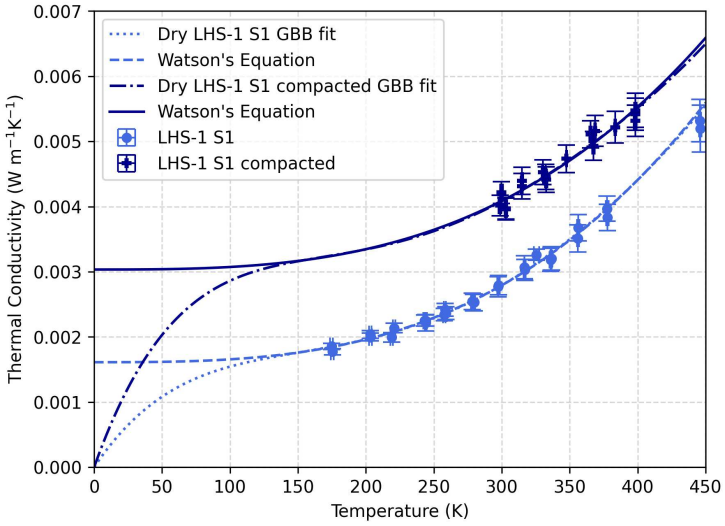

Figure 6.7.: Dry LHS-1 S1 fit with Watson's equation and the Gundlach Blum Bürger model. Both models fit the data with high certainty, reflected in $R^2 = 0.99$ for LHS-1 S1 and $R^2 = 0.95$ for the compacted variant for both models.

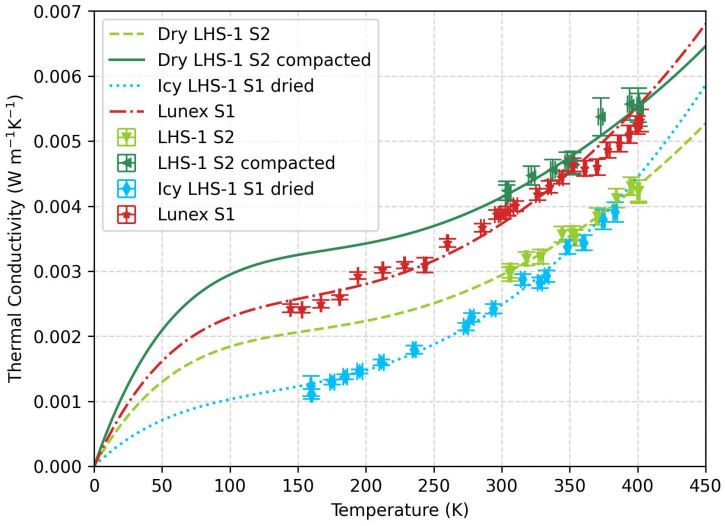

Figure 6.8.: Gundlach Blum Bürger fits for the remaining dry regolith simulant samples, closely resembling the measured data with $R^2 = 0.95$ for Dry LHS-1 S2 compacted, $R^2 = 0.96$ for Lunex S1, $R^2 = 0.98$ for Dry LHS-1 S2 and $R^2 = 0.99$ for Icy LHS-1 S1 dried.

sample without any uncertainty to reduce the number of fit parameters. A list of these parameters can be found in Table 6.3. The other parameters of the model were adapted from Bürger et al. [11] for lunar regolith as detailed in Section 2.2.1.

Table 6.3.: Best fit parameters of the Gundlach Blum Bürger model for the dry samples. The particle size r and the scaling parameter χ were utilized as free parameters, while the volume filling fraction ϕ was fixed at the measured value.

Sample	r (µm)	ϕ	χ
LHS-1 S1	65	0.49	0.81
LHS-1 S1 compacted	59	0.53	1.20
LHS-1 S2	53	0.49	0.91
LHS-1 S2 compacted	56	0.53	1.22
Icy LHS-1 dried	71	0.45	0.68
Lunex S1	55	0.43	1.58

The average fitted effective particle size of LHS-1 with standard uncertainty is (60.9 ± 6.6) µm, which is in in very good agreement with the median particle size of 61 µm. For Lunex S1, the effective particle size was fitted to be 55.0 µm, which is only slightly smaller than the median of 61 µm. These results indicate that the median particle size is a good approximation for the effective particle size in the heat transfer model for this application. In contrast to the mean particle size, which is substantially larger, the median also accounts for the large number of small particles in the samples, which fill parts of the pore spaces between the larger particles, altering the solid conductivity through new and differently sized contact points and the radiative conductivity by influencing the mean free path of the photons.
The fitted χ values of the dry regolith simulants are in general larger than the value of $\chi = 0.69$ found by Bürger et al. [11] for the maria and high thermal conductivity highlands model, as well as $\chi = 0.14$ for the low thermal conductivity highlands model. For LHS-1, χ increases with the volume filling fraction which indicates that the alteration in the packing structure also alters the behavior of the heat transfer. Since χ was introduced to describe any deviations from a monodisperse packing of spherical particles, additional effects play a role if the packing structure of such a highly irregular granular sample is changed, for example when particle edges realign under compression, altering the number and size of contact points.
In comparison to the χ values of the Apollo samples, the relatively large values found here could also be explained by deviations in the material parameters. The Poisson's ratio, the Young's modulus, the specific surface energy, and the infrared emissivity are not known for LHS-1 or the Lunex simulant. If the values differ from those of the Apollo samples, this deviation would be reflected in the fit by a variation in χ. A reduction in the Young's modulus, an increase in the Poisson ratio, or an increase in the specific surface energy would result in an elevated χ. It is not possible to determine all of these parameters from a singular fit, as multiple different parameter configurations could lead to the same result.

In general, the elevated χ values indicate that the high conductivity model with $\chi = 0.69$ might be more applicable to a highlands simulant than the low conductivity one with $\chi = 0.14$. The

previously found difference to the Apollo samples, which thermal conductivities were generally smaller than the ones found for the regolith simulants, also indicates the need for a larger scaling parameter, assuming the material properties are mostly consistent.
While the effective particle sizes matched closely with the median particle sizes of the simulants, deviations possibly occurred from the neglected uncertainty of the volume filling fraction. For future measurements, the precise determination of the volume filling fraction and a determination of the additional material properties of the simulants would be beneficial to derive the effective particle size and scaling parameter with more precision.

6.1.3. Thermal Diffusivity and Specific Heat Capacity

In addition to the thermal conductivity, the thermal diffusivity of the dry samples was measured as well. The results are shown in Figure 6.9 for Dry LHS-1 S1 and Icy LHS-1 S1 dried, and in Figure 6.10 for LHS-1 S2. For Dry LHS-1 S1 and Icy LHS-1 S1 dried, a slight downward trend with increasing temperature is visible, which results in a mostly constant diffusivity and a slight increase in the high-temperature regime. The values for the compacted sample are slightly larger in comparison to the uncompacted one, while the icy sample's thermal diffusivity is even larger. For LHS-1 S2, no significant difference is evident between the compacted and uncompacted samples, indicating there is no clear correlation between the volume filling fraction and the measured thermal diffusivity of these samples.
While the measured values are of a similar magnitude to those of the Apollo samples by Cremers [31], as shown in Figure 6.9, the strong fluctuations between the samples indicate an additional source of uncertainty, which is not reflected by the error bars in the plot. This uncertainty might be attributable to the minimal width of the THS, which is optimized for thermal conductivity measurements and not for thermal diffusivity measurements [29]. Therefore, the measured values

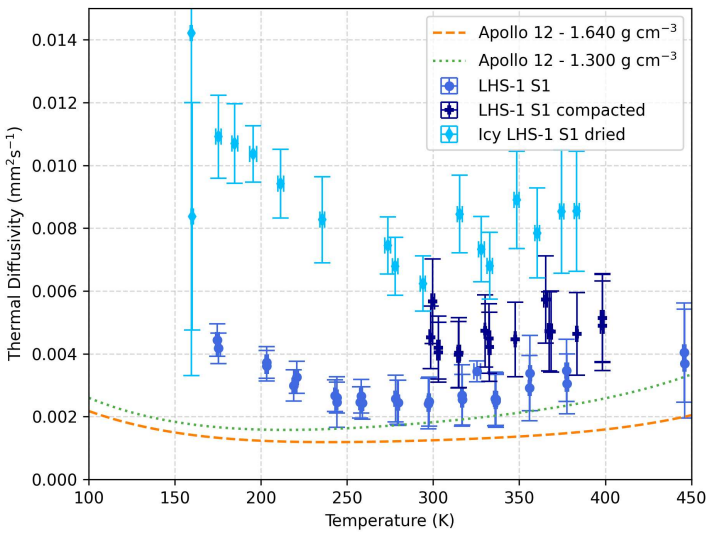

Figure 6.9.: Thermal diffusivity of Dry LHS-1 S1, S1 compacted and Icy LHS-1 S1. No clear trend with density can be seen from the data, which exhibits large fluctuations. The diffusivity initially decreases with increasing temperature and is mostly constant afterwards.

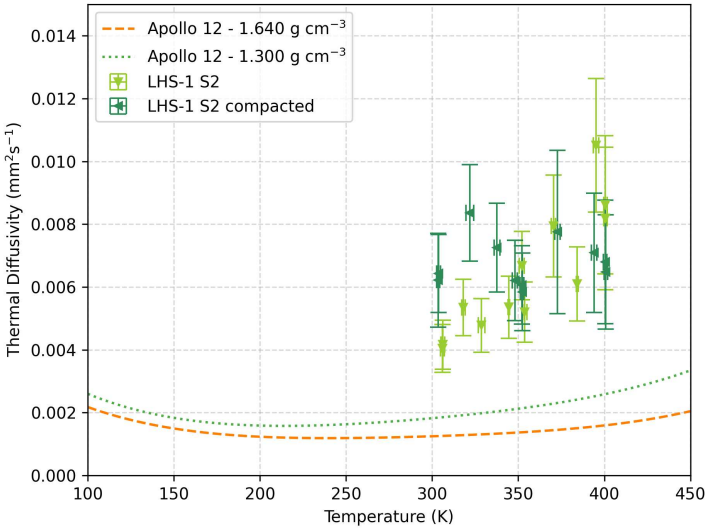

Figure 6.10.: Thermal diffusivity of Dry LHS-1 S2 and S2 compacted. The data range is similar to the compacted version of Dry LHS-1 S1, although more fluctuations are visible. No clear temperature trend is visible.

for the thermal diffusivity should be interpreted as order of magnitude only.
In comparison to literature, Austen and Shafirovich [36] also measured the thermal diffusivity of LHS-1, resulting in a similar initial temperature trend, although with values two orders of magnitude larger due to a significantly larger pressure of 10^{-2} mbar, where the gas component is not negligible.
From the thermal conductivity, the bulk density, and the thermal diffusivity, the specific heat capacity of the samples may be calculated via Equation 2.11. Due to the large uncertainty in the bulk density as well as the uncertainties in the measured thermal properties, these values are subjected to large uncertainties as well as shown in Figure 6.11.
The data is compared to the polynomial specific heat fit of Hayne et al. [18] for lunar regolith as provided by Equation 2.12. Figure 6.12 shows the same plot for the remaining dry samples. Given that the specific heat capacity is a material property, it should be consistent for all LHS-1 samples, regardless of volume filling fraction. However, this is not the case, suggesting that the unquantified uncertainty in the thermal diffusivity due to the THS width is the most probable cause of this deviation. It is therefore not possible to calculate the specific heat with sufficient certainty from the measured thermal properties of the samples utilized in this study.

Under the assumption that the specific heat capacity fit for lunar regolith is also applicable to the simulant, an estimation of the thermal diffusivity of the simulant is derived from the measured thermal conductivity and the specific heat fit. The results are shown in Figure 6.13 and 6.14 in comparison to the measured values.
A clear difference can be observed, with the derived curves following a similar trend as the above-shown Apollo sample's thermal diffusivities. The simulant's thermal diffusivity increases with increasing volume filling fraction, analogous to the previously found trend in thermal conductivity.

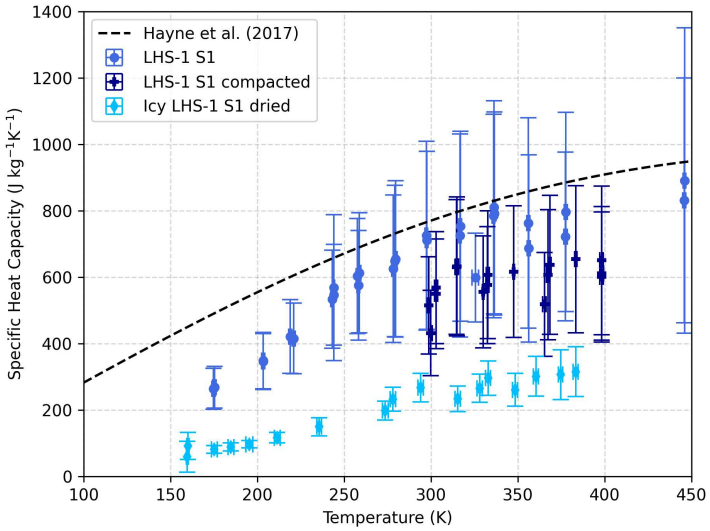

Figure 6.11.: Specific heat of Dry LHS-1 S1, S1 compacted and Icy LHS-1 S1 dried as derived from the thermal conductivity and diffusivity measurements. The data for the uncompacted dry sample matches the fit for lunar regolith closely for larger temperatures >250 K, while a deviation can be seen for lower temperatures. The other samples deviate strongly from the fit, most certainly due to the deviation in the thermal diffusivity.

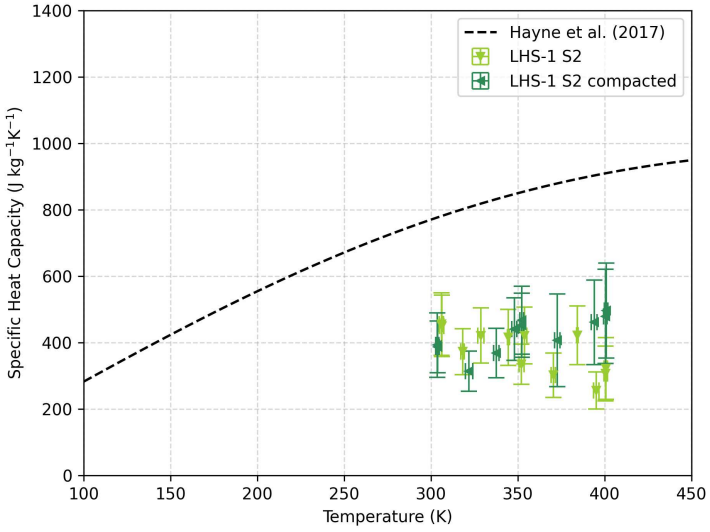

Figure 6.12.: Specific heat of Dry LHS-1 S2 and S2 compacted as derived from the thermal conductivity and diffusivity measurements. A strong deviation from the fit is visible for all samples, similar to Icy LHS-1 S1.

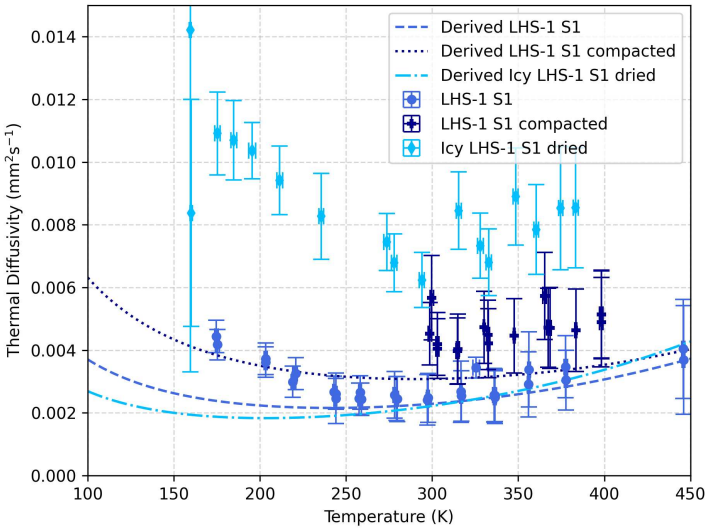

Figure 6.13.: Derived thermal diffusivity of Dry LHS-1 S1, S1 compacted and Icy LHS-1 S1 compared to the measured values.

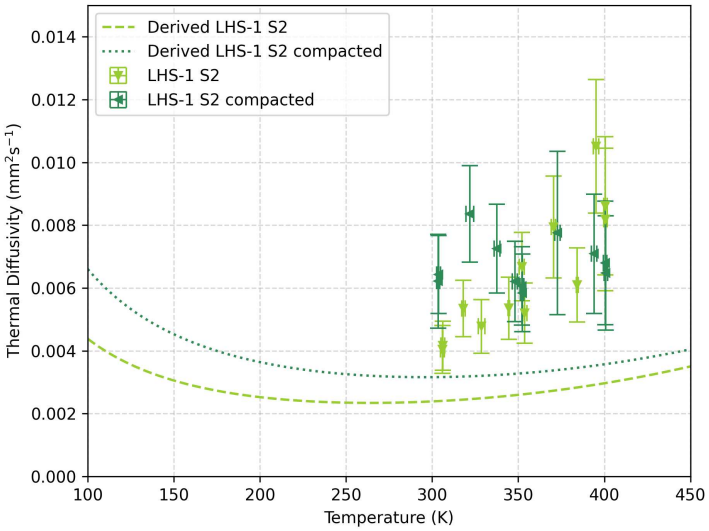

Figure 6.14.: Derived thermal diffusivity of Dry LHS-1 S2 and S2 compacted compared to the measured values.

6.2. Icy Lunar Regolith Simulants

In order to analyze the effect of ice added to a regolith simulant, a series of samples were prepared, and their thermal properties were investigated. Section 6.2.1 provides details on those samples and explains the procedure of the measurements. Sections 6.2.2, 6.2.3 and 6.2.4 outline the temperature and pressure conditions in the TVAC for these measurements and present the resulting thermal transport properties for three micro-granular icy samples, while Section 6.2.5 provides details for the mudpie sample and Section 6.2.6 for a pure ice sample respectively. After a clarification of the use of the linear THS model in Section 6.2.7, the thermal conductivity of these icy samples is finally analyzed in detail in Section 6.2.8.

6.2.1. Sample Properties and Experimental Procedure

Three samples, labeled Icy LHS-1 S1, S2, and S3, have been created with the micro-granular water ice approach as described in Section 3.4.3, while sample Mudpie LHS-1 S1 was created in the form of a mudpie as described in Section 3.5. This mudpie sample was frozen in the TVAC before the pump-down process started. The final sample Ice Particles S1 was prepared consisting of desiccated water ice particles only, without any added regolith simulant.
The sample properties and water ice contents of each of those samples are listed in Table 6.4. Here, the water ice content is given as relative weight. The volume filling fraction was calculated using the known material densities of the regolith and water ice respectively, along with the bulk density of the sample, which was determined in a manner analogous to that utilized for the dry samples.

Table 6.4.: Sample properties of the icy samples.

Sample	Mass (g)	Bulk density ($\mathrm{g\,cm^{-3}}$)	Volume fraction	Ice (wt %)
Icy LHS-1 S1	479 ± 1	1.520 ± 0.113	0.48 ± 0.04	2.24 ± 0.31
Icy LHS-1 S1 dried	412 ± 1	1.450 ± 0.101	0.45 ± 0.03	0.01 ± 0.01
Icy LHS-1 S2	441 ± 1	1.390 ± 0.119	0.44 ± 0.04	2.94 ± 0.11
Icy LHS-1 S2 cooldown	400 ± 1	1.450 ± 0.012	0.45 ± 0.01	1.56 ± 0.10
Icy LHS-1 S3	410 ± 1	1.150 ± 0.087	0.38 ± 0.03	7.71 ± 0.08
Mudpie LHS-1 S1	367 ± 1	1.080 ± 0.096	0.34 ± 0.03	2.90 ± 0.10
Mudpie LHS-1 S1 dried	356 ± 1	1.050 ± 0.093	0.32 ± 0.03	0.01 ± 0.01
Ice Particles S1	97 ± 1	0.290 ± 0.038	0.32 ± 0.06	100.00

Prior to the insertion of the sample, the sample holder was cooled to the greatest extent possible. As a result, the initial temperature of all experiments was primarily determined by the temperature of the sample holder, which was measured in the sample holder wall to be approximately 100 K. However, due to the lack of active cooling of the lid, the samples rapidly increased in temperature to approximately 150 K. For samples that were mixed with liquid nitrogen beforehand, exhibiting a much lower starting temperature, some measurements could be performed during the initial temperature rise.
The first sample Icy LHS-1 S1 was then exposed to a step-wise increase in temperature, which

did not provide a good temperature resolution and enabled much water to sublimate at once as described in Section 6.2.2. For the other samples, a constant temperature gradient approach was therefore implemented to create better temperature resolution and to avoid abrupt effects as explained in Section 4.3.2.
Samples Icy LHS-1 S1 and Mudpie LHS-1 S1 were subjected to elevated temperatures of up to 380 K to observe the drying process of these icy samples and to analyze how the material's thermal properties change during and after desiccation. Additionally, Icy LHS-1 S1 was cooled down again after desiccation to investigate the temperature dependence in comparison to the dry simulants that were not mixed with ice. Sample Icy LHS-1 S2 was cooled down again as well, but already after reaching approximately 210 K to observe the changes in the thermal properties due to a possible alteration in the ice structure as a result of sublimation and re-cementation processes.
The pressure within the TVAC was continuously monitored in order to register water vapor leaving the sample holder. The pumps were running the entire time, simulating the conditions on the lunar surface, where escaping vapor would also leave the system. Given that the sample holder only provides small openings for gas to escape and gas permeability through regolith is low due to the irregular porous structure [37], it has to be noted that the pressure reading does not accurately reflect the conditions within the sample holder and certainly not within the sample. Additionally, for sample Icy LHS-1 S2, these openings were frozen during the removal of the cold sample, possibly leading to even greater deviations.

6.2.2. Micro-Granular Icy LHS-1 S1

Starting with sample Icy LHS-1 S1, Figure 6.15 shows the temperature profile over time of not only the sample holder but also the THS during the entire experiment. The pressure reading is shown in the graph above. The observable discrepancy in temperature between the THS and the sample holder can be attributed to the fact that the sample holder temperature sensor is situated within the actively cooled wall, whereas the sample is exposed to the non-actively cooled lid directly from above. This results in a larger sample temperature, especially in the beginning due to the radiative heating of the lid by the TVAC outer walls. This effect is reduced for larger temperatures, where the sample gradually desiccates and is unable to conduct heat as efficiently. This insulates the THS in the center from the lid's temperature influence. Concurrently, the inner sample's temperature surpasses that of the lid, reversing the direction of the offset.
With temperature steps in the range of up to 20 K, a first change in pressure is observable after the sample holder reaches 200 K, which is shown in the closeup in Figure 6.16.
Here, sublimated water vapor escapes from the sample holder. This effect is even more pronounced after the step to 225 K, leading to an increasing TVAC pressure of up to 10^{-1} mbar. Over time, the increasing amount of water vapor that leaves the sample and sample holder at rising temperatures is removed by the pumps, desiccating the icy sample to a point, where the TVAC pressure shows no significant difference to the nominal values of 10^{-4} mbar to 10^{-5} mbar. Only small pressure increases are visible with each temperature step.
The pressure values fluctuate notably more in the low-temperature region. This is due to a non-optimal connection of the liquid nitrogen pipes within the TVAC, resulting in small quantities of gas leaving the cooling system. As the pipes are situated outside of the sample holder, the escap-

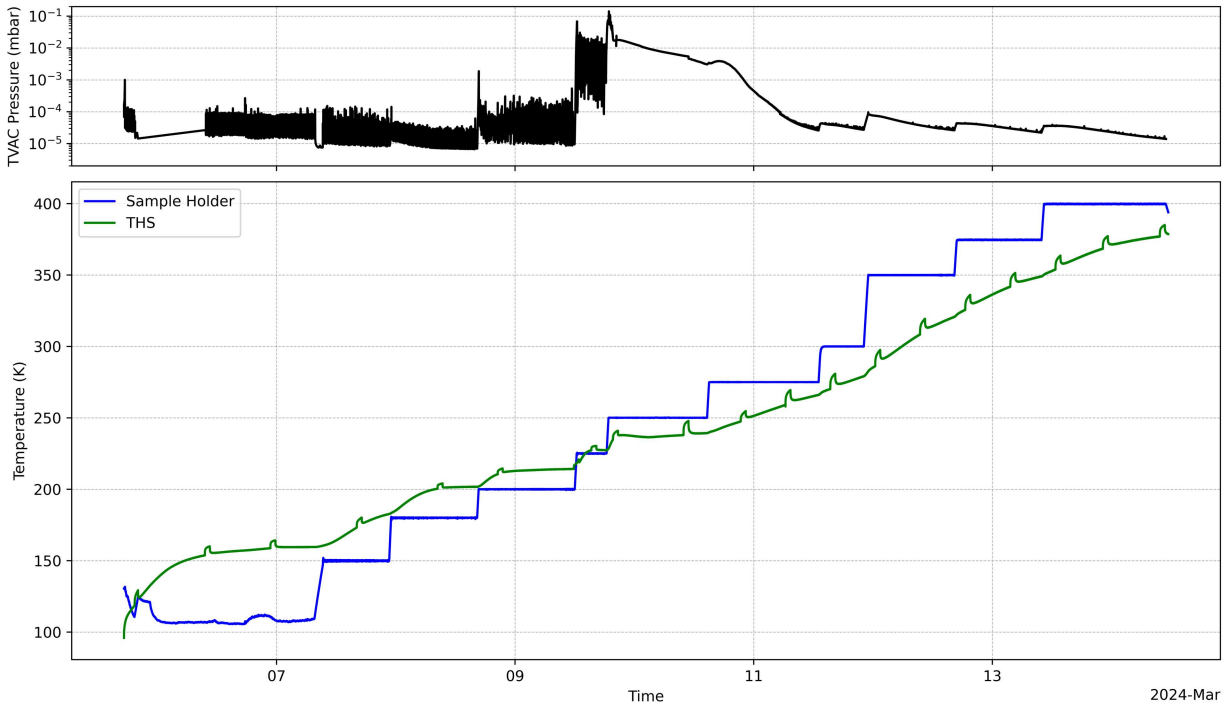

Figure 6.15.: Temperature and pressure profile of the Icy LHS-1 S1 measurements.

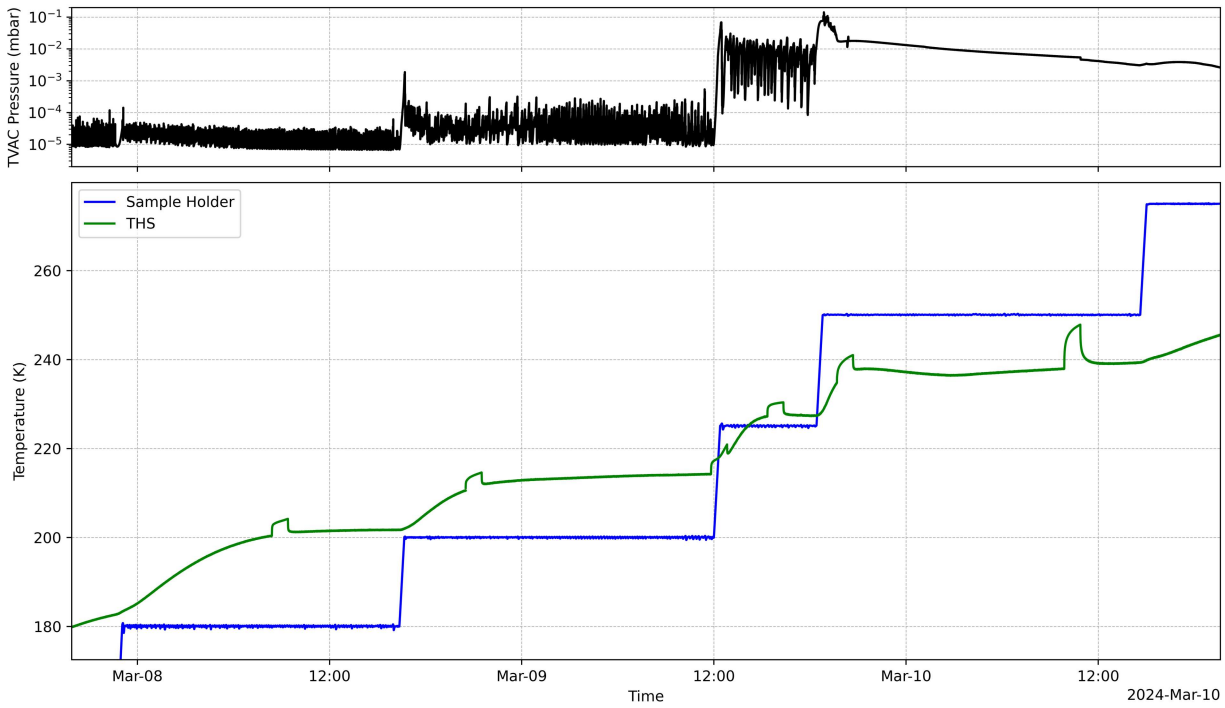

Figure 6.16.: Closeup of the temperature and pressure profiles of the Icy LHS-1 S1 measurements. After the sample holder's temperature step to 200 K, a spike in the TVAC pressure is visible, indicating sublimated water gas leaving the sample holder. After 225 K, this is even more pronounced.

ing gas is quickly removed by the pumps. It can be reasonably assumed that the sample material will not be significantly affected by this gas, given that the pressure remains below 10^{-4} mbar. At a temperature of 200 K, the sublimation pressure of water is $2 \cdot 10^{-3}$ mbar as shown in Figure 2.5. This means that water ice present in the sample sublimates at significant rates during the first time period shown in Figure 6.16, where the TVAC pressure shows no sign of escaping gas. Since the sample holder is still much colder, the gaseous water deposits at either a colder position in the sample or at the sample holder walls.
With an increase in the sample holder's temperature to 200 K, the re-deposited water ice sublimates as well, leading to a continuous escape of water vapor from the system. At even higher temperatures of 225 K and above, the out-gassing rate increases drastically since more and more ice sublimates. The TVAC pressure rises to values above 10^{-2} mbar, which is near the sublimation pressure of approximately $5 \cdot 10^{-2}$ mbar at this temperature. Here, the rate of gas pumping is insufficient to offset the rate of sublimation. This, in turn, constrains the sublimation rate, as no further ice sublimates when the pressure nears the sublimation pressure threshold. Ice therefore stays present in the sample over the time-span of multiple days of sublimation with a mostly constant outgassing rate. During this period, the pumping rate is only slightly smaller than the outgassing rate, resulting in a less fluctuating pressure reading in the TVAC for sample holder temperatures exceeding 250 K.

Thermal Conductivity of Icy LHS-1 S1

The influence of the sublimating water is visible in the measured thermal conductivity data as well, which is shown in Figure 6.17. Initially, there is a slow rise in the thermal conductivity, which steepens after 200 K, and peaks at 237 K with $(0.016 \pm 0.002)\,\mathrm{W\,m^{-1}\,K^{-1}}$, after which it declines to values in the range of the dry simulant thermal conductivity at 260 K.

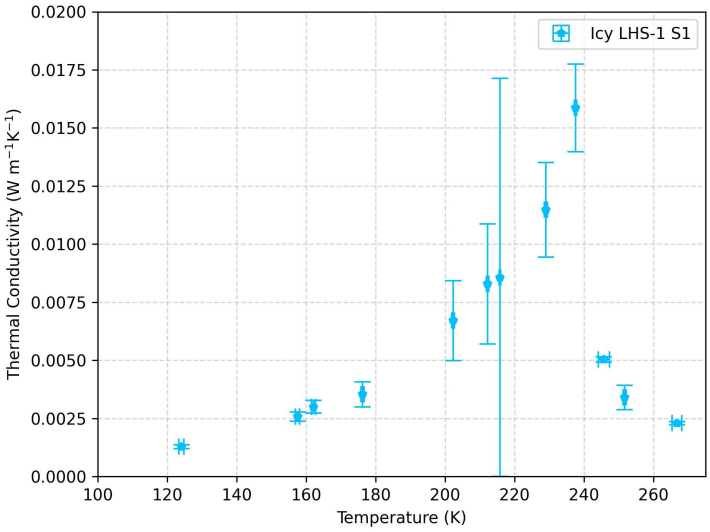

Figure 6.17.: Thermal conductivity of Icy LHS-1 S1. After an initial slow rise in thermal conductivity with temperature, a strong increase is visible after 200 K, which is related to the sublimation of water ice inside the sample. After 240 K, the thermal conductivity drops again to lower values.

It should be noted that the temperature curves for this icy sample could not be evaluated as easily as those of the dry simulants. Often, the identification of the linear part was not unambiguous, leading to a larger uncertainty for some of the measurements. While all measurement curves can be found in the supplementary material in Appendix A.2, a detailed elaboration of this problem can be found in Section 6.2.7.
Following this initial temperature trend, the same sample was then heated to 380 K and cooled to 160 K without opening the chamber in between to measure the thermal conductivity of the desiccated material. The data of this dried material was presented already in Section 6.1.2, resembling the data of Dry LHS-1 S1, however, with a slightly different trend due to the lower bulk density, as a result of the desiccation process. No difference in thermal conductivity to the completely desiccated sample could be identified after 260 K, indicating that the sample was mostly dry at this point.

Thermal Diffusivity of Icy LHS-1 S1

Very similar to the curve of the thermal conductivity, the thermal diffusivity of this icy sample starts at low temperatures with an initial slow increase, resulting in a pronounced peak and a following abrupt drop when the sample dries out. Figure 6.18 shows this behavior. As already described above for the dry samples, these values should only be used as an indication of the order of magnitude. For the same reason, the specific heat capacity is not calculated for this sample.

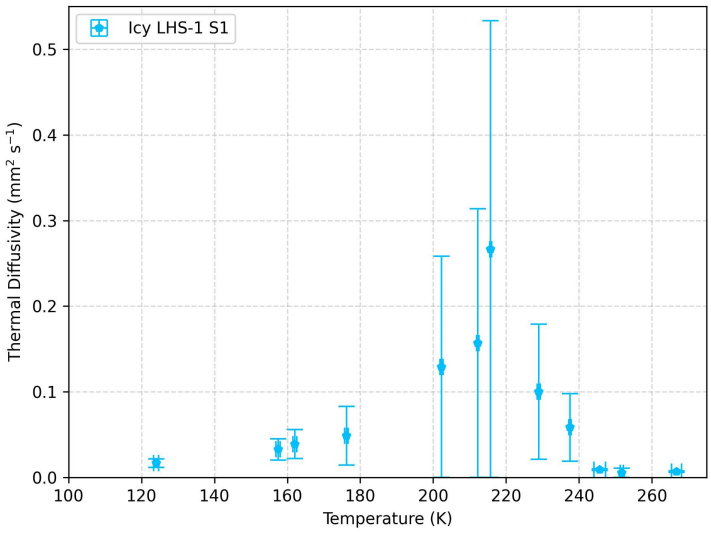

Figure 6.18.: Thermal diffusivity of Icy LHS-1 S1.

6.2.3. Micro-Granular Icy LHS-1 S2

The next sample was created having a slightly higher water content of (2.94 ± 0.11) wt % in comparison to the first sample. Figure 6.19 shows the temperature and pressure profiles of this sample during the constant temperature gradient sweep, which was inverted after the sample surpassed 200 K to cool it down again. After the cool-down phase, more measurements were done at slightly elevated temperatures of approximately 135 K and 155 K to analyze if changes still occur at these lower temperatures.
In contrast to the first sample, the TVAC pressure was below 10^{-4} mbar for most times, with the only exception being a small increase in pressure during the inversion of the temperature gradient, which could not be done smoothly at the time, leading to a short rise in temperature of approximately 2 K. This indicates that water vapor may have left the sample at even lower temperatures, but only in small amounts that were not measurable, possibly due to the large amount of noise. Additionally, the holes in the sample holder were frozen after the experiment, indicating that much water left the sample but was trapped at the sample holder, hindering more vapor from leaving the system efficiently. After the sample was removed from the TVAC, a residual ice content of (1.56 ± 0.10) wt % was measured to still be present in the sample, meaning that about half of the ice sublimated away during the experiment.
Due to a hardware issue, no pressure data could be collected after the 19th of April for this experiment run but due to these colder temperature regimes, no significant changes are anticipated.

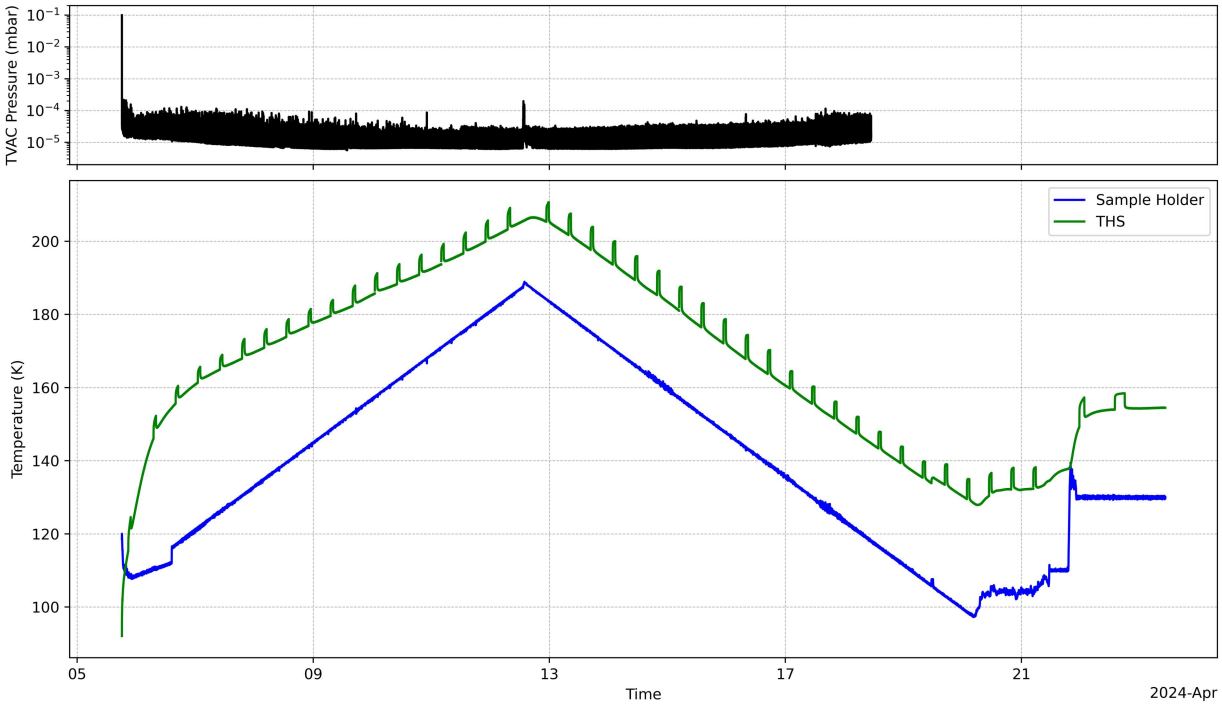

Figure 6.19.: Temperature and pressure profile of the Icy LHS-1 S2 measurements. During inversion of the constant temperature gradient, the sample holder temperature increased by 2 K, resulting in an increase in the TVAC pressure, indicative of water vapor leaving the system.

Thermal Conductivity of Icy LHS-1 S2

Figure 6.20 shows the thermal conductivity data for the heating as well as the cooling phase. The measured values closely resemble the initial slow increase in thermal conductivity previously found for sample Icy LHS-1 S1, whose thermal conductivity is also plotted on the left-hand side of the figure. After approximately 180 K, this initial increase flattens to be more or less constant at a plateau of $(0.0055 \pm 0.0001)\,\mathrm{W\,m^{-1}\,K^{-1}}$ for up to 210 K. During the subsequent cooling phase, the sample shows an irreversible behavior in thermal conductivity, with a pronounced decline within the initial 10 K and a gradual reduction with decreasing temperature afterwards, which is explained in Section 6.2.8. The last measurements done at the lower temperatures of approximately 135 K and 155 K are shown on the right-hand side of Figure 6.20 as well, closely matching the other data points by fading seamlessly into the overall trend of the data. This indicates that the conditions of the sample and those inside the sample holder did not change significantly at these lower temperatures.

Thermal Diffusivity of Icy LHS-1 S2

The same plot was made for the thermal diffusivity of the sample as depicted in Figure 6.21, showing a similar trend. The main difference is that the thermal diffusivity stays mostly constant during the cooling period, while the thermal conductivity slowly decreases with temperature.

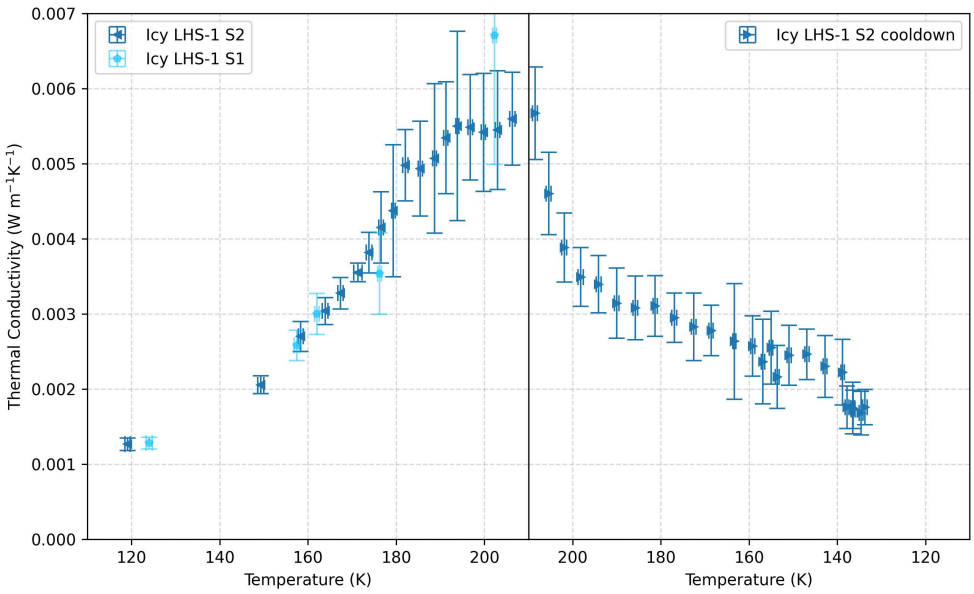

Figure 6.20.: Thermal conductivity of Icy LHS-1 S2 for the heating as well as the cooling period. For comparison, the results of Icy LHS-1 S1 are plotted on the right, closely matching the new data for lower temperatures. A clear difference between the heating and cooling data is evident, indicating that irreversible changes occurred during the temperature sweep.

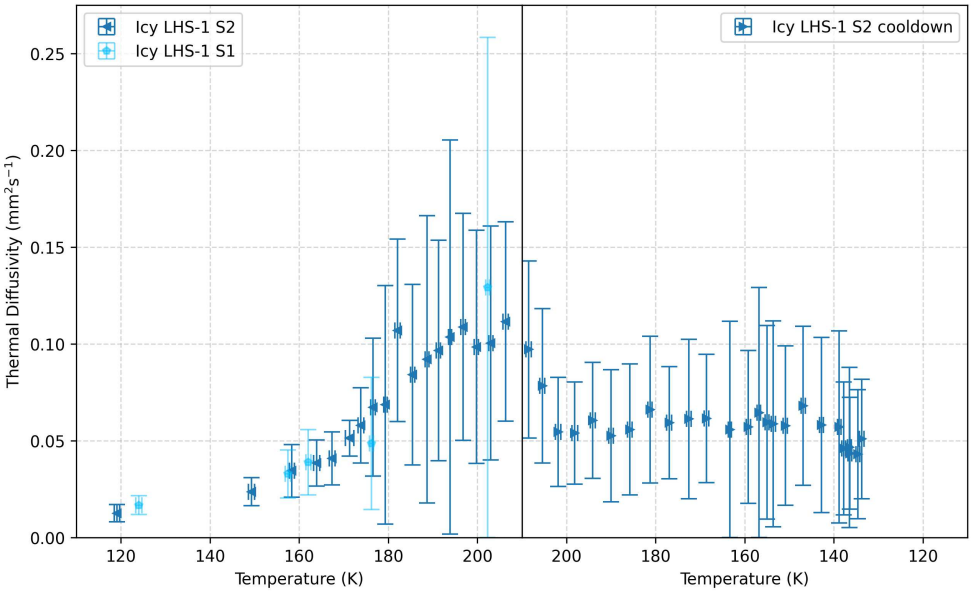

Figure 6.21.: Thermal diffusivity of Icy LHS-1 S2 for the heating as well as the cooling period.

6.2.4. Micro-Granular Icy LHS-1 S3

The final sample with micro-granular water ice particles was created with a larger ice content of $(7.71 \pm 0.08)\,\mathrm{wt\,\%}$. As visible in the temperature and pressure profile shown in Figure 6.22, this sample was heated with an initial temperature gradient of $0.5\,\mathrm{K\,h^{-1}}$ that was increased to $1\,\mathrm{K\,h^{-1}}$ after the sample reached 200 K. This was done to reduce the experimental time frame while drying out the sample.

Two unintentional interruptions in the liquid nitrogen supply resulted in one brief increase in the temperature of the sample holder on June 17th and one larger increase on June 23rd. The first one only had a minor influence on the sample's temperature, however, the second one led to a strong deviation as depicted in Figure 6.23. Within this temperature range, much water sublimated at once. Some of the measurements done in this period of strong temperature fluctuations had to be rendered unusable for evaluation because either no temperature correction was possible or no linear part could be identified, reducing the time resolution of the thermal conductivity measurements.

Additionally, the pressure reading in this experiment is not as time-resolved as in the first measurements due to a hardware issue. Nevertheless, a strong increase in pressure is visible after the sample holder surpassed 200 K, which persisted until the end of the experiment.

Following the removal of the sample from the TVAC, the remaining water content was measured to be $(2.51 \pm 0.01)\,\mathrm{wt\,\%}$.

Thermal Conductivity of Icy LHS-1 S3

The results of the thermal conductivity measurements are shown in Figure 6.24, while a comparison of the initial temperature trend with the previously analyzed samples is given in Figure 6.25 for visibility purposes. While the initial thermal conductivity of the larger ice content sample Icy

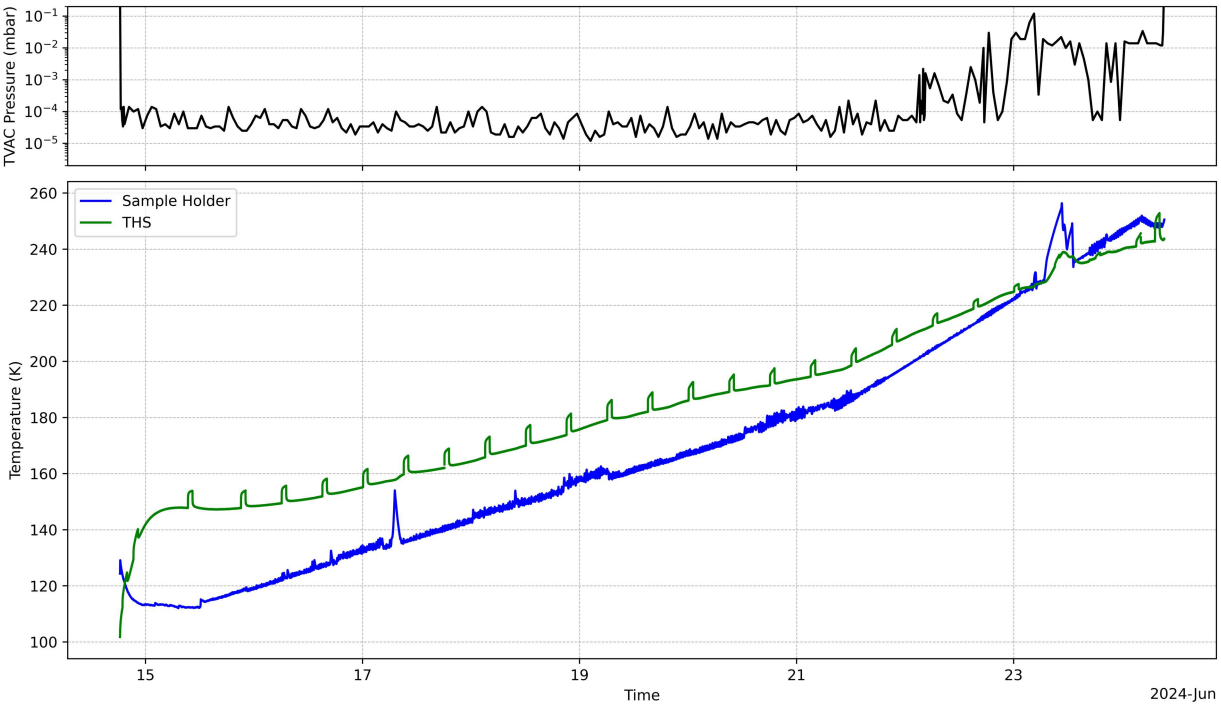

Figure 6.22.: Temperature and pressure profile of the Icy LHS-1 S3 measurements.

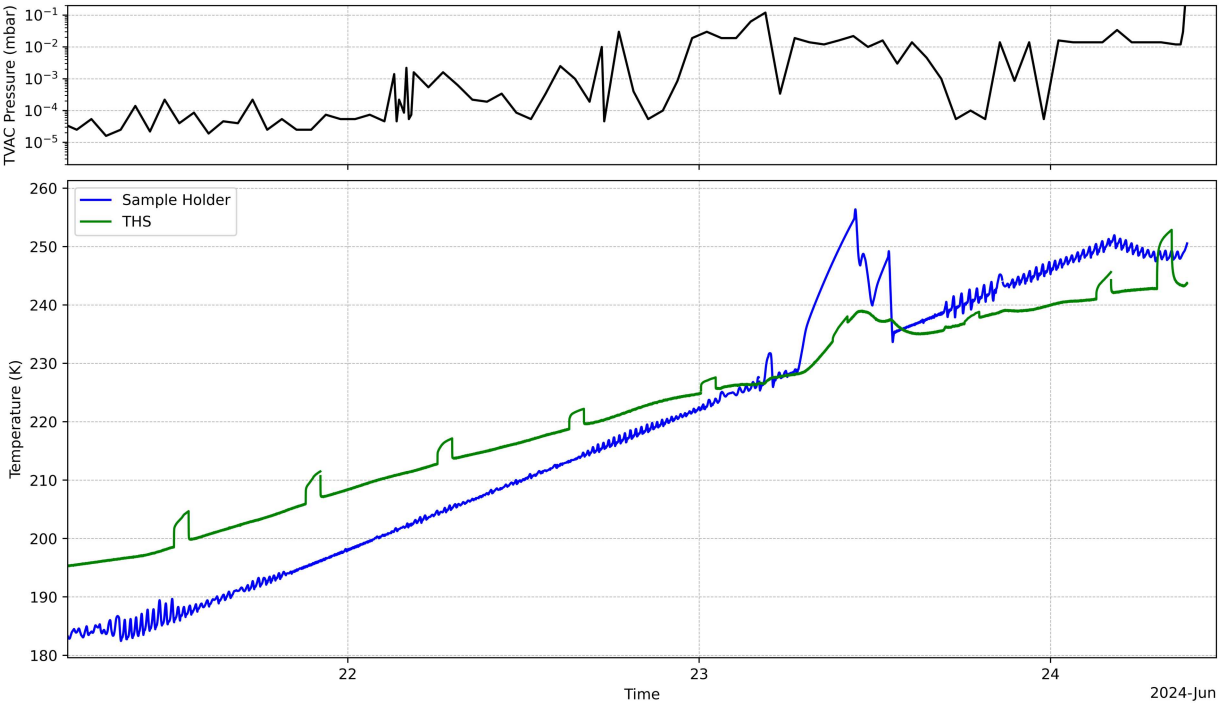

Figure 6.23.: Temperature and pressure profile closeup of the Icy LHS-1 S3 measurements. A first increase in pressure is visible after the sample holder reaches 200 K. The strong temperature fluctuations at the end of the experiment resulted in the exclusion of the affected measurements from the evaluation.

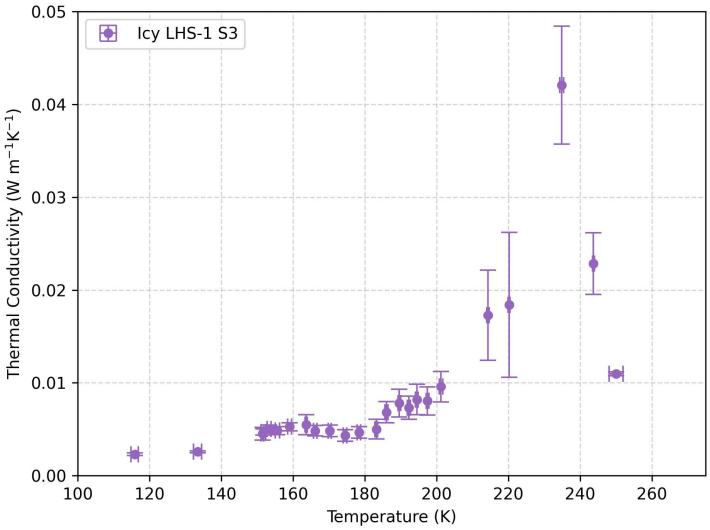

Figure 6.24.: Thermal conductivity of Icy LHS-1 S3. The trend of the data is very similar to Icy LHS-1 S1 with a slow initial increase, a larger peak at 336 K, and a final abrupt decrease in thermal conductivity.

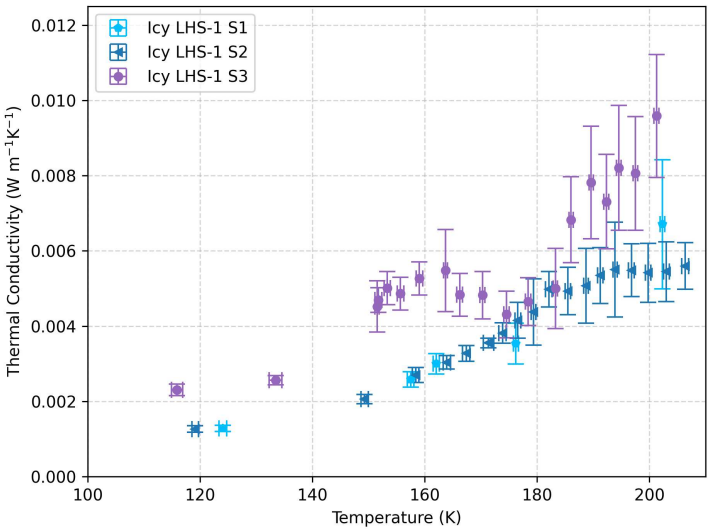

Figure 6.25.: Comparison of thermal conductivity data for Icy LHS-1 S1, S2 and S3 for low temperatures.

LHS-1 S3 is higher, the temperature trend is in general similar to that of Icy LHS-1 S1. A deviation is present for a temperature of 165 K, where a decline in the thermal conductivity is followed by a more pronounced increase beyond 185 K. However, the trend reaches its peak at the same temperature of 235 K, although with a significantly larger amplitude of $(0.042 \pm 0.006)\,\mathrm{W\,m^{-1}\,K^{-1}}$ in comparison to $(0.016 \pm 0.002)\,\mathrm{W\,m^{-1}\,K^{-1}}$ for Icy LHS-1 S1. Since this measurement is one of the two measurements conducted during the above-mentioned period of unintentional temperature increase, a large amount of sublimating water ice most certainly contributed to this peak. The other measurements were excluded due to the presence of numerous small-term temperature fluctuations.
Following 240 K, the last two measurements indicate an abrupt decrease in thermal conductivity, similar to the one found for Icy LHS-1 S1.

Thermal Diffusivity of Icy LHS-1 S3

The thermal diffusivity of Icy LHS-1 S3 shown in Figure 6.26 exhibits a similar initial slow increase, as well as a slight decrease at 165 K. The peak thermal diffusivity can be found for 215 K, while the thermal conductivity peaked at 235 K. At this temperature, the thermal diffusivity already dropped to values of $<0.1\,\mathrm{mm\,s^{-1}}$.
The error margins for many of the shown measurements are quite large, which results from the evaluation process and the uncertainty of the linear fit. As the allocation of the linear part was not always unambiguous for this sample, the scattering of the data points is significantly influenced by this effect.

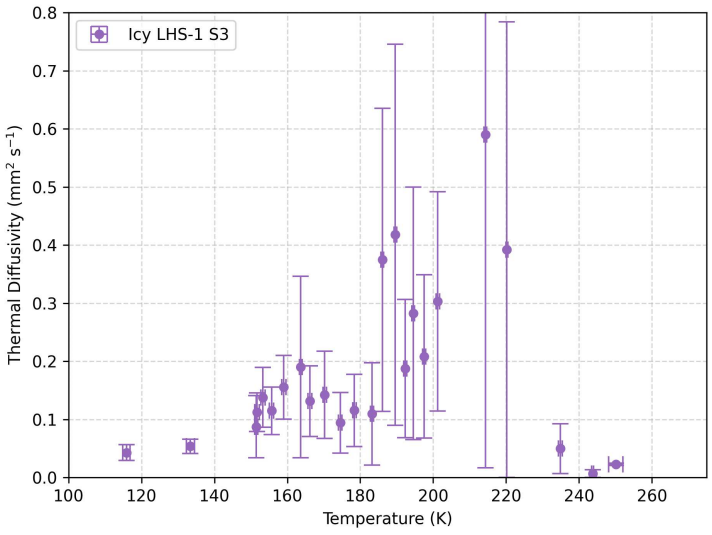

Figure 6.26.: Thermal diffusivity of Icy LHS-1 S3.

6.2.5. Mudpie LHS-1 S1

One last icy regolith sample was prepared in the form of a mudpie with a water ice content of $(2.9 \pm 0.1)\,\mathrm{wt\,\%}$, the same as sample Icy LHS-1 S2 and similar to S1. Figure 6.27 shows the temperature and pressure profile during the experiment, which included heating to 360 K and desiccating the sample. Similar to the previous samples, a constant temperature gradient of $0.5\,\mathrm{K\,h^{-1}}$ was used until reaching a sample temperature of 200 K, at which point the temperature gradient was increased to $1\,\mathrm{K\,h^{-1}}$.
At the same temperature, the pressure reading begins to indicate the escape of a considerable amount of water gas from the sample holder, which persists up to a sample holder temperature of approximately 270 K, where the TVAC pressure returns to nominal values. The fluctuations of the pressure data are also drastically reduced, as the outgassing reached a mostly stable state. The influence of the liquid nitrogen supply leakage is also reduced due to the reduced usage at larger temperatures.

Thermal Conductivity of Mudpie LHS-1 S1

The thermal conductivity data up to 260 K is shown in Figure 6.28 in comparison to the other icy samples with similar ice content. In contrast to the previously analyzed samples, the initial thermal conductivity is notably larger than any of the micro-granular samples and follows a slightly different temperature trend. After an initially constant thermal conductivity, there is an increase starting at 155 K, that reverses at 180 K with a minimum at 200 K. This is followed by a drastic increase and a final abrupt drop to values in the same range as those of the dry regolith

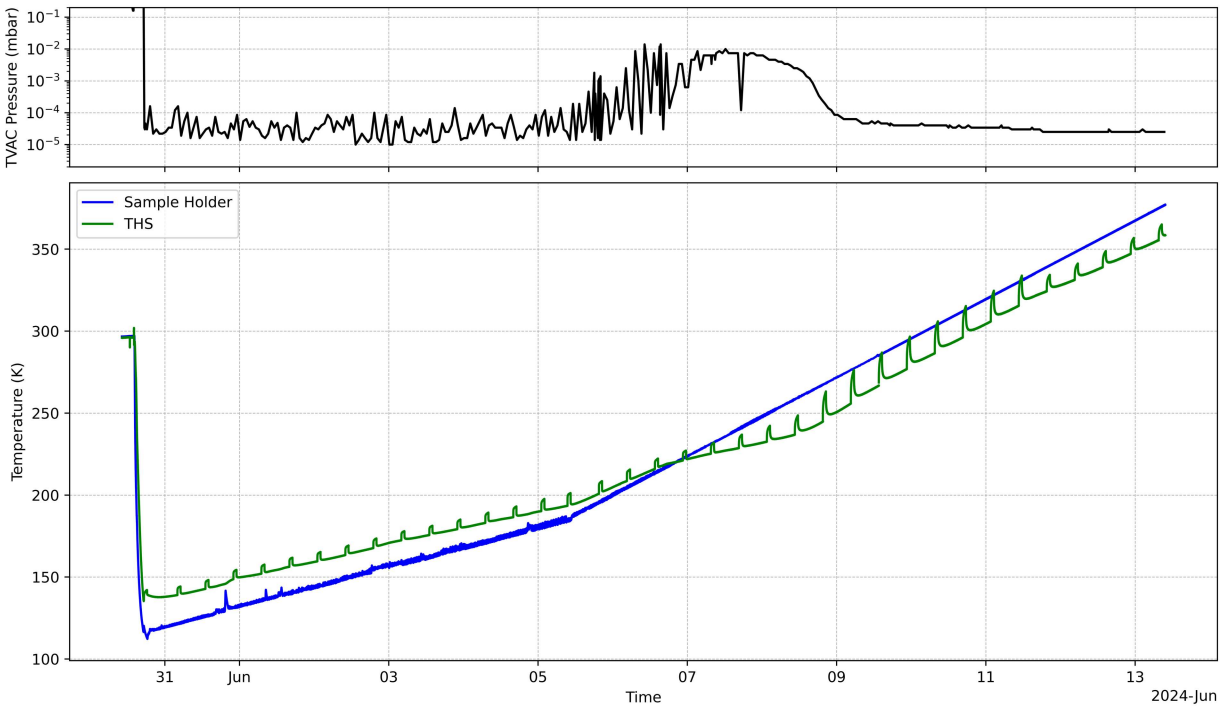

Figure 6.27.: Temperature and pressure profile of Mudpie LHS-1 S1.

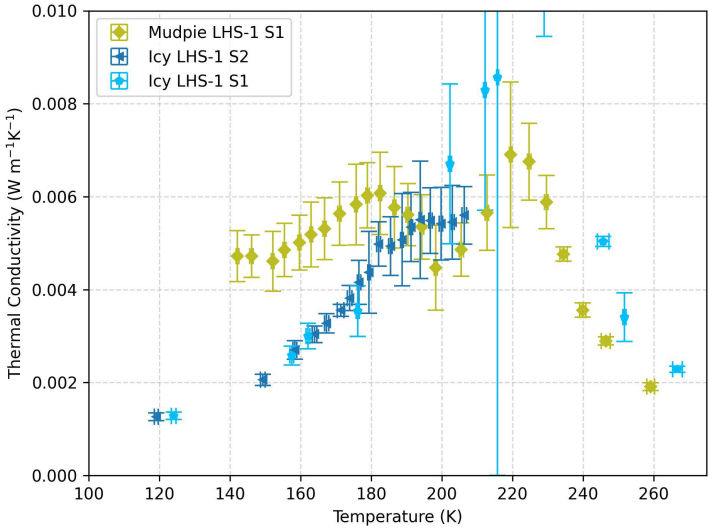

Figure 6.28.: Thermal conductivity of Mudpie LHS-1 S1 in comparison to those of the micro-granular samples Icy LHS-1 S1 and S2 with similar ice content.

after 260 K. This final peak is very similar to the behavior of Icy LHS-1 S1 and S3 at similar temperatures, although smaller in amplitude.

The evaluations for Mudpie LHS-1 S1 were subject to increased uncertainty, which was due to the same reason as for sample Icy LHS-1 S3, where the linear fit for the temperature curves could not be located with high certainty at all times.

Taking those larger errors into account, the initial thermal conductivity for temperatures of up to 215 K can also be fitted as a constant value with a standard uncertainty of $(5.16 \pm 0.16) \cdot 10^{-3}$ $\mathrm{W\,m^{-1}\,K^{-1}}$. This value is only slightly smaller than the thermal conductivity of the micro-granular sample Icy LHS-1 S2, which has the same ice content, at the plateau of (0.0055 ± 0.0001) $\mathrm{W\,m^{-1}\,K^{-1}}$ at temperatures above 190 K.

Especially at a temperature of 150 K, the thermal conductivity of the mudpie sample is larger by a factor of more than two. At temperatures exceeding 180 K, the thermal conductivities overlap with each other's uncertainty intervals.

At the time of the later drop in thermal conductivity beyond 230 K, the TVAC pressure is still quite large in the range of almost 10^{-2} mbar, only reaching nominal values as the sample reaches temperatures of >250 K. As no further water vapor can be supplied with even larger temperatures, the pressure drops. Notably, there is a temperature offset of approximately 10 K between the drop for Icy LHS-1 S1 and Mudpie LHS-1 S1. The mudpie sample dried out at lower temperatures, wich is correlated with the duration of the experiment. Icy LHS-1 S1 was heated step-wise at a relatively rapid rate, while Mudpie LHS-1 S1 was heated at a slower and constant rate over a longer period. This allowed the latter sample to lose more water mass between measurements, leading to complete desiccation at lower temperatures.

Similar to the dried version of Icy LHS-1 S1, the measured thermal conductivities for the dried Mudpie LHS-1 S1 exhibit a $a + b \cdot T^3$ behavior, that can be seen in Figure 6.29 fitted with $a = (1.03 \pm 0.08) \cdot 10^{-3}\,\mathrm{W\,m^{-1}\,K^{-1}}$ and $b = (4.09 \pm 0.27)\,\mathrm{W\,m^{-1}\,K^{-2}}$ with a coefficient of deter-

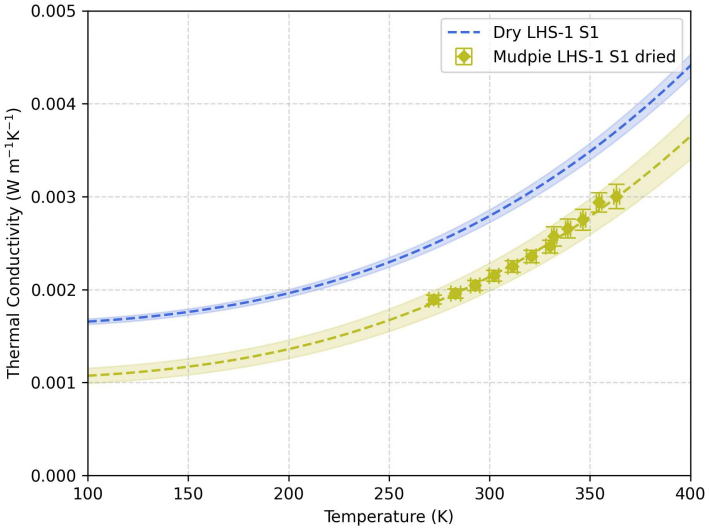

Figure 6.29.: Thermal conductivity of dried Mudpie LHS-1 S1. The plot shows the dried data fitted with a $a + b \cdot T^3$ with $R^2 = 0.99$ in comparison to the fit for Dry LHS-1 S1. Despite a lower volume filling fraction, the radiative conductivity is similar for both curves.

mination of $R^2 = 0.99$. In contrast to the previous dried icy sample, this curve does not cross the thermal conductivity curve of sample Dry LHS-1 S1 at higher temperatures, despite the lower volume filling fraction of 0.32 ± 0.03 in comparison to 0.49 ± 0.10 for Dry LHS-1 S1. This is probably the result of a different packing structure due to the added liquid water and grain agglomeration.

Thermal Diffusivity of Mudpie LHS-1 S1

Figure 6.30 shows the measured thermal diffusivity values of the mudpie sample in comparison to Icy LHS-1 S1 and S2. Starting with a slight increase in temperature, the thermal diffusivity of the mudpie drops after 220 K in a similar way to Icy LHS-1 S1. In comparison to the thermal conductivity, the initial temperature dependency differs only slightly from those found for Icy LHS-1 S1 and Icy LHS-1 S2. The initial thermal diffusivity is similarly larger at the lowest temperatures, while for temperatures up to 210 K, there is no difference in the thermal diffusivity within the given uncertainties. These uncertainties are again substantial due to the above-mentioned uncertainty in the linear fit determination. While sample Icy LHS-1 S1 shows a strong peak, the diffusivity of the mudpie sample remains constant until 200 K, after which a drop occurs, analogous to the thermal conductivity, as explained in Section 6.2.8.

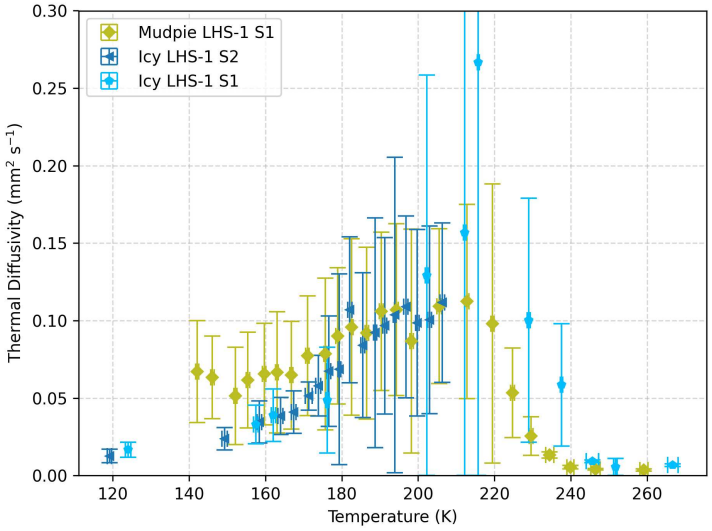

Figure 6.30.: Comparison of the thermal diffusivity of Mudpie LHS-1 S1 to micro-granular samples Icy LHS-1 S1 and S2 with a similar ice content of approximately 3 %. The peak value of Icy LHS-1 S1 lies outside of the shown range for visibility purposes.

6.2.6. Micro-Granular Water Ice S1

As a final sample presented here, micro-granular water ice particles were used without any added regolith simulant. The sample was heated with a constant temperature gradient of $0.5\,\mathrm{K\,h^{-1}}$ as shown in the temperature profile in Figure 6.31. While the sample reached temperatures of 170 K, the individual measurements showed a drastic increase in temperature at the end of each measurement that led to an even larger increase with larger sample temperatures, which is shown in the closeup in Figure 6.32. After this was detected, the temperature gradient was inverted and the THS voltage was reduced, which reduced the temperature increase of the THS during the next measurements. The sample was then cooled down again to approximately 150 K, where two additional measurements were done.

During the course of the experiment, another hardware issue with the pressure sensor occurred, resulting in a faulty readout on May 11th that persisted throughout the duration of the experiment. It is therefore not known if and at which point in time water gas left the sample holder. By measuring the weight of the sample after the experiments, a mass loss of 3.36 g was revealed, which corresponds to approximately 3.5 % of the initial sample mass.

Many of the measured temperature curves could not be fitted with high certainty for this sample, since the linear parts matching time bounds τ_{min} and τ_{max} of the model given in Section 5.2 often occurred during the first few seconds of the measurement. In these cases, a suitable fit could not be created, resulting in significant uncertainties and the discarding of multiple measurements. Furthermore, it is unclear whether the initially anticipated non-linear behavior of the THS already occurred during the preceding time interval for which data points are lacking. These problems are analyzed in Section 6.2.7, which goes into more detail on the applicability of the linear model for the icy samples with high thermal diffusivity.

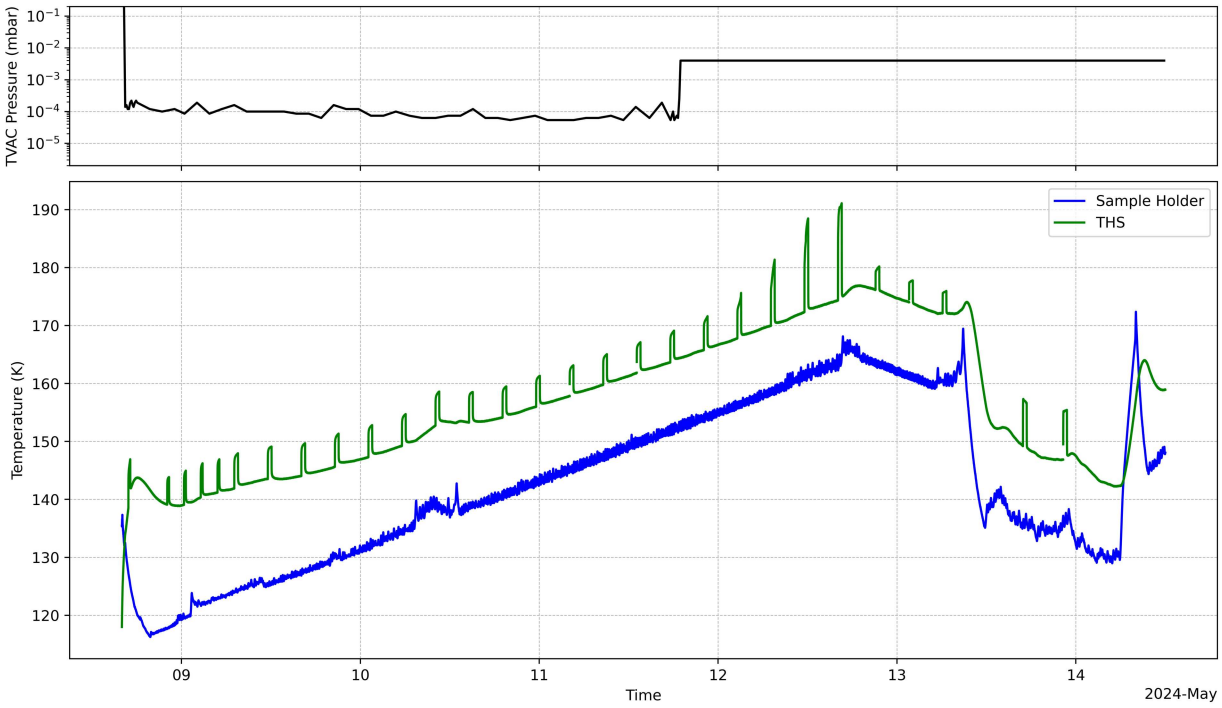

Figure 6.31.: Temperature and pressure profile of Micro-Granular Ice S1.

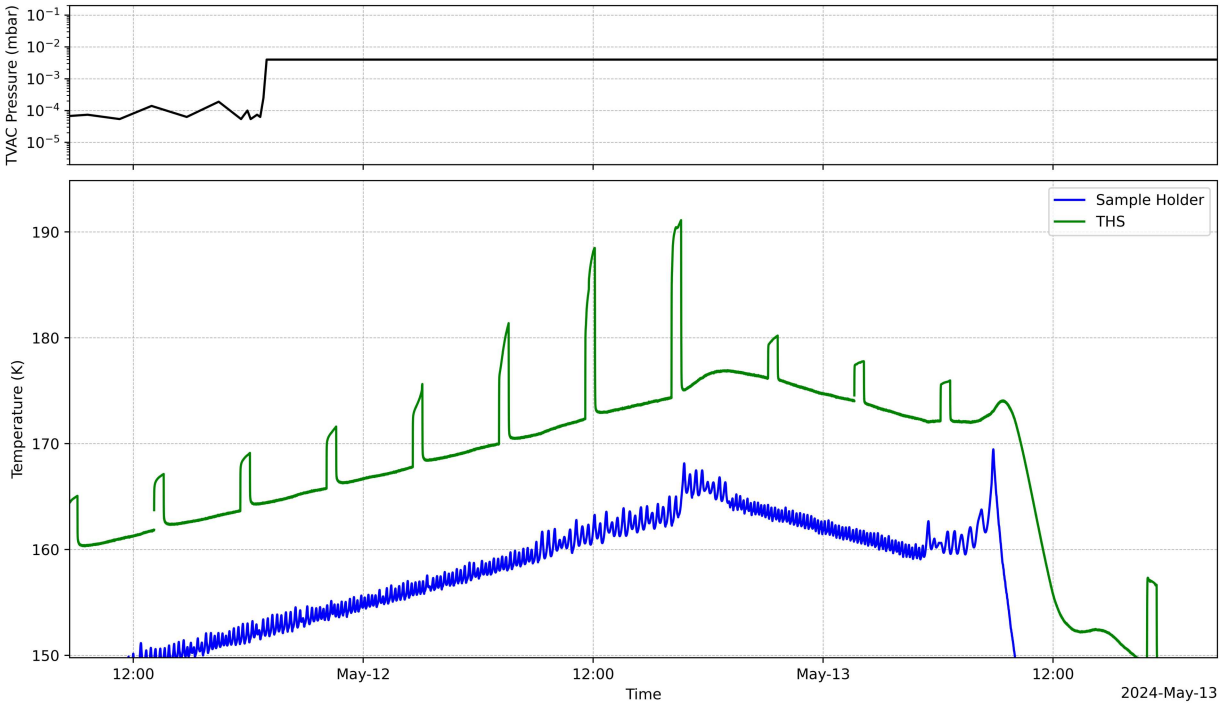

Figure 6.32.: Temperature and pressure profile closeup of Micro-Granular Ice S1.

Thermal Conductivity of Ice Particles S1

The thermal conductivity values derived from the evaluable measurements are presented in Figure 6.33. In comparison to the thermal conductivity of the icy regolith samples, which range up to $0.006\,\mathrm{W\,m^{-1}\,K^{-1}}$, the values for the pure ice sample are significantly higher, reaching up to $0.02\,\mathrm{W\,m^{-1}\,K^{-1}}$. It is important to note that these results are subject to large fluctuations, which are primarily attributed to the evaluation uncertainty. Therefore, these findings should be interpreted with caution. At the elevated temperatures, the slight drop in thermal conductivity is probably attributable to the loss of the particles closest to the THS due to sublimation, degrading the thermal contact.

Thermal Diffusivity of Ice Particles S1

The diffusivity values shown in Figure 6.34 exhibit considerably more fluctuations than those of the icy LHS-1 samples. As there is not clear temperature-dependent trend, it is probable that the pronounced fluctuations are not physical and can be attributed to the aforementioned uncertainty in the evaluation process.

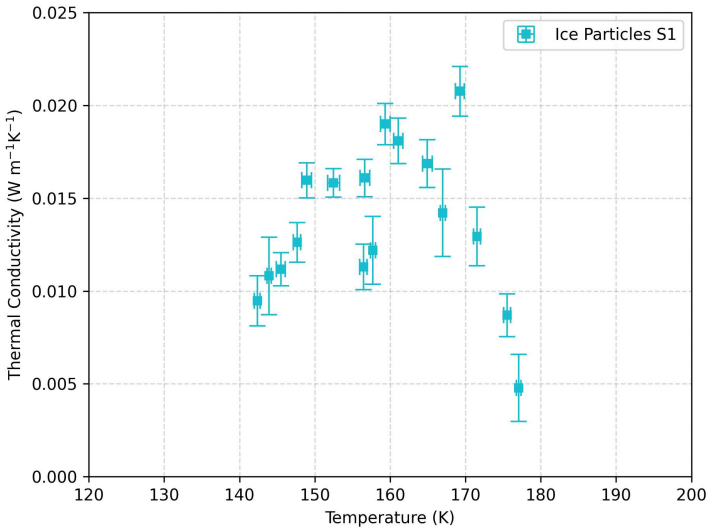

Figure 6.33.: Thermal conductivity of the micro-granular ice particles S1. These values are highly error-prone, since the determination of the linear part was not always certain.

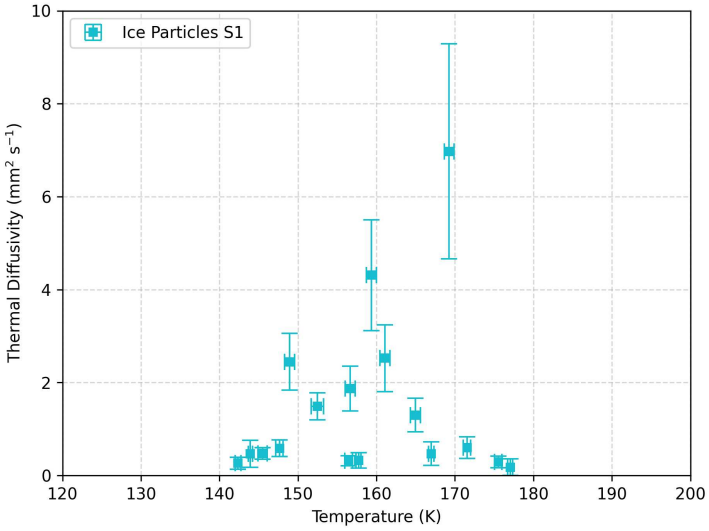

Figure 6.34.: Thermal diffusivity of the micro-granular ice particles S1. These values are highly error-prone, since the determination of the linear part was not always certain.

6.2.7. Applicability of the Linear Model to High Thermal Diffusivity Icy Samples

The determination of the linear part of a measurement curve, as explained in Section 5.2, is not always unambiguous. This phenomenon has been observed in the analysis of multiple icy samples in the previous sections. This section presents the reasons for such discrepancies from the ideal curves, as well as the criteria employed for the retention or rejection of such measurements.

In general, the heat transport from the THS into the surrounding sample has to be in a stable condition to result in a linear behavior during the measurement. Any alterations due to, for example, the finite heat capacity of the strip, any non-ideal contact with the sample, or the finite dimensions of the sample, result in a non-linear behavior as shown in Figure 6.35. Additional deviations occur if the sample changes, for example, due to the relocation of volatile materials.
With such processes, the temperature curve provides a direct insight into the heat flow in the sample. If the THS temperature increases drastically, a significant portion of the heat is not transported away efficiently and the effective thermal conductivity will be low. If the temperature only increases slightly, most of the heat is efficiently transported away, resulting in a large thermal conductivity.
In the case of ice, sublimation occurs if the temperature is high enough at a given pressure. The energy needed to change the phase of the water ice from solid to gaseous, the latent heat of sublimation, is taken from the energy emitted by the THS. Besides this alteration, the now present gas may transport heat via gas diffusion, adding another component to the effective thermal conductivity.
If the sample is still cold enough, the sublimated gas may redeposit during the diffusion process when it comes in contact with a colder part of the sample. The phase change back to a solid will release the same latent heat, converting it back into thermal energy, thus, effectively transporting

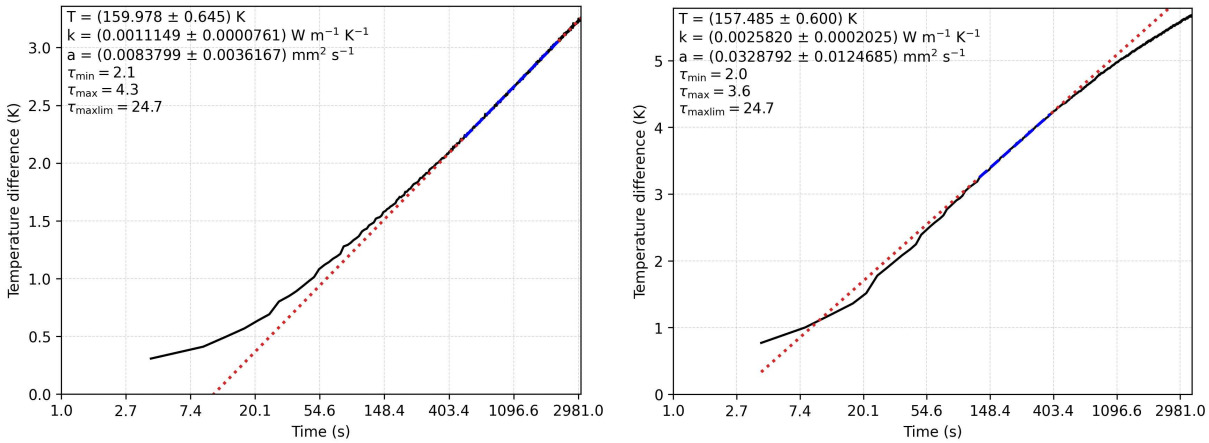

Figure 6.35.: Example measurement curves of dried Icy LHS-1 S1 (left) showing the initial non-linear behavior due to the finite heat capacity of the THS and bad thermal-contact to the sample, as well as Icy LHS-1 S1 (right) with a slight deviation from the linear curve at later times due to the relatively large thermal diffusivity and finite sample dimensions.

the energy from the THS to another point in the sample.
With this process occurring during a measurement, the temperature curve will flatten, since the heat of the THS can be transported away more efficiently. If the process is stable enough to lead to a linear part, the fit will result in a substantially larger effective thermal conductivity. If it only occurs during a measurement, a linear part might not be identifiable.

An additional effect that can alter the temperature curves is the depletion of any well-conducting material next to the THS, for example, due to sublimation. While the sample holder is colder than the inner sample, ice in direct contact with the warm THS will sublimate first. This means that for an icy sample, the few particles that do sublimate adjacent to the THS can significantly degrade the thermal contact with the surrounding sample by creating a small gap, increasing the slope of the measurement curve as heat can not be transported away as efficiently. Similar to the process above, this may result in non-linear curves if it occurs during a measurement. The process was evident with the pure ice sample, as the temperature drastically increased for some of the higher temperature measurements where sublimation was possible. One example for such an increase is provided by the explanatory curve shown in Figure 6.36.
In addition to these sublimation effects, the icy samples often display an elevated thermal diffusivity. For such samples, the energy emitted by the THS is transported away with remarkable efficiency, leading to a significant effect due to the outer sample surface. The loss of heat at these boundaries also leads to a non-linear behavior.
With larger thermal diffusivity, the rear non-linear part is more pronounced as shown in the exemplary curves in Figure 6.37, reducing the certainty with which the linear part can be identified. These curves also illustrate the relocation of the linear part due to the desiccation of the sample. For larger thermal diffusivities, the linear part occurs earlier during the measurement and has a shorter duration.
In the extreme case of the pure ice sample, the thermal diffusivity was so large, that the linear

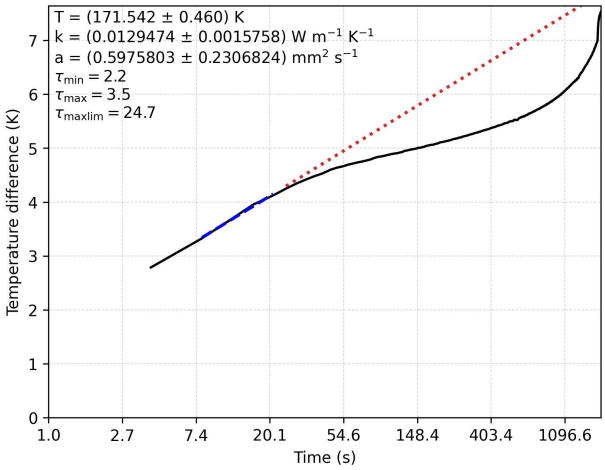

Figure 6.36.: Example measurement curve of the pure ice sample S1. The final strong increase in temperature is presumably attributable to the sublimation of contacting ice particles.

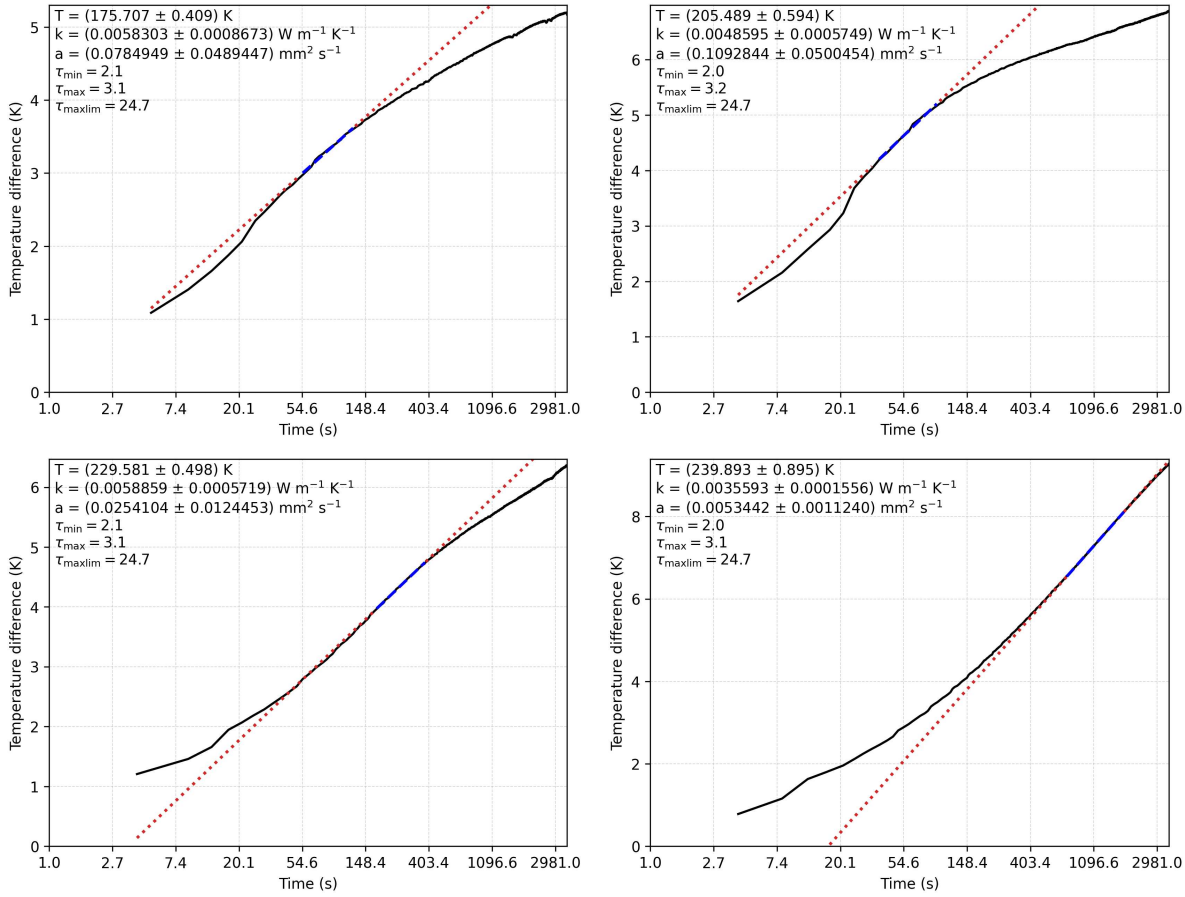

Figure 6.37.: Temperature curves of Mudpie LHS-1 S1 showing thermal diffusivity changes with temperature. Increasing temperature raises diffusivity (top), extending the non-linear region, which then decreases as diffusivity becomes negligible (bottom).

part started to appear within the first few seconds of a measurement, where the data was not yet time-resolved enough to provide enough information for a good fit. Therefore, it is not possible to determine with certainty whether the fitted intervals of this sample reflected the phase of stable heat transfer or lie within the non-linear parts. It would have been advantageous to use the full volume of the sample holder for this experiment, to reduce the influence of the sample's limited dimension.

In order to analyze the measurement curves that do not exhibit an extensive linear part, it is essential to define the time limits for the fitting process. Figure 6.38 shows the theoretical intervals for the linear fit, that arise from the time limits $\tau_{\min} = 2.0$ and $\tau_{\max} = 24.7$ utilizing Equation 5.2. The later one arises from the probing depth of approximately 3.5 cm which corresponds to half of the width of the aluminium tray used for the icy samples. An alternative version is given by the dotted line for $\tau_{\max} = 10.6$, which emerges if the probing depth is chosen to be 1.5 cm, the approximate depth with which the strip is buried beneath the surface. For a large thermal diffusivity, the linear part of a measurement should start within the first few seconds, as is the case for many of the pure ice measurements. However, comparing the endpoint of the linear fits, for example in Figure 6.36, the linear part should theoretically persist up to at least a few hundred seconds, which is not the case for the real measurements. The same shortening of the linear part in comparison to the theoretical limit is evident for many other measurement curves. This discrepancy is attributable to the imprecise nature of the thermal diffusivity measurement, given that the geometry of the THS is optimized for conductivity measurements.
Due to this reason, all high thermal diffusivity measurements where the linear part was not unambiguously identifiable were fitted on the first possible part of the curve. If the fit matched the

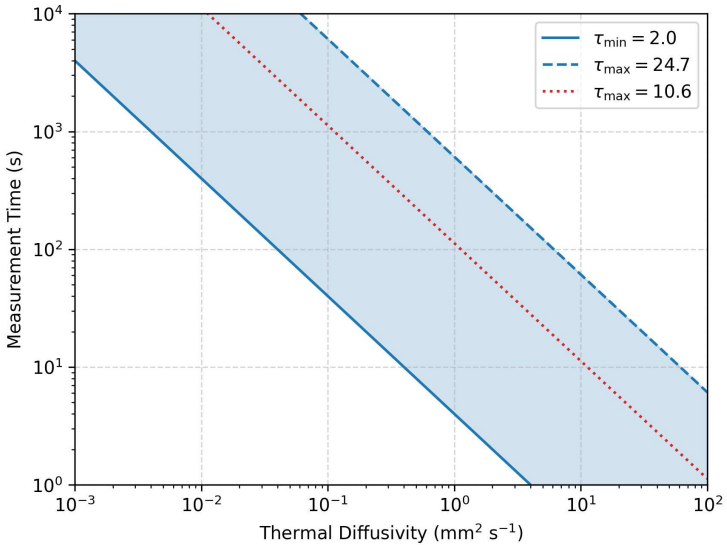

Figure 6.38.: Theoretical time limits of the linear fits vs. thermal diffusivity, determined by the non-dimensional time limits $\tau_{\min} = 2.0$ and $\tau_{\max}$. $\tau_{\max} = \sqrt{2}R_0/D$ changes with the probing depth R_0, exemplary plotted for 3.5 cm ($\tau_{\max} = 24.7$), the horizontal probing depth in the aluminium tray and 1.5 cm ($\tau_{\max} = 10.6$), the burial depth of the THS below the sample surface.

initial bound of $\tau_{\min} = 2$ and provided a low enough deviation from the original data, it was used for further evaluation. If the latter condition could not be met, the measurement was excluded from further analysis. Any deviations from the ideal linear fit are reflected in the uncertainty of the fit parameters, which in turn are reflected in the uncertainty of the conductivity values, as explained in Section 5.2.

A final effect that rendered a small number of measurements unusable was the occurrence of short-term temperature fluctuations. These fluctuations were able to influence the sample's inner temperature more often for high thermal diffusivity samples. If situated at the end of a measurement curve, the linear part in the beginning could still be evaluated. If the fluctuations occurred before or in between the measurements, it was not possible to correct the temperature gradient or identify a linear component, which resulted in the inability to evaluate those measurements.

In conclusion, the linear model remains applicable to a significant portion of the measurements conducted on the icy samples. The increase in thermal diffusivity with temperature often created large uncertainty in the identification of the linear part, resulting in either large uncertainties for the derived thermal transport properties or rendering the measurements non-evaluable.
For future measurements, larger sample sizes, an increased time resolution, and a different THS geometry or an entirely different method would be beneficial to analyze the behavior of high thermal diffusivity samples more precisely.

6.2.8. Analysis of the Thermal Conductivity of the Icy Samples

Considering all of the evaluable measurements presented in the previous sections, it was found that the thermal conductivities of the icy samples are in general larger compared to those of the dry regolith simulants. Starting at lower temperatures, Figure 6.39 shows the thermal conductivity of Icy LHS-1 S1 and S2 in comparison to the $a + b \cdot T^3$ fit of the dried variant of Icy LHS-1 S1. The data for the fit is extrapolated from 160 K to lower temperatures.
Since the pressure of the TVAC is typically in the range of 10^{-5} mbar to 10^{-4} mbar, the first ice starts to sublimate at around 170 K to 185 K as visible in Figure 2.5. The initial increase in thermal conductivity with low temperatures is thereby not related to any gas conductivity, as major sublimation occurs only with rising temperatures. However, even for elevated temperatures, as already discussed in Section 2.2.2 and shown by Figure 2.7, the thermal conductivity that results from gas diffusion is negligible up to 220 K for small pore sizes in the order of 10^{-4} m to 10^{-6} m, as they are expected to occur in the regolith simulants. This is also shown in Figure 6.40, where the theoretical contribution of water gas at the sublimation pressure is plotted for this range of possible pore space sizes in comparison to the measured values.
This diffusive thermal conductivity of water gas can not explain the initial rise or the drastic increase in thermal conductivity of the icy samples. It has to be noted that the molecular flow ends near 250 K, depending on the pore space size. Following a transitional period, a constant kinetic gas conductivity of approximately $10^{-1}\,\mathrm{W\,m^{-1}\,K^{-1}}$ would be anticipated for water gas. However, this is not the case as the samples underwent desiccation and the actual pressure within the sample holder is probably considerably smaller than the sublimation pressure at this point.
Additionally, contributions from the solid ice particles have been neglected for now, but even when

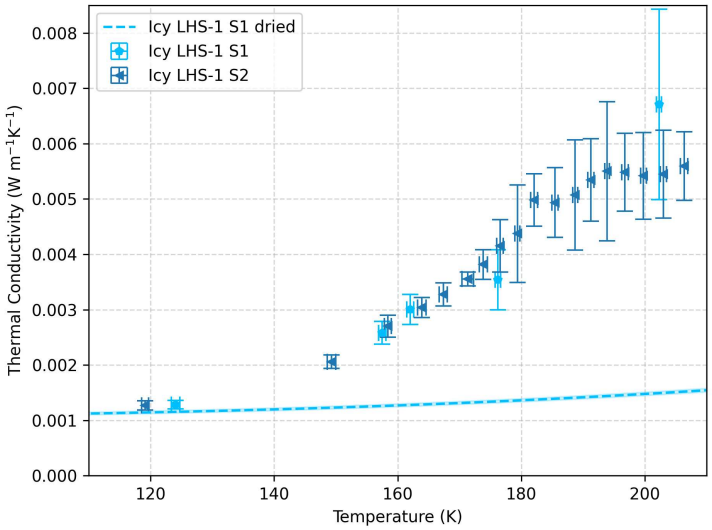

Figure 6.39.: Comparison of the thermal conductivities of icy and dry regolith simulant samples.

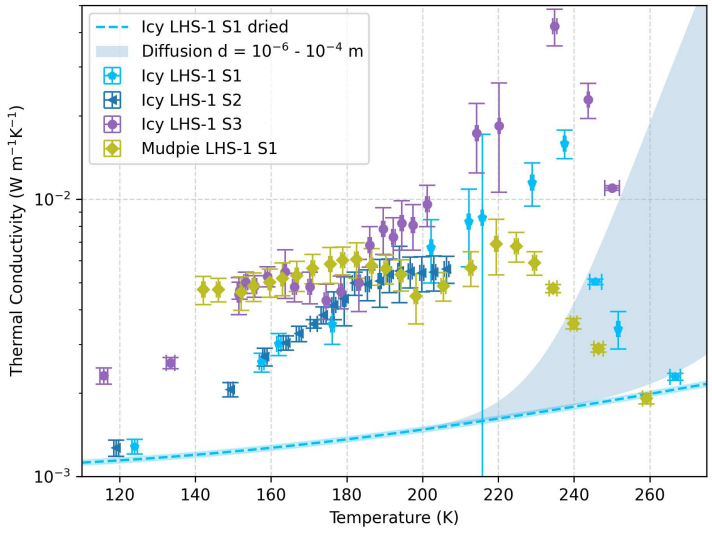

Figure 6.40.: Thermal conductivity due to gas diffusion in comparison to the measurements done on the icy regolith samples. The diffusive heat transfer model is unable to account for either the initial or the subsequent, more pronounced increase in temperature.

assuming a constant conductivity in the range of $0.008\,\mathrm{W\,m^{-1}\,K^{-1}}$, the additional gas conductivity could not explain the observed behavior.
Given that the diffusive heat transfer is not capable of explaining this behavior, it is important to consider the role of latent heat. The following calculation illustrates this. For a sample made of spherical ice particle with a radius of $2.4\,\mu\mathrm{m}$ and a density of $1\,\mathrm{g\,cm^{-3}}$, one particle would have a mass of approximately $5.8 \cdot 10^{-11}\,\mathrm{g}$. For hexagonal ice Ih, the latent heat of sublimation is $2834\,\mathrm{J\,g^{-1}}$ [13, p. 6-12], resulting in an energy of $1.6 \cdot 10^{-7}\,\mathrm{J}$ that is needed to sublimate a singular ice particle. The average power during a THS measurement is about $10^{-3}\,\mathrm{W}$ to $10^{-2}\,\mathrm{W}$, which means that theoretically, the equivalent of 6000 to 60000 particles, a mass of approximately $10^{-6}\,\mathrm{g}$, could sublimate away each second if all power would go into this process only. This implies that sublimation due to the heat emitted from the THS plays no major role in the mass loss of a sample during an experiment but could theoretically consume as much heat as is emitted during the entire measurement. This would drastically alter the effective thermal conductivity. Due to the restricted size of the pore space, gas particles carrying the latent heat will collide with regolith particles at some point, limiting the thermal conductivity to some degree.

Figure 6.41 shows the thermal conductivity due to the latent heat transport model as described in Section 2.2.2 for the range of possible pore-space sizes S (blue shaded area). The radiative and conductive components are used from the $a + b \cdot T^3$ fit of the dried Icy LHS-1 S1, for now neglecting any alterations from the solid ice present in the sample.
While the precise dimensions of the pore-space of the samples are unknown, the depicted range is believed to be a reasonable approximation, given that the mean particle size of the regolith is slightly smaller than $10^{-4}\,\mathrm{m}$. Due to smaller particles filling parts of the space between the larger ones, the real pore-space size is smaller than the mean particle size. However, the angular nature

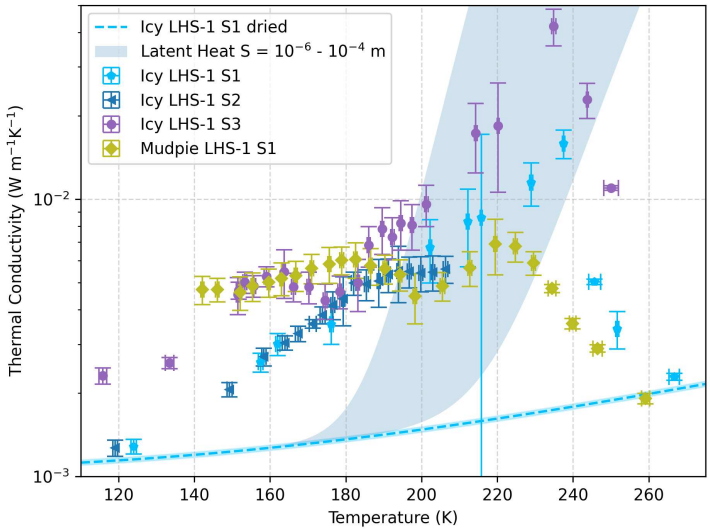

Figure 6.41.: Thermal conductivity due to latent heat transport. Depending on the pore-space size S, the latent heat transport model is able to explain the drastic increase in thermal conductivity for the icy samples at elevated temperatures above 200 K. The pressure was assumed to be the sublimation pressure at any given temperature.

of the particles may lead to an increased pore-space size.
Although the initial increase in thermal conductivity at the lower temperatures cannot be explained by this model, the increase after 200 K and the peak for most samples at 220 K is well-fitted, indicating that latent heat transport plays a major role in the effective thermal conductivity of icy samples at temperatures where sublimation occurs.
One notable deviation can be seen for the mudpie sample and Icy LHS-1 S2, where the increase at 200 K is not as pronounced and not even present. This could be connected to the difference in the ice structure of the mudpie, where fused ice might block the escape routes of gas particles, limiting the sublimation rate and thereby limiting the latent heat transport in the vicinity of the THS. For Icy LHS-1 S2, the obstruction of the sample holder's openings as well as in colder parts in the sample created from re-deposited ice could have led to a mostly constant pressure in the sample volume. Since this sample was not heated sufficiently, the outer parts of the sample's pore space as well as the sample holder openings never cleared out completely. This maintained the pressure close to the sublimation pressure, thereby limiting the amount of water that sublimates and, consequently, minimizing the latent heat transport.

For the samples that were heated completely, the latent heat transport is limited by the amount of ice in the sample as well as the outgassing rate. If no more ice molecules sublimate, and the residual gas is removed by the pumps, the effective thermal conductivity declines over time to values comparable to those of the dried regolith. This is evident for Icy LHS-1 S1, Mudpie LHS-1 S1, and to a lesser extent, Icy LHS-1 S3. In terms of thermal conductivity, all samples were desiccated completely at a temperature of approximately 260 K.

Finally, the initial temperature increase of the icy samples has to be analyzed. Due to the significant difference between the mudpie sample and the micro-granular samples at the lowest temperatures, this deviation probably results from the contact of the ice particles with the regolith grains. In contrast to the granular samples, where contact occurs at discrete locations between the spherical ice particles and the angular regolith particles, there are initially numerous fused connections between ice and regolith particles for the mudpie. This results in a more efficient conductive heat transfer, even when ice contents are relatively low. At the same time, the thermal conductivity of Icy LHS-1 S3 is initially larger, since more connections are present due to the larger amount of ice in the sample. This leads to a larger contribution of the ice's solid conductivity in comparison to the other samples.
As temperatures increase, the contact points between the ice and regolith particles transform due to the formation of ice necks between the particles, which is referred to as sintering. For this to occur, it is necessary that small amounts of material sublimate and redeposit directly at the contact point, thereby increasing the thermal conductivity of the granular samples to levels comparable to that of the initially well-connected mudpie sample at higher temperatures. This theory may be supported by the observations made for sample Icy LHS-1 S2, where the results of the cooling curve differed from the heating curve, indicating a restructuring of the material's contact points. Since the ice content of the mudpie sample was quite low, there is no complete fused structure but possibly a multitude of local fused agglomerates that sinter with increasing temperature, resulting in a small increase in thermal conductivity.

Furthermore, an observation was made regarding the macroscopic structure of Icy LHS-1 S2 and sample Icy LHS-1 S3, which were not desiccated completely. Upon removal of the samples from the TVAC, some parts of the sample were observed to be bound into larger ice-regolith chunks, as shown in Figure 6.42. For Icy LHS-1 S3, which was heated to 250 K, these chunks occurred across the entire length of the aluminium tray, while the upper surface was mostly desiccated. This effect can be attributed to the warmer temperature of the sample holder lid. In the case of Icy LHS-1 S2, which was exposed to peak temperatures of only 210 K, chunks, although smaller in number and size, could be found as well. A singular larger one was found in the lower corner of the tray, where the temperatures were possibly the lowest. Although all of these chunks could be broken into smaller fragments with only a small amount of force, they are clear evidence of a cementation process, altering the thermal conductivity of these samples.

For lunar regolith samples that might consist of significantly more granular ice than the above presented samples, an upper limit can be provided by the measurements done on the pure micro-granular water ice sample. Figure 6.43 shows the measured thermal conductivity values in comparison to a fit with the Gundlach Blum model. For this fit, the median particle radius of the ice particles of 2.4 µm and the measured volume filling fraction of 0.32 were utilized as fixed parameters, while the scaling parameter χ was a free parameter. The empirical solid thermal conductivity of ice $\lambda_{\text{solid}} = {}^{567}/_{T}$ was used from Klinger [38], while the Young's modulus $E = 10.5 \cdot 10^9$ Pa and Poisson ratio $\mu = 0.31$ were extracted from Gundlach et al. [39]. The specific surface energy of micro-granular ice particles $\gamma = 0.19\,\mathrm{J\,m^{-2}}$ was determined by Gundlach et al. [40], although for smaller particles with a mean size of approximately 1.5 µm.
At the given particle size, the solid conductivity's ${}^{1}/_{T}$ dependence is predominant for low temper-

Figure 6.42.: Cemented chunks in Icy LHS-1 2 (left) and Icy LHS-1 3 (right) that were removed from the TVAC before complete desiccation. The visible ice-regolith chunks did not exhibit much mechanical strength and could be easily broken with a pointy metal tool but are clear evidence of a cementation process.

atures, as can be seen from the best fit with $\chi = 0.38$.
In addition to small variations in the particle shapes and sizes from perfectly mono-disperse spherical-shaped particles and the influences of agglomeration, the small χ value is probably caused by deviations in the material properties, especially the specific surface energy, which might differ for the here used values. If employing the specific surface energy as a free parameter with a fixed $\chi = 1$, a best fit can be found for $\gamma = 0.01\,\mathrm{J\,m^{-2}}$, which could also be reasonable.

With regard to high ice content icy regolith samples, microgranular water ice will thereby lead to maximal thermal conductivities of approximately $0.02\,\mathrm{W\,m^{-1}\,K^{-1}}$ for temperatures above 100 K. Due to the $1/T$ behavior, thermal conductivity increases with decreasing temperature for samples with extremely large ice contents in the low-temperature regime. This is in contrast to the low-ice content samples, where there is a decrease in thermal conductivity for a reduction in temperature, resulting in values approaching those of the dry simulant. It has to be noted that the solid conductivity used here is only applicable to temperatures above 30 K. For lower temperatures, the thermal conductivity should approach zero similarly to that of the regolith, as phononic heat transfer freezes out.
In future measurements, it would be advantageous to analyze the relative amount of ice in a regolith simulant sample required to lead to a change between these anticipated temperature trends.

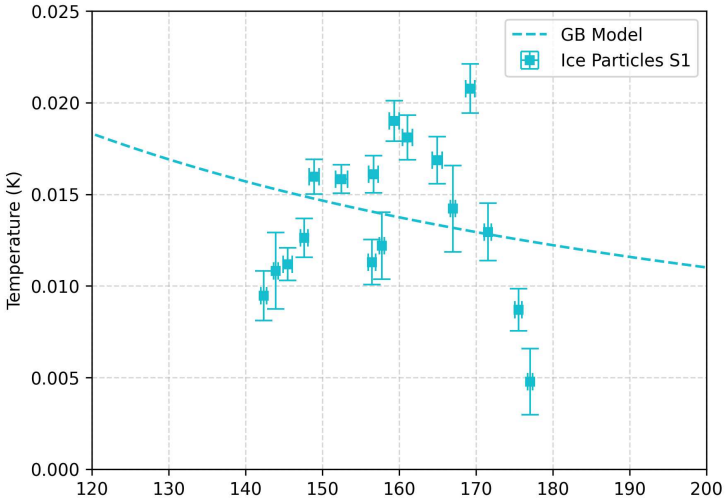

Figure 6.43.: Gundlach Blum model fitted to the measured thermal conductivity values of the micro-granular ice particles S1. Although the measurements were subject to increased uncertainty, the fit resembles the order of magnitude in thermal conductivity that can be achieved with pure micro-granular ice.

7. Discussion

The objective of this study, to analyze the temperature behavior of the thermal conductivity of icy lunar regolith simulant samples, has been achieved. While the specific results of the measurements have already been discussed in Chapter 6, this chapter briefly discusses the main uncertainties and difficulties encountered in this study.

For the dry regolith simulants, the main uncertainty of the measurements lies in the determination of the bulk density, which could not be done with high precision. This is a clear disadvantage of the utilized setup and the intrusive THS method, which alters the packing structure of any granular material into which it is inserted. Nevertheless, the impact of compaction on thermal conductivity was successfully demonstrated.
The comparison to Apollo samples and the difference between the LHS-1 and Lunex simulant partly showed major differences in the thermal conductivity, which could not be fully explained in this study. Further investigations on the influence of the chemical composition and particle size distribution, and possibly a comparison to a more detailed physical model are required to investigate the exact influence of polydisperse and irregular particles on the thermal conductivity.

In comparison to the dry samples, the icy regolith simulants exhibited drastically different thermal conductivities which could be explained qualitatively by the effect of sintering and the contribution of latent heat to thermal conductivity. While these explanations seem reasonable, they have not been quantitatively verified. This would require a detailed physical model of the mixture of granular water ice and regolith, combined with additional measurements of the influence of, for example, ice content and sublimation rate at higher resolution. It is additionally important to analyze the Knudsen regime in more detail, as the strong increase in thermal conductivity could potentially be connected to a transitional region from molecular flow to collision-based gas diffusion. Such an analysis requires detailed knowledge about the pore-space shape and size of the icy samples, as well as a model of the drying process that starts at similar temperatures.
The partly large uncertainties in the measured thermal conductivity allow for some freedom of interpretation. For example, for the mudpie simulant, a constant conductivity would be plausible, however, a slight temperature-dependent increase similar to the micro-granular samples is also a possibility. This is because the exact nature of the fused connections in this simulant is unknown. Larger fused icy regolith agglomerates are present instead of a homogeneously fused structure, which may result in a different temperature behavior than that a completely fused sample may exhibit.

The unknown microscopic nature of the samples presents a significant challenge, because the production process was verified only based on macroscopic visual appearance. It is important to consider the potential for the presence of small, invisible ice agglomerates, as well as larger regolith chunks, which may have been overlooked. Therefore, a microscopic analysis should be conducted in the future to investigate the homogeneity of the samples and to identify deviations

due to such agglomerates. This analysis could also be utilized to improve the production process and find better methods of mixing the ice particles with the regolith simulant. Additionally, a way of producing a homogeneous sample with a precisely predefinable water ice content could not be achieved in this work. However, such a method would be beneficial for future applications and large-scale production.

One of the main uncertainties regarding the thermal conductivity of the icy samples was the intrinsic uncertainty of the thermal diffusivity measured by the THS, as this diffusivity is required to evaluate the linear part of the measurement curves. This uncertainty could not be quantified apart from the slope and intercept error of the linear fits. However, the error is small for low thermal diffusivity samples, which means that significant variations should occur only for larger ice content samples, and the temperature regions where sublimation occurs and thermal diffusivity is high.

In conclusion, despite these uncertainties, the measured temperature behavior of the icy samples could be analyzed and explained. However, future measurements are needed to provide more insight into the detailed parameters that influence these trends.

8. Summary and Outlook

To analyze the thermal transport properties of icy regolith, a novel unfused micro-granular icy regolith simulant was created by utilizing micrometer-sized water ice particles, intermixed with lunar highlands simulant LHS-1.

Thermal conductivity measurements were done with a transient hot strip in a thermal vacuum chamber with pressures of $<10^{-4}$ mbar and a temperature range of 120 K to 450 K. The thermal conductivity of the dry regolith simulants in this temperature range can be adequately described by Watson's equation $a + b \cdot T^3$ and with the Gundlach Blum Bürger model of thermal conductivity, suggesting that the found values are in good agreement with the theory of heat transport in granular media.
The icy samples exhibited significant deviations from these results. Three micro-granular icy regolith samples and a fused mudpie simulant were analyzed with low ice contents in the range of 2 wt % to 8 wt %. The microgranular simulants initially exhibited a low conductivity, comparable to that of the dry simulant, with variations depending on the ice content. The thermal conductivity increased with temperature, which is attributable to the sintering of the ice grains and regolith particles. The mudpie sample demonstrated an initially significantly larger thermal conductivity of up to a temperature of 200 K, as most of the ice was fused already. The sublimation occurring at higher temperatures led to a drastic increase in thermal conductivity, which can be attributed to the transport of latent heat. With further increasing temperatures, the samples desiccated and were completely dry exceeding 260 K.

In conclusion, the results of this study indicate that lunar icy regolith will exhibit thermal conductivities similar to dry regolith for low temperatures if only small amounts of micrometer-sized ice are scattered discretely in the regolith. If fused deposits are present, which is the case for both initially fused samples and those that have undergone temperature-driven cementation, a greater thermal conductivity is to be expected, even for low ice contents.
In general, most permanently shadowed regions exhibit temperatures much lower than those investigated here. Due to the vanishing thermal conductivity for $T \to 0$, the PSRs are well insulated from temperature changes. For this reason, the results of this study are more applicable for boundary regions near those craters or in the lunar subsurface, where temperatures could get large enough for sublimation to occur, for example during diurnal temperature changes. In such cases, cemented icy-regolith structures would be present in those regions. Therefore, temperature-driven cementation effects are important to consider for any thermophysical models that aim to describe these regions.

One major finding of this study is the significant contribution of latent heat to the thermal conductivity of icy samples at temperatures where sublimation occurs. This effect is not only important to consider for thermophysical models of icy boundary regions, but also for water extraction experiments, where the exploitation of this increased conductivity could drastically improve the

efficiency. From a technical standpoint, a setup should be capable of precisely controlling the pressure and temperature, thereby enabling the continuous utilization of this effect.

Future experiments should focus on the analysis of the low-temperature behavior of the icy regolith simulants, which would require a more efficient cooling system. The current setup could be improved by actively cooling all components of the sample holder and by reducing its dimensions. With these implementations, it would be possible to analyze a deviation from the $a + b \cdot T^3$ behavior for the dry samples, expected to occur below 100 K, and to determine the relation of ice content to thermal conductivity with more precision. Here, it would also be interesting to investigate the ice content, at which a deviation from dry regolith is evident.
However, a reduced sample size would prohibit the measurement of high thermal diffusivity samples, limiting the maximal possible ice content.
Finally, it would be interesting to analyze the impact of the applied THS method by comparing it to a steady-state method. With such a method, the main disadvantage of the THS, which is the intrusive nature, would be avoided and the bulk density could be controlled with more precision. Additionally, the large uncertainties due to the imprecise determination of the thermal diffusivity could be avoided and the findings presented here could be verified.

List of Figures

List of Tables

List of Abbreviations

GBB	Gundlach Blum Bürger.
GUI	Graphical User Interface.
LCROSS	Lunar Crater Observation and Sensing Satellite.
LMS	Lunar Mineralogical Spectrometer.
LUPEX	Lunar Polar Exploration Mission.
M3	Moon Mineralogy Mapper.
PID	Proportional-Integral-Derivative.
PSR	Permanently Shadowed Region.
SEM	Scanning Electron Microscope.
SOFIA	Stratospheric Observatory for Infrared Astronomy.
THS	Transient Hot Strip.
TVAC	Thermal Vacuum Chamber.
VIPER	Volatiles Investigating Polar Exploration Rover.

References

[1] Heiken, G. H., Vaniman, D. T., and French, B. M. (1991). *Lunar Sourcebook. A User's Guide to the Moon*. Cambridge University Press. ISBN: 0-521–33444-6.

[2] Hare, T. M. et al. (2015). *Image mosaic and topographic map of the moon. Scientific Investigations Map*. Tech. rep. U.S. Geological Survey. DOI: http://dx.doi.org/10.3133/sim3316.

[3] Li, S. et al. (2018). "Direct evidence of surface exposed water ice in the lunar polar regions". In: *Proceedings of the National Academy of Sciences* 115.36, pp. 8907–8912. DOI: 10.1073/pnas.1802345115.

[4] Colaprete, A. et al. (2010). "Detection of Water in the LCROSS Ejecta Plume". In: *Science* 330.6003, pp. 463–468. DOI: 10.1126/science.1186986.

[5] Lin, H. et al. (2022). "In situ detection of water on the Moon by the Chang'E-5 lander". In: *Science Advances* 8.1, eabl9174. DOI: 10.1126/sciadv.abl9174.

[6] Honniball, C. I. et al. (2021). "Molecular water detected on the sunlit Moon by SOFIA". In: *Nature Astronomy* 5, pp. 121–127. DOI: 10.1038/s41550-020-01222-x.

[7] Hayne, P. O., Aharonson, O., and Schörghofer, N. (2021). "Micro cold traps on the Moon". In: *Nature Astronomy* 5.2, pp. 169–175. DOI: 10.1038/s41550-020-1198-9.

[8] Chakraborty, T. et al. (2024). "On the reachability and genesis of water ice on the Moon". In: *ISPRS Journal of Photogrammetry and Remote Sensing* 211, pp. 392–405. DOI: https://doi.org/10.1016/j.isprsjprs.2024.03.020.

[9] Gundlach, B. and Blum, J. (2012). "Outgassing of icy bodies in the Solar System – II: Heat transport in dry, porous surface dust layers". In: *Icarus* 219.2, pp. 618–629. DOI: https://doi.org/10.1016/j.icarus.2012.03.013.

[10] Gundlach, B. and Blum, J. (2013). "A new method to determine the grain size of planetary regolith". In: *Icarus* 223.1, pp. 479–492. DOI: https://doi.org/10.1016/j.icarus.2012.11.039.

[11] Bürger, J. et al. (2024). "A Microphysical Thermal Model for the Lunar Regolith: Investigating the Latitudinal Dependence of Regolith Properties". In: *Journal of Geophysical Research: Planets* 129.3, e2023JE008152. DOI: https://doi.org/10.1029/2023JE008152.

[12] Marx, A. and Gross, R. (2018). *Festkörperphysik*. 3rd ed. De Gruyter. ISBN: 978-3-11-055822-7.

[13] Haynes, W. (2017). *CRC Handbook of Chemistry and Physics*. 97th ed. CRC Press. ISBN: 978-1-4987-5429-3.

[14] Huebner, W. et al. (2006). *Heat and Gas Diffusion in Comet Nuclei*. ISSI scientific report SR-004. International Space Science Institute.

[15] Persson, B. N. J. (2023). "Heat transfer in granular media consisting of particles in humid air at low confining pressure". In: *The European Physical Journal B* 96.2, p. 14. DOI: 10.1140/epjb/s10051-023-00483-5.

[16] VDI e. V., ed. (2013). *VDI-Wärmeatlas*. 11th ed. Springer Vieweg Berlin, Heidelberg. ISBN: 978-3-642-19982-0.

[17] Steiner, G. and Kömle, N. I. (1991). "A model of the thermal conductivity of porous water ice at low gas pressures". In: *Planetary and Space Science* 39.3, pp. 507–513. DOI: https://doi.org/10.1016/0032-0633(91)90009-Y.

[18] Hayne, P. O. et al. (2017). "Global Regolith Thermophysical Properties of the Moon From the Diviner Lunar Radiometer Experiment". In: *Journal of Geophysical Research: Planets* 122.12, pp. 2371–2400. DOI: https://doi.org/10.1002/2017JE005387.

[19] Ricardo, D. et al. (2023). "A review on the preparation techniques and geotechnical behaviour of icy lunar regolith simulants". In: *Advances in Space Research* 72.10, pp. 4553–4581. DOI: https://doi.org/10.1016/j.asr.2023.09.032.

[20] Reiss, P. et al. (2021). "Dynamics of Subsurface Migration of Water on the Moon". In: *Journal of Geophysical Research: Planets* 126.5, e2020JE006742. DOI: https://doi.org/10.1029/2020JE006742.

[21] Šļumba, K., Sargeant, H. M., and Britt, D. T. (2024). "Development of icy regolith simulant for lunar permanently shadowed regions". In: *Advances in Space Research* 73.6, pp. 3222–3234. DOI: https://doi.org/10.1016/j.asr.2024.01.014.

[22] Johnson, D. K. et al. (2024). "Pressure Sintered icy lunar regolith Simulant (PSS): A novel icy regolith simulant production method". In: *Icarus* 410, p. 115885. DOI: https://doi.org/10.1016/j.icarus.2023.115885.

[23] Exolith Lab (2022). *LHS-1 Lunar Highlands Simulant Fact Sheet*. 002-01-001-0621.

[24] Lunex Technologies (2024). *Lunar Regolith Simulant 57% Terrae - 25% Mare Datasheet*.

[25] Kreuzig, C. et al. (2023). "Micrometre-sized ice particles for planetary science experiments – CoPhyLab cryogenic granular sample production and storage". In: *RAS Techniques and Instruments* 2.1, pp. 686–694. DOI: 10.1093/rasti/rzad049.

[26] NASA (2021). *NASA-STD-1008. Classifications and Requirements for Testing Systems and Hardware to be Exposed to Dust in Planetary Environments*. Tech. rep.

[27] Ensinger AG (2023). *TECAPEEK natural - Stock Shapes (rods, plates, tubes) Data Sheet*.

[28] Gustafsson, S. E., Karawacki, E., and Khan, M. N. (1979). "Transient hot-strip method for simultaneously measuring thermal conductivity and thermal diffusivity of solids and fluids". In: *Journal of Physics D: Applied Physics* 12.9, p. 1411. DOI: 10.1088/0022-3727/12/9/003.

[29] Hammerschmidt, U. and Sabuga, W. (2000). "Transient Hot Strip (THS) Method: Uncertainty Assessment". In: *International Journal of Thermophysics* 21.1, pp. 217–248. DOI: 10.1023/A:1006621324390.

[30] Cremers, C. J. (1971). "Density, Pressure, and Temperature Effects on Heat Transfer in Apollo 11 Fines". In: *AIAA Journal* 9.11, pp. 2180–2183. DOI: 10.2514/3.50023.

[31] Cremers, C. J. (1972). "Thermal conductivity of Apollo 12 fines at intermediate density". In: *The Moon* 4, pp. 88–92. DOI: https://doi.org/10.1007/BF00562916.

[32] Cremers, C. J. (1975). "Thermophysical properties of Apollo 14 fines". In: *Journal of Geophysical Research* 80.32, pp. 4466–4470. DOI: https://doi.org/10.1029/JB080i032p04466.

[33] Cremers, C. J. and Hsia, H. S. (1973). "Thermal Conductivity and diffusivity of Apollo 15 fines at low density". In: *Proceedings of the Fourth Lunar Science Conference*. Vol. 3, pp. 2459–2464.

[34] Cremers, C. J. and Hsia, H. S. (1974). "Thermal Conductivity of Apollo 16 lunar fines". In: *Proceedings of the Fith Lunar Science Conference*. Vol. 3, pp. 2703–2708.

[35] Fountain, J. A. and West, E. A. (1970). "Thermal conductivity of particulate basalt as a function of density in simulated lunar and Martian environments". In: *Journal of Geophysical Research* 75.20, pp. 4063–4069. DOI: https://doi.org/10.1029/JB075i020p04063.

[36] Austen, D. H. and Shafirovich, E. (2024). "Thermophysical properties of lunar regolith simulant LHS-1 and ice sublimation kinetics in its mixtures with frozen water". In: *Thermochimica Acta* 731, p. 179648. DOI: https://doi.org/10.1016/j.tca.2023.179648.

[37] Tabuchi, Y., Kioka, A., and Yamada, Y. (2023). "Water permeability of sunlit lunar highlands regolith using LHS-1 simulant". In: *Acta Astronautica* 213, pp. 344–354. DOI: https://doi.org/10.1016/j.actaastro.2023.09.027.

[38] Klinger, J. (1981). "Some consequences of a phase transition of water ice on the heat balance of comet nuclei". In: *Icarus* 47.3, pp. 320–324. DOI: https://doi.org/10.1016/0019-1035(81)90179-2.

[39] Gundlach, B. et al. (2018). "Sintering and sublimation of micrometre-sized water-ice particles: the formation of surface crusts on icy Solar System bodies". In: *Monthly Notices of the Royal Astronomical Society* 479.4, pp. 5272–5287. DOI: 10.1093/mnras/sty1839.

[40] Gundlach, B. et al. (2011). "Micrometer-sized ice particles for planetary-science experiments – I. Preparation, critical rolling friction force, and specific surface energy". In: *Icarus* 214.2, pp. 717–723. DOI: https://doi.org/10.1016/j.icarus.2011.05.005.

A. Appendix

A.1. Lunar Regolith Simulant Properties

Table A.1.: Mineralogy of LHS-1 [23].

Component	Wt. %
Anorthosite	74.4
Glass-rich basalt	24.7
Ilmenite	0.4
Pyroxene	0.3
Olivine	0.2

Table A.2.: Mineralogy of the Lunex simulant [24].

Component	Wt. %
Plagioclase feldspar (Bytownite)	72.75
Plagioclase feldspar (Labradorite)	9.6
Pyroxene (Augite)	10.48
Olivine (Forsterite)	4.6
Titanomagnetite	0.25
Alkali feldspar	0.08

Table A.3.: Chemical compositions of LHS-1 [23], Lunex [24] and basalt [35].

Substance	LHS-1 (Wt. %)	Lunex (Wt. %)	Basalt (Wt. %)
SiO_2	51.2	48.7	51
Al_2O_3	26.6	26.1	14
CaO	12.8	13.0	8.0
FeO	2.7	3.3	8.8
Na_2O	2.9	3.2	3.4
MgO	2.6	4.4	-
TiO_2	0.6	0.7	2.7
K_2O	0.5	0.6	1.7
MnO	0.1	0.25	-
P_2O_5	0.1	0.1	1.4
FeO_2	-	-	3.4
H_2O	-	-	0.86
CO_2	-	-	0.03
S	-	-	0.004
Residual	0.9	1.6	0.036

A.2. Supplementary Material

The code and additional images used in this thesis are available online at the following directory: `https://github.com/Wa-He/MasterThesis`. This supplementary material includes the correction and evaluation plots of all measurements conducted, as well as the complete code implemented for the control software and data analysis.